UNIVERSITY OF CALIFORNIA
RIVERSIDE

Experimental Studies of Oxide Magnetic Tunnel Junctions and Graphene

A Dissertation submitted in partial satisfaction
of the requirements for the degree of

Doctor of Philosophy

in

Physics

by

Xinfei Liu

September 2012

Dissertation Committee:
Professor Jing Shi, Chairperson
Professor Ward P. Beyermann
Professor Harry W. K. Tom

The Dissertation of Xinfei Liu is approved:

Committee Chairperson

University of California, Riverside

Acknowledgement

Here comes the end of my Ph.D journey at UC Riverside and beginning of my new career. Six-year journey at UC Riverside is a long and arduous period in my life. With all the pains and gains, I finally grew up with solid foundation for my future. At this moment of accomplishment, all I want to say is to thank everyone and everything at Riverside in the past years that make this thesis possible.

First of all I want to acknowledge my advisor, Prof. Jing Shi. I am very much thankful to him for taking me as his student at the critical stage of my Ph.D. Dr. Shi is a great scientist and a gracious mentor who demonstrates professional, perceptive and insightful qualities as an advisor. This work would not have been possible without his guidance, support and encouragement. Under his guidance I successfully overcame many difficulties and learned a lot. With all I get equipped here, I am ready to accept all the challenges in the future.

I am very grateful to my committee members, Prof. Harry Tom and Prof. Ward Beyermann for their lively discussions and constructive feedback. Thank you to the entire Physics Department at UC Riverside. All of the faculty and staff that I worked with and met throughout my graduate studies are wonderful people and a real pleasure to know.

My colleagues in the lab ensured I was constantly engaged along the way. In particular, I cannot thank enough to Di Wu, Jianxing Ma, Zuhong Xiong, Tao Lin, Deqi Wang, Peng Wei, Yong Pu, Ray Sachs, Zhiyong Wang, Zilong Jiang and Mohamed Hamad for their help and friendship. Without them, all my life in the past years would be

much tougher.

Also, I would like to deeply thank my friends at UC Riverside: Wenzhong Bao, Dong Gui, Wei Han, Zilong Jiang, Tao Lin, Yingdi Liu, Keyu Pi, Yong Pu, Dezheng Sun, Deqi Wang, Zhiyong Wang, Peng Wei, Dong Yan, Dexter Humphrey. All of you gave me a lot of help both in my personal life and academic research. Thank you so much for your support. I enjoyed every moment staying with all of you.

Last but not least I would like to thank my wife Lin for her personal support and great patience at all times. Despite the hardest time, she always stayed with me and gave me her solid encouragement. My parents and brother have given me their unequivocal support throughout, as always, for which my mere expression of thanks likewise does not suffice. If I wrote down everything I ever wanted for my family member, I would not have believed I could meet someone better! All of your continued support and urging after moving to Riverside is deeply appreciated. To all of you, thanks for always being there for me.

Thank you all!

ABSTRACT OF THE DISSERTATION

Experimental Studies of Oxide Magnetic Tunnel Junctions
and Graphene

by

Xinfei Liu

Doctor of Philosophy, Graduate Program in Physics
University of California, Riverside, September 2012
Dr. Jing Shi, Chairperson

The spin state of a ferromagnet on its surface can deviate significantly from that in the bulk. This effect could be strongly orientation-dependent in manganites due to strong spin-orbit interaction. We have successfully fabricated high-quality (110)-oriented $[La_{0.7}Sr_{0.3}MnO_3$ (t) /$SrTiO_3$ (3ML)$]_n$ superlattices and systematically studied their crystal structure as well as interface magnetism. Compared to the (100)-oriented counterparts, LSMO has a thinner dead-layer and a higher interface moment at the (110)-oriented LSMO/STO interface. The magnetism of the manganite interface could be manipulated by taking advantage of the orientation-dependent nature of the exchange interactions.

To engineer the interface between tunnel barrier and LSMO, we have developed a high quality Al_2O_3 (HfO_2) tunnel barrier in LSMO/Al_2O_3/Co stacking structure with Al_2O_3 (HfO_2) grown *ex-situ* by Atomic Layer Deposition as well as LSMO/STO/Co with LSMO and STO epitaxially grown by Pulsed Laser Deposition in both (100) and (110) orientations. Our specially designed shadow mask technique ensures a high yield and high performance of magnetic tunnel junction devices. The magneto-transport

measurements show very interesting results.

The thermoelectric properties of graphene have been extensively studied both experimentally and theoretically. The exotic band structure of graphene leads to unusual thermoelectric properties which are sensitive to the carrier mobility. However, all the previous experiments were based on graphene samples with fixed mobility and make comparisons between different samples. Recently, we showed that it is possible to tune the carrier mobility of the same graphene device over a wide range. We adopted this method and systematically studied the magneto- Seebeck and Nernst effects for different mobility values. The crossover behavior of the Seebeck signal reported before around Charge Neutral Point is related to the splitting of zeroth Landau Level. Moreover, we demonstrate that the Nernst peak linearly depends on the carrier mobility in graphene.

Besides, we find that the empirical relation between the longitudinal and Hall resistivities and its counterpart between the Seebeck and Nernst coefficients hold surprisingly well for graphene in the quantum transport regime except near the Dirac point. The validity of the relations is cross-examined by independently varying the magnetic field and the carrier density in graphene. Our experimental results validate both derivative relations for massless Dirac Fermions except near the Dirac point.

.

Table of Contents

List of Figures

List of Tables

Chapter I

Manganite Electronic Band Structure and Magnetism

I-1 Manganite Crystal Structure

Transition metal oxides have been extensively studied in the past decades due to their rich crystallographic, electronic and magnetic properties [Chatterji *et al.*, 2004; Tokura *et al.*, 2000; Coey *et al.*, 1999]. Among the various transition metal oxides, $RaMnO_3$ manganite is one particular study object due to its strong electron-electron interaction, electron-lattice coupling and rich magnetic properties under proper doping. Here Ra represents rare earth elements such as La and Mn is Manganese atom. Historically the Double Exchange (DE) concept proposed by Zener in 1951 was used to explain the ferromagnetism of manganites with the perovskite $RaMnO_3$ structure [Zener, 1951]. $RaMnO_3$ manganite has a perovskite lattice structure and $RaMnO_3$ with trivalent Mn ion is a Mott insulator. Figure I-1 shows the crystal structure of its unit cell.

Eight Ra (yellow) atoms are sitting at the corner of the cubic lattice with one Mn (green) ion right in the cubic center. There are 6 oxygen atoms (red) located right in the center of the six faces of this cubic which form an octahedral together with the Mn ion. From this unit cell, we can find $RaMnO_3$ manganite has a layered structure feature along the cubical axis with a stacking sequence of RaO and MnO_2. In this case, all Mn ions are in trivalent state and the electronic configuration of Mn^{3+} ion is $[Ar]3d^4$. The crystal field leads to a splitting of Mn^{3+} d electron orbitals into 2 high energy e_g orbitals and 3 low

energy t_{2g} orbitals.

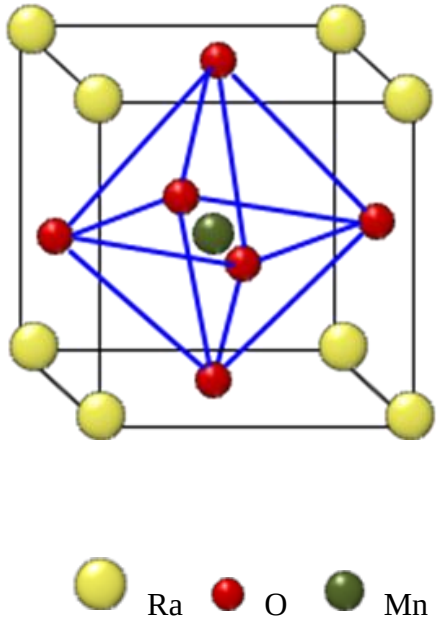

Figure I-1 Schematic view of a cubic unit cell of $RaMnO_3$ in real space. Ra atoms are sitting at the corner of the cubic with one Mn atom in the center. Six oxygen atoms are right in the center of the six cubic side faces.

The large Hund's coupling forces 3 d electrons to occupy the t_{2g} orbitals and 1 electron to occupy the e_g orbital while all their spin are aligned in the same direction. Moreover, in the perovskite structure, the octahedral sub-lattice distortion, called Jahn-Teller distortion, is another important mechanism that again breaks the degeneracy of the e_g and t_{2g} orbitals. This Jahn-Teller distortion is essentially the deformation of oxygen/Mn octahedral. The final electronic configuration of Mn^{3+} is shown as Figure I-2. From Figure I-2, we can see that two electrons are in yz, zx orbital, one in xy orbital and one in $3z^2$-r^2 orbital with all of their spins aligned in the same direction.

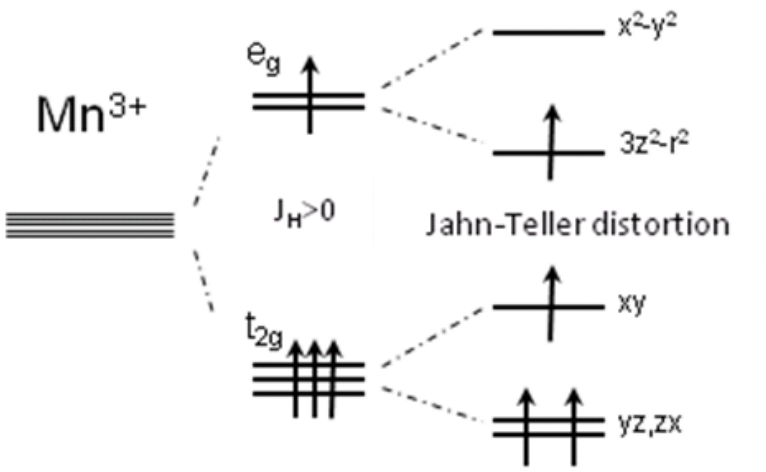

Figure I-2 Schematic view of a Mn^{3+} ion electronic configuration in $RaMnO_3$ cubic unit cell.

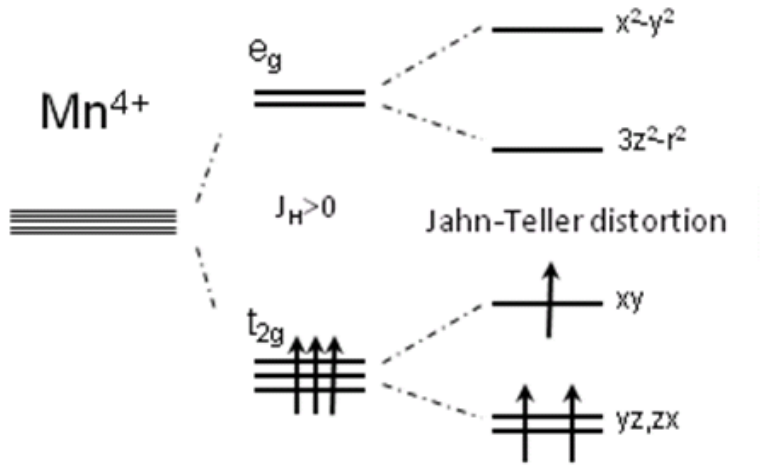

Figure I-3 Schematic view of the Mn^{4+} ion electronic configuration in $La_{1-x}Sr_xMnO_3$ cubic unit cell. Note that there are only 3 d electrons left while e_g orbitals are empty now.

I-2 Alkali Metal Doping and Double Exchange

Because in our case, our specific study object is $La_{1-x}Sr_xMnO_3$, we will initially take a look at the parental compound $LaMnO_3$ which is a Mott insulator because all e_g electrons of Mn are localized due to the large Coulomb repulsion between Mn ions. However, once we introduce Sr dopants to partially replace La atoms in $LaMnO_3$, the physical properties will be greatly different. Since Sr atom can only donate 2 electrons instead of 3 as what La does in $La_{1-x}Sr_xMnO_3$, the Mn ion has to donate one extra e_g electron to maintain the charge neutrality and thus leaving a Mn^{4+} onsite at the unit cell where Sr is introduced. The electronic configuration of a Mn^{4+} is shown in Figure I-3 on the previous page.

In 1951, Zener introduced the DE interaction concept in order to explain the ferromagnetism of perovskites. In a Kondo-lattice type model, the Hamiltonian is:

$$H = -\sum_{ij\sigma} t_{ij} a_{i\sigma}^{+} a_{j\sigma} - J\sum_{i} S_i \cdot M_i \qquad (1)$$

Here S_i is the conduction electron spin and M_i is the localized Mn ion spin [Kaplan *et al.*, 2010]. The first summation represents electron hopping between different sites while the second term represents interaction between hopping e_g electron and local Mn ion spin. The physical picture of DE can be simply described by Figure I-4. Once a Mn^{4+} is created, the e_g electron in Mn^{3+} ion can directly interact with oxygen 2P state. In the following sections, we set the spin direction of Mn ion as our reference direction. The spin-up 2P electron in the oxygen can hop to the adjacent Mn^{4+} site and align the local Mn^{4+} spin in the same direction according to Hund's rule with a vacancy left in oxygen 2P state.

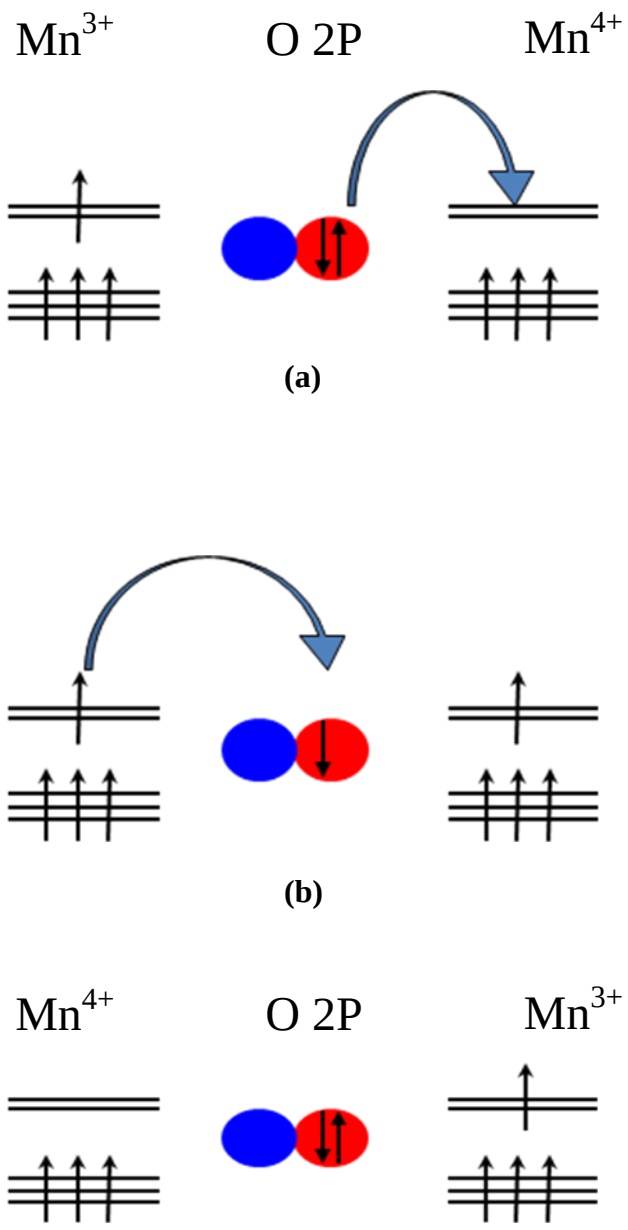

Figure I-4 Schematic view of Double Exchange process (a) Electron in O 2p hops to the adjacent Mn^{4+} (b) Electron in adjacent Mn^{3+} hops to the vacant O 2P state (c) final state after a completed DE process.

Then the e_g electron in the adjacent Mn^{3+} can hop to this oxygen vacant site with the same spin direction. It is essentially a Mn^{3+}–O–Mn^{4+} double-exchange mechanism. In this process the mobile e_g electron can align the local core Mn ion spins ferromagnetically via a strong on-site Hund's coupling and in turn the e_g electrons become more itinerant due to the local spin alignment which essentially reduces the Coulomb repulsion in the same time. Because of the DE interaction, we can expect an e_g electron hopping from Mn^{3+} site to Mn^{4+} site via an oxygen atom intermediary, and this process will not only lead to conduction, but also the alignment of local Mn ion (both Mn^{3+} and Mn^{4+}) spins and consequently, magnetism. This is a simple description of the double exchange process.

I-3 $La_{1-x}Sr_xMnO_3$ (LSMO) Phase Diagram and Magnetism

Sr-doped $LaMnO_3$ is a special oxide compound that has been extensively studied for its relatively high Curie temperature (T_c) and ease of epitaxial growth [Urushibara *et al.*, 1995]. The phase diagram of $La_{1-x}Sr_xMnO_3$ is shown in Figure I-5. We can see that physical properties of LSMO are very sensitive to Sr doping concentration and temperature. When the doping level is within 10%-60%, we have a ferromagnetic (FM) state and the highest T_c is achieved when doping level is located at 33% of Sr concentration. In LSMO bulk material with the optimized Sr doping, its Curie temperature is around 370 K and above this temperature it is in a paramagnetic state. At Sr concentration below 10%, it is in a spin canted antiferromagnetic insulator state.

Because the conduction in LSMO is also from e_g electron hopping, we can expect a strong correlation between its magnetism and conduction. Indeed, people observed that around the Curie temperature, there is also a metal-insulator phase transition in conduction as a function of temperature. This transition temperature is always close to T_c. Figure I-6 shows electrical transport and magnetism properties as a function of temperature of LSMO with a 20% Sr doping level. Below T_c, it has a positive temperature coefficient of resistivity (TCR) while above T_c, its TCR is negative, indicating a metal-insulator transition with the transition temperature close to T_c.

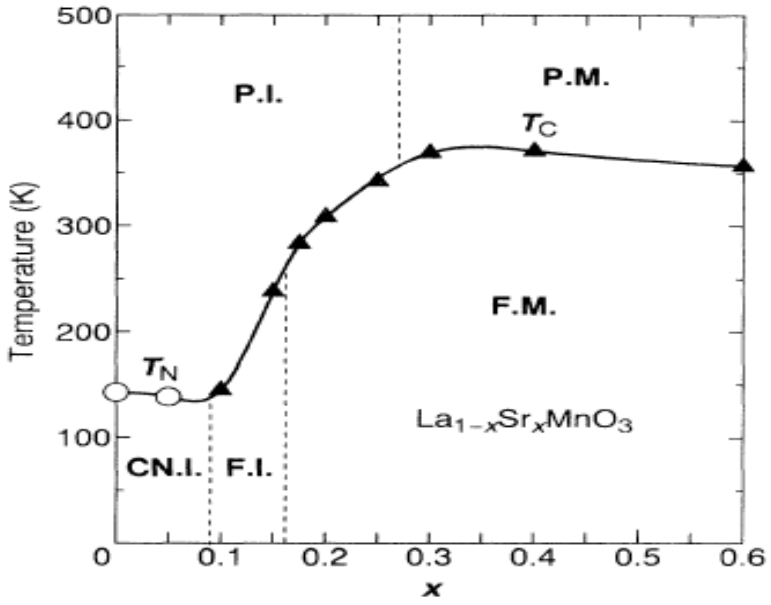

Figure I-5 Phase diagram of LSMO. In the graph, X axis represents Sr doping concentration while Y axis represents temperature. The abbreviations mean paramagnetic insulator (PI), paramagnetic metal (PM), spin-canted insulator (CNI), ferromagnetic insulator (FI) and ferromagnetic metal (FM) [Urushibara *et al.*, 1995].

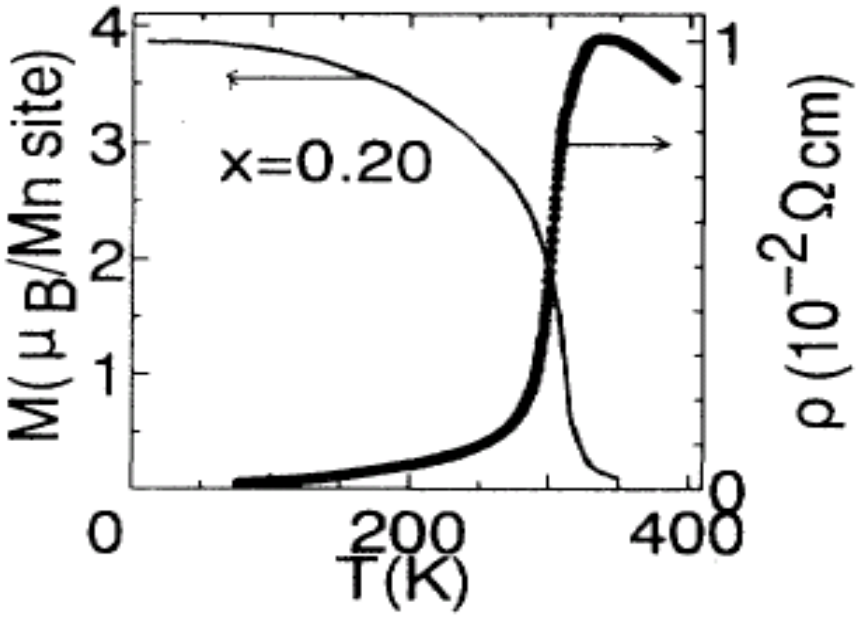

Figure I-6 Correlation between the temperature dependence of resistivity and magnetic moment for LSMO at Sr=20% doping [Urushibara *et al.*, 1995].

I-4 100% Spin Polarization

From the DE model, we can expect that all hopping e_g electrons (conduction electrons) will align the local Mn ion spins in the same direction as the e_g electron spin itself due to the large Hund's coupling energy. We can thus expect that spins of all conduction electrons are aligned along the same direction in the metallic state, i.e, we have a 100% spin polarization (SP) from the conduction electrons SP polarization definition $P = \frac{N_\uparrow - N_\downarrow}{N_\uparrow + N_\downarrow}$ where $N_\uparrow$ and $N_\downarrow$ are conduction electrons density of states (DOS) with spin up and down, respectively.

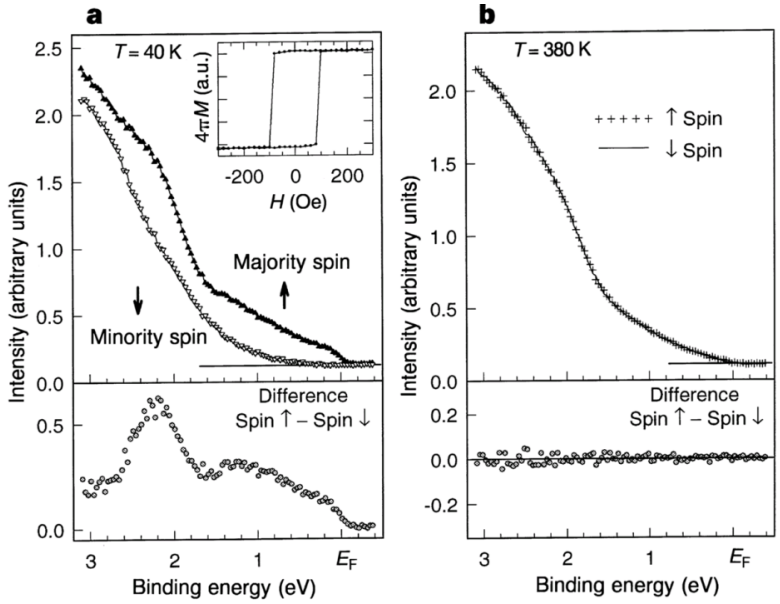

Figure I-7 (a) DOS as a function of energy for spin up and spin down sub bands at 40 K far below T_c. (b) DOS as a function of binding energy for spin up and spin down sub bands at 380 K above T_c. The bottom parts of both graphs show DOS difference between the two spin bands [Park *et al.*, 1998].

In 1998, J. H. Park *et al.* did a famous spin resolved photoemission experiment to directly measure the DOS for the two spin sub-bands independently [Park *et al.*, 1998]. As shown in Figure I-7, we can observe that, below T_c, we have finite DOS only for the spin-up band while the DOS for the spin-down band is zero at the Fermi energy E_F. Below E_F, we have finite DOS for both spin bands and their difference is finite which indicates a net magnetic moment. Above T_c, there is no difference between the two spin bands, leading to zero net magnetic moment. This experiment convincingly shows that LSMO is a half metal within the accuracy of experiments.

I-5 Pulsed Laser Deposition

Pulsed laser deposition (PLD) is a physical vapor deposition (PVD) technique for thin film growth. In principle, a high power pulsed laser beam is focused onto a target material in ultra high vacuum (UHV) chamber so that a plume of target material plasma is excited. The target material is then vaporized from the rotating target and deposit onto a substrate normal to the plume [Wikipedia.org]. For LSMO or $SrTiO_3$ (STO) oxide material growth, this process always takes place in the ambient of oxygen which is commonly used to maintain oxygen stoichiometry. We utilize a homemade PLD UHV system to epitaxially grow high quality oxide thin films and its configuration is shown in Figure I-8. A Coherent Compex Pro. KrF excimer laser that works at 248nm is used as the ablation source.

We start from chemically pure lanthanum oxide La_2O_3, strontium carbonate ($SrCO_3$), titanium oxide (TiO_2) and manganese oxide (MnO_2) to mix them according to the stoichiometric proportions. The stoichiometric ceramic mixture was then sintered using the conventional solid-state reaction method at 1200 ℃ in air. After this, the mixture was reground manally and pressed under 20 MPa. A final sintering was done to get the target pellet. The target is held on a rotation holder controlled by a step motor with a 1 degree/second rotating speed. The base pressure of the UHV chamber is 9×10^{-8} Torr while it is about 7×10^{-3} Torr during growth with Oxygen/Ozone. Due to the chemically active ozone, we can achieve very good oxygen stoichiometry in LSMO films. We utilize a Reflected High Energy Electron Diffraction (RHEED) system to monitor the film crystallinity simultaneously. The following figures show the carton and real picture of our

PLD system.

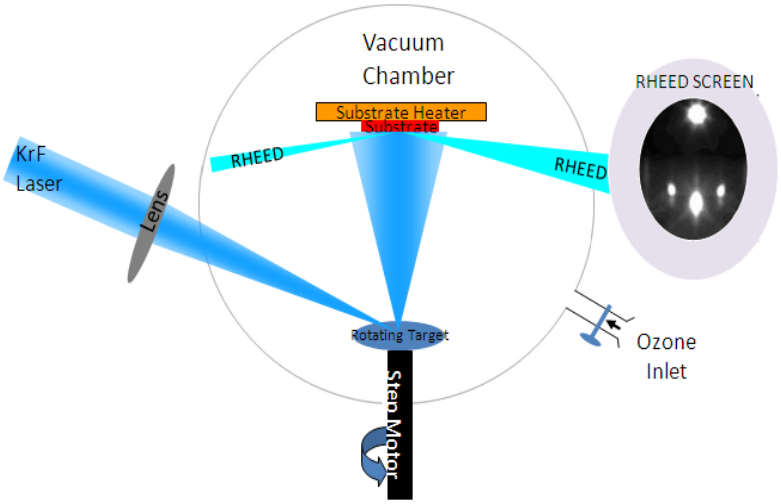

(a)

(b)

Figure I-8: Schematic view of our homemade PLD system (a) Cartoon view of PLD (b) Real picture of PLD at Prof. Jing Shi's lab in Physics Department of UC Riverside.

Compared to other thin film deposition techniques, particularly MBE technique, the basic setup of PLD is relatively simple while the quality of the grown material is very high. Many materials can be deposited epitaxially at a fast rate. However, the physical process of laser-target interaction and film growth are quite complex. When the laser pulse energy is absorbed by a target material, the energy of the light is first converted to electronic excitations and then into thermal, chemical and mechanical energies giving rise to evaporation, ablation, plasma formation and even physical exfoliation of the target material [Wikipedia.org]. These species will expand into the surrounding vacuum in the form of a plume and deposit onto the typically hot substrate surface. Simply, there are four stages involved in the film growth process [Wikipedia.org]: first, target material plasma is created by laser ablation followed by the second stage which is the dynamic evolution of the plasma plume itself. The third state involves the deposition of the target material onto a substrate surface and finally, nucleation process takes place on the surface of substrate and thin film is formed. All these stages together determine the stoichiometry, uniformity and crystallinity of the final film. During growth, there are several critical physical parameters that determine our final film quality.

Laser energy: typically we use 160mJ/pulse at the frequency of 1-3Hz. This laser energy parameter is critical to fully excite the target material plasma with good stoichiometry and target material flux density. Typically, the material flux density increases as the laser energy increases and low laser energy will result in off-stoichiometry in the final film.

Substrate temperature: Substrate temperature has a great impact on the film

crystallinity. Specially, for LSMO on STO, we maintain our substrate at a temperature of ~800-850 ℃.

Substrate surface morphology: typically, the surface flatness/crystallinity condition determines the nucleation process and growth of film. We use chemically etched STO substrate with well defined atomic terrace structure and LSMO can be easily epitaxilly grown on it.

Background pressure: for LSMO oxide material, oxygen deficiency is a common reason that results in low magnetism, poor crystallinity and low T_c. In our case, we maintain the oxygen pressure at ~1 mTorr with a 12 wt% of ozone which produces films with little oxygen deficiency and a high T_c in the as-grown state.

During LSMO growth, we always observe three typical growth modes which critically depend on the deposition parameters [Ma *et al.*, 2009]. The very first common growth mode is the layer-by-layer growth mode. With our atomically flat substrates and the ozone atmosphere at 850 ℃, we can readily obtain this growth mode of LSMO on STO. In this mode, the LSMO nucleation process continues until a full layer of LSMO is formed and then a new nucleation process takes place for the next layer. We utilize RHEED technique to monitor this process. The RHEED diffraction pattern indicates the morphology and crystallinity of LSMO film while the RHEED intensity oscillation as a function of the growth time shows how many layers have been grown.

In reality, when people polish the top surface of STO substrate, there is always a miscut angle (in our case it is typically <0.5 °). Once we chemically etch the STO substrate and anneal it in ozone, we always obtain atomic terraces as well as steps

between terraces. At high temperature (>900 ℃), LSMO species deposited on the surface of LSMO tend to diffuse to the edge of those terraces and start to nucleate there. During this process, the RHEED intensity does not change significantly and RHEED pattern maintains the same all the time. It is just like that there are many steps flowing across the surface. Finally, a 3-dimensional island growth mode could be observed if the sample is grown under a low oxygen pressure, low temperature or low laser energy power. This island growth mode leads to a polycrystalline film and a rough film surface.

Reference

Chatterji, T., Colossal Magnetoresistive Manganites **(Book, Edition 1)** (2004).

Tokura, Y. *et al.*, Annu. Rev. Mater. Sci. **30**, 451 (2000).

Coey, J. M. D. *et al.*, Advances in Physics **48**, 167 (1999).

Zener, C., Phys. Rev. **81**, 440 (1951), Phys. Rev. **82**, 403 (1951) and Phys. Rev. **83**, 299 (1951).

Kaplan, T. A. *et al.*, Physics of manganites **(Book)** (2010).

Urushibara, A. *et al.*, Phys. Rev. B **51**, 14103 (1995).

Park, J. H. *et al.*, Nature **392**, 794 (1998).

http://en.wikipedia.org/wiki/Pulsed_laser_deposition.

Ma, J. X. *et al.*, Phys. Rev. B **79**, 174424 (2009).

Chapter II

Orientation Dependent Interface Magnetism

II-1 Introduction

From the previous sections we learned it is DE that leads to conduction and ferromagnetism in LSMO or other similar manganites. An external magnetic field helps align local spins of Mn ions and promote hopping of e_g electrons between them, and consequently this gives rise to a lower resistivity. Indeed, in manganites like LSMO, the resistivity is greatly suppressed under an external magnetic field [Haghiri-Gosnet *et al.*, 2003]. This suppression reaches maximum around T_c and magnetoresistance can achieve as high as 100% at 15 T. This large magnetoresistance is called colossal magnetoresistance (CMR) [Volger, 1954]. What is the mechanism behind for the colossal magnetoresistance? When the magnetic transition temperature is approached from below, the spins tend to lose the alignment, but an external magnetic field helps align neighboring spins; e_g electron hopping from Mn^{3+} ion to neighboring Mn^{4+} is therefore promoted.

For manganites, the ferromagnetic interface/surface in which the spins are aligned is the most desired property for potential spintronic device applications. In a prototype model system, i.e. LSMO/STO/LSMO magnetic tunnel junction (MTJ), previous studies have mainly focused on this MTJ in (100) orientation probably due to the simplicity of epitaxial growth [Lu *et al.*, 1996; Sun *et al.*, 1996; Ishii *et al.*, 2005; Bowen *et al.*, 2003].

So far, all experimental results show that the interface magnetism between the STO barrier and bottom LSMO layer is significantly suppressed due to the inherent antiferromagnetic (AFM) coupling resulted from charge transfer (CT) or orbital ordering (OO) occurring at the interfaces. Its interface average magnetic moment and Curie temperature are much lower than that of bulk states [Lu *et al.*, 1996; Sun *et al.*, 1996; Ishii *et al.*, 2005; Bowen *et al.*, 2003]. It is argued that the charge transfer could be compensated by modifying interface doping profile, the strain and/or symmetry-breaking induced orbital ordering which is orientation-dependent and thus intrinsic to the (100) interface [Yamada *et al.*, 2006; Tebano *et al.*, 2008]. This intrinsic AFM coupling of (100) interface was attributed to the reduced tunneling magnetoresistance (TMR) and its steep temperature dependence in devices made in (100) orientation.

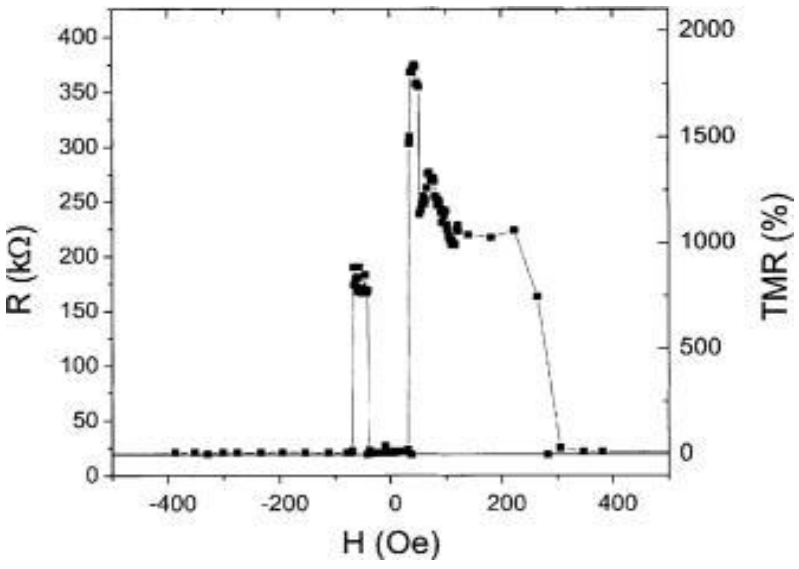

Figure II-1 Tunneling magnetoresistance in LSMO/STO/LSMO (100) at 4.2 K from Bowen *et al.*, [Bowen *et al.*, 2003].

Figure II-1 shows a great example from M. Bowen *et al.* in a LSMO/STO/LSMO MTJ with (100) orientation [Bowen *et al.*, 2003]. Indeed, they observed a TMR ratio as high as 1800% at 4.2 K which corresponds to a spin polarization of LSMO ~95% at the interface. However, if we look at the temperature dependence of TMR, we notice that it decays very fast and down to zero at about 250 K. Compared with the LSMO film T_c which is ~ 350 K, TMR can only persist up to a temperature much lower than LSMO film T_c. We propose an interface polarity discontinuity model to explain this phenomenon and perform interface magnetism measurements in a systematic study. Our argument is that the (110) oriented interface between STO and bottom LSMO will have much more robust ferromagnetism than its (100) oriented counterpart, since the polarity discontinuity does not exist at the interface between LSMO and STO in (110) orientation [Figure II-2]. Thus CT is reduced and OO is unfavorable, which leads to highly enhanced interface ferromagnetism.

In order to measure the interface electrical and magnetic properties at the interface between STO/LSMO in (110) orientation, first we utilize the superlattice approach to study this system [Ueda *et al.*, 1998; Brinkman *et al.*, 2007; Takahashi *et al.*, 2001]. We synthesized a series of SL samples consisting of $La_{0.7}Sr_{0.3}MnO_3$ and non-magnetic insulator STO in (110) orientation. By changing SL periodicity, we can effectively tune the interface-to-bulk ratio, which allows us to measure the absolute value of the interface magnetic moment. In a series of (110)-oriented $La_{0.7}Sr_{0.3}MnO_3/SrTiO_3$ superlattices, we demonstrate that robust ferromagnetism persists down to 4 monolayers (MLs) (~1.1 nm in thickness), of which 50% Mn is at the interface state. Above 8 MLs, the magnetic

moment is nearly saturated to the theoretical value of 3.7 μ_B per Mn ion, with the interface moment of ~3.2 μ_B per Mn ion. In contrast to (100) interface that is prone to strong spin canting due to the intrinsic AFM coupling, (110) interface is ferromagnetic possessing a higher magnetic moment.

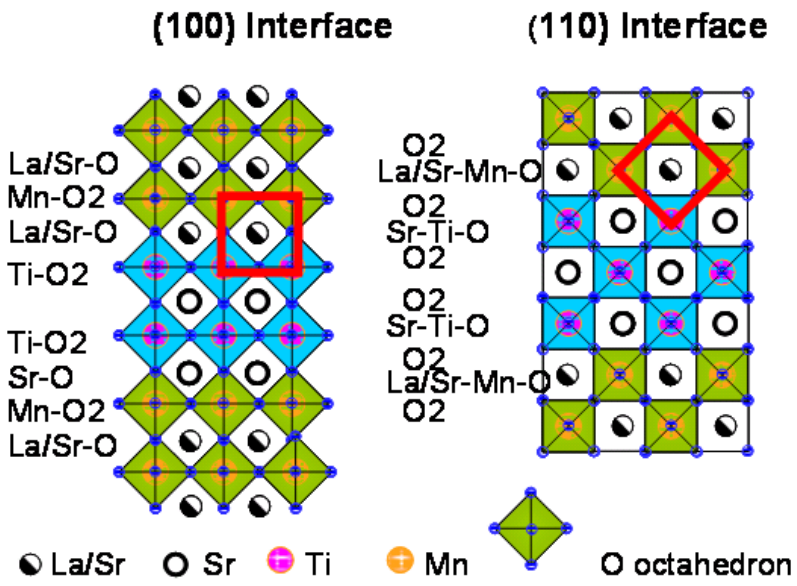

Figure II-2 Schematic view of LSMO/STO/LSMO hetero-interfaces. The upper interface LaSr-O/MnO_2/Sr-O is different from the lower interface LaSr-O/MnO_2/LaSr-O for (100) orientation. Both interfaces are identical: O_2/LaSrMnO/O_2 for (110) orientation.

II-2 Sample Preparation and Measurement

The (110)-oriented (LSMO[N]/STO[3])p SL (denoted as N-(110)SL) samples were grown in our newly developed PLD system. The STO insulating spacing layer is fixed at

3 ML (110) (~ 0.81 nm in thickness), whereas the number of the LSMO atomic layers N varies from 3 to 15 ML in each SL unit while the total number of LSMO layers in the entire SL is kept close to 100 ML (110). In this way, we can make quantitative comparison between different SLs with different LSMO unit thickness. A 100 ML (110) LSMO film capped with a 3 ML (110) STO was also separately grown as a reference bulk sample. In the same time we also prepared several (100)-oriented SL (denoted as N-(100)SL) samples with intentionally chosen LSMO thicknesses in order to make direct comparison with the (110) counterparts.

Commercially available STO(110) substrates from Crystec were ultrasound-cleaned in acetone and in-situ annealed in 10^{-5} Torr ozone atmosphere at 800℃-850℃ for 30-60 minutes. With this modified substrate treatment procedure, we always observe a sharp RHEED pattern which indicates a high quality and flat STO(110) substrate surface. The growth temperature was kept at 800℃-850℃ and the oxygen pressure was 1 mTorr with 12 wt% of ozone. Under this condition, we can always obtain a well defined layer-by-layer growth mode as indicated by the RHEED intensity oscillation [Figure II-3]. LSMO growth condition was optimized that its Curie temperature T_c is ~340 K and the saturation magnetic moment Ms~3.7 μ_B/Mn in the as-grown 100 ML LSMO thin film. In order to ensure sharp interfaces and minimize the inter-diffusion between STO and LSMO units, interval annealing was deliberately performed between the growth of LSMO and STO until the RHEED intensity was fully recovered. This procedure was repeated so that the RHEED oscillation intensity was maintained approximately constant throughout the growth process. Following this procedure, the post-growth RHEED

pattern was almost the same as that of the pre-growth, and the Kikuchi lines were clearly visible, as shown in Figure II-4.

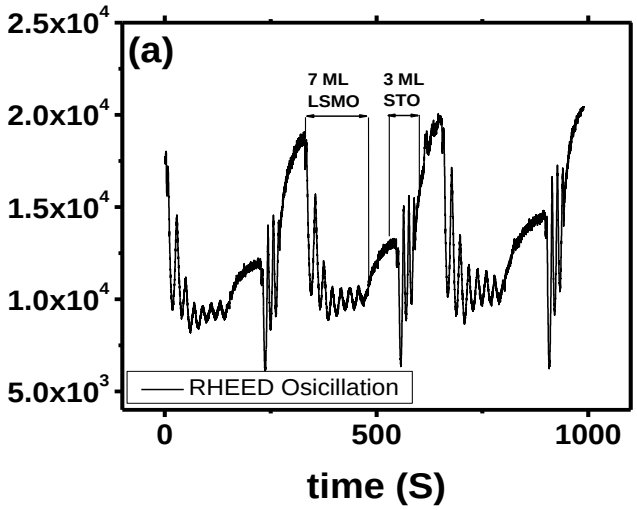

Figure II-3 RHEED intensity oscillation as a function of time. Data shown here is for SL with [LSMO(7ML)/STO(3ML)]$_{14}$/STO(110).

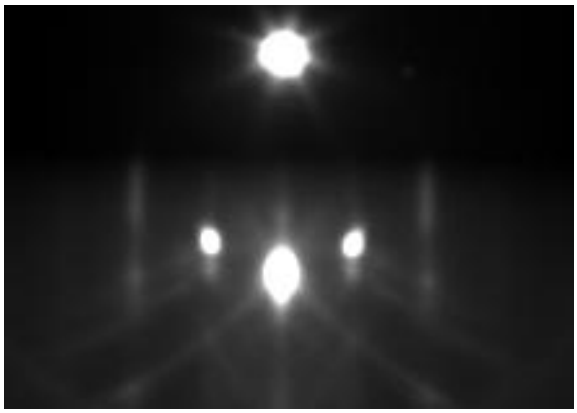

Figure II-4 RHEED pattern of one SL after growth. Data shown here is for SL with [LSMO(7ML)/STO(3ML)]$_{14}$/STO(110). STO substrate shows almost the same RHEED pattern.

High resolution transmission electron microscopy (HRTEM) shows an excellent SL layered structure with good periodicity [Figure II-5]. Beside this, we also performed X-ray diffraction (XRD) experiments. As shown by Figure II-6, in addition to the two main peaks from STO substrate, we also obtain clear SL satellite peaks confirming good SL crystallinity and periodicity.

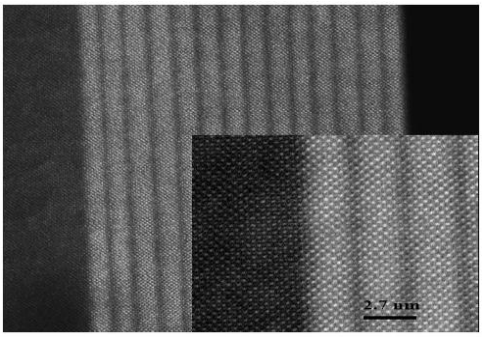

Figure II-5 Z-contrast TEM image of 7-SL samples with 14 periodic units in full range. Inset is the high-resolution image taken near the substrate. The bright and dark regions correspond to LSMO and STO, respectively.

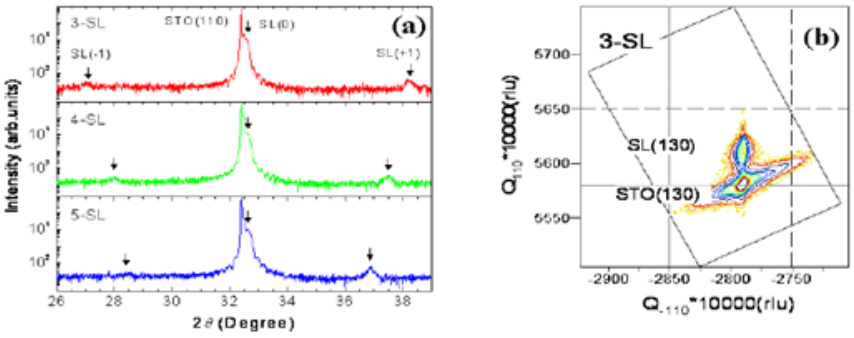

Figure II-6 X-ray diffraction (XRD) spectra for SL samples with 3, 4 and 5 ML LSMO periodic units, respectively.

Magnetic properties of SL samples are measured with the SQUID magnetometry, and transport properties are measured by the standard 4-terminal method. In 4-terminal transport measurement, 4 gold wires are uniformly attached by silver paint on the top surface of SL samples and all the measurements are done in a Janis Research closed-cycle cryocooler system either by a DC or an AC technique.

II-3 Experimental Results

First of all, we measure the magnetic moment of all SLs as a function of temperature with the SQUID magnetometry technique. Figure II-7 (a) shows temperature dependence of the measured magnetic moment M of all SL samples. The magnetic moment was measured during warming-up in a magnetic field of 500 Gauss applied along the in-plane [001] direction upon zero field cooling. After the magnetic moment measurements, we perform the standard 4-terminal measurements for SL resistivity. Figure II-7 (b) shows the temperature dependences of resistivity ρ for all SL samples. The resistance was measured at zero magnetic field and the resistivity was calculated based on the total number of LSMO layers as well as the SLs aspect ratio. The electrical current was set along the [001] axis. In M versus T curves, we can clearly observe ferromagnetic to paramagnetic transitions in all SL samples with LSMO thickness above 4ML except for the 3ML LSMO -(110)SL that shows weak magnetism. Metal-Insulator (MI) transitions are also observed for samples with LSMO above 6 ML in (110) orientation, but samples below 5 ML (110) show insulating behaviors only. From these results, we can extract the interface magnetic dead layer thickness. In (110) oriented interface between STO and

LSMO, the total magnetic dead layer thickness is 3 ML (110) (~ 0.82 nm) which is equivalent to the thickness of 2.1 ML (100) in (100) orientation. On the other hand, the electric dead layer is 5 ML (110) thick (~ 1.37 nm) that is equivalent to a thickness of 3.7 ML in (100) orientation.

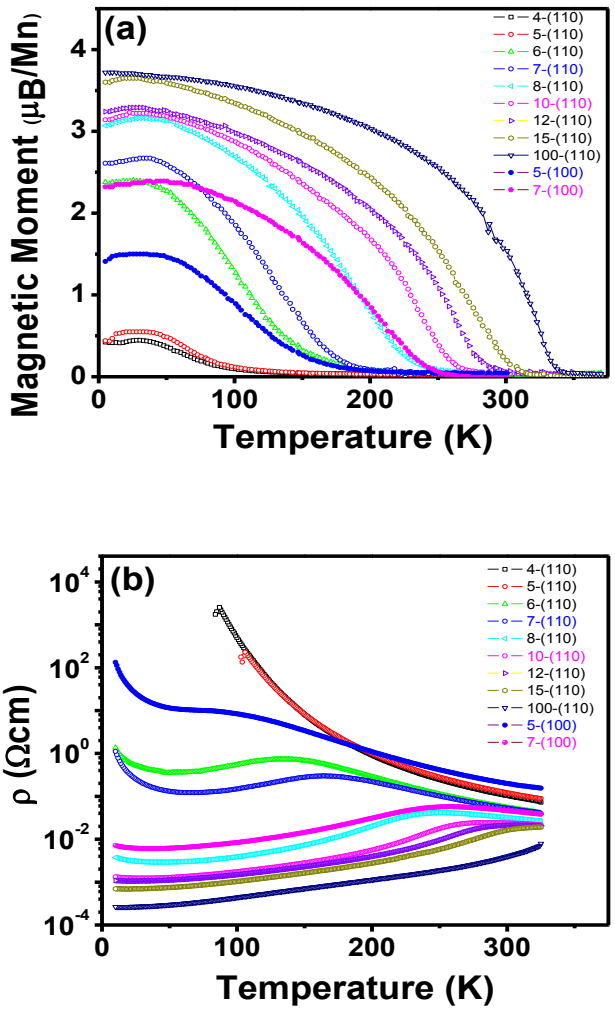

Figure II-7(a) Temperature dependence of magnetic moment M for SLs measured during field warming (0.05T along [001]) upon zero field cooling (b) Temperature dependence of resistivity ρ measured at zero magnetic field. Resistivity is normalized by the total number of LSMO layers.

To study the spin state of the interfaces, we measured the magnetic field dependence of the SL moments at 5 K, as shown in Figure II-8 for different LSMO unit thickness SLs. Well-defined hysteresis loops were observed for all SL samples with LSMO above 4 ML (110).

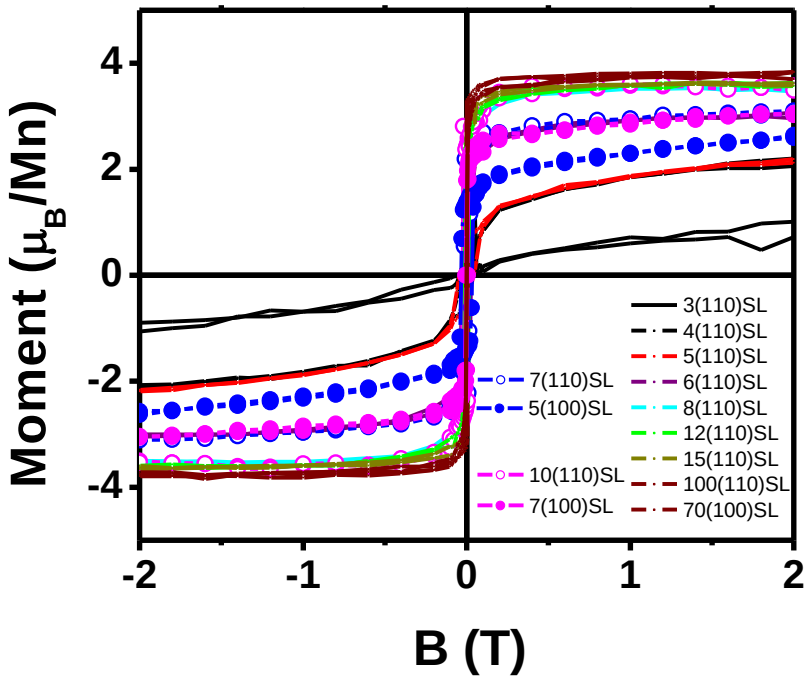

Figure II-8 Magnetic hysteresis loops of (110) SL samples measured at 5 K. (100) oriented SLs are also presented here at two selected unit thickness: 5ML and 7ML LSMO.

For a 100 ML (110) LSMO single thin film (~27 nm in thickness), the observed saturation M is 3.75 μ_B/Mn, which is close to the theoretical value of 3.7 μ_B/Mn, demonstrating that the 100 ML LSMO thin film can recover the bulk magnetic property.

When we decrease LSMO unit thickness (increase interface/bulk ratio), the measured saturation moment M decreases steadily. For samples with LSMO above 8 ML (110), M reaches saturation at 0.5 T, indicating that both inner layer and interface moments are saturated. The saturation moment only lightly increases with increasing LSMO thickness. Below 7 ML (110), the saturation moment decreases very rapidly as we decrease LSMO unit thickness, indicating that moment of both the inner layers and the interface layers decreases and the total interface layers are around 7 ML. We will come back to this point later. For 3-(110)SL, the remanent moment approaches zero, although a sizable saturation M of 0.9 μ_B can be detected at 2 T.

In manganites, ferromagnetic spin-spin interaction is mediated by the DE interaction between the nearest Mn ions through oxygen atoms and thus the interface effects become important within the charge screening length scale [Hong *et al.*, 2005], above which the magnetic moment approaches to the bulk value. Kavich *et al.* studied the interface moment profile for (100) oriented LSMO films and found that the magnetic moment gradually increases and reaches saturation state at 6 ML (100) [Kavich *et al.*, 2007]. To our knowledge, there is no such an experimental or theoretical study on (110) interfaces between STO and LSMO. Here we adopt a similar profile analysis approach for (110)-oriented interfaces as illustrated in the inset of Figure II-9. Above a critical thickness, the inner layers reach saturation at temperatures sufficiently lower than T_c. Suppose that the total thickness of each LSMO unit cell exceeds its total dead layer thickness. Each LSMO unit has nominal thickness t (number of layers), and each unit has a t_0 layers dead layer (completely dead).

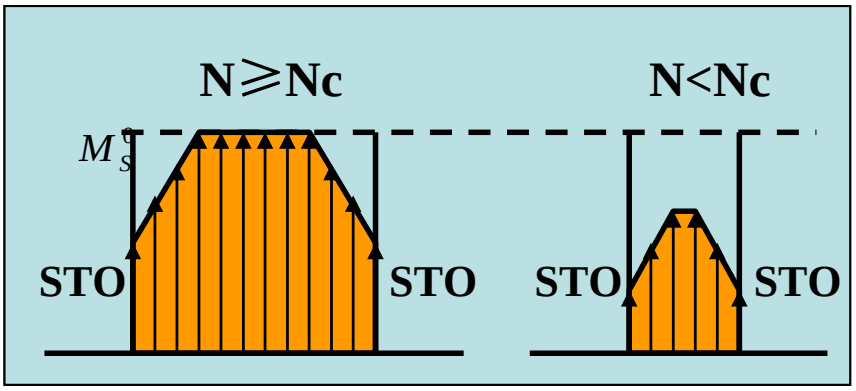

Figure II-9 Magnetic moment profile as a function of LSMO unit thickness in Superlattices.

The total number of units is N, and the total number of LSMO layer is fixed at N_0. So $N \times t = N_0$. Each live layer contributes M_0 to the total magnetic moment. Then the total measured moment M can be expressed as: $M = M_0 \times N \times (t - t_0)$. In addition, we assume that the interface moment profile remains the same as the LSMO thickness varies; therefore, the total loss of moment from the interfaces remains constant if the total LSMO thickness exceeds the total interface state thickness. Based on this, we can obtain: $\left(M_S^0 - M_S\right) \cdot t = 2a$, where M_S is the measured saturation moment per Mn ion at 2 T; t is the number of LSMO layers in one SL unit; *a* is the total moment loss associated with one interface and the factor of two takes care of the two interfaces. Thus, we have $M_S = M_S^0 - 2a/t$, i.e. the measured saturation magnetic moment per Mn ion is a linear function of 1/t if the inner layer moment is fully saturated. Figure II-10 shows the average saturation moment vs. 1/t curve measured at 5 K and it clearly follows a straight line for $t \geq 8$.

By linear fitting, we obtain: *Ms*=3.76±0.013 μ_B, and a=0.98±0.077 μ_B. *Ms* is very close to the ideal value 3.7 μ_B/Mn. When LSMO is below 6 ML (110), the data departs sharply from the linear behavior, which indicates a crossover thickness of 6 ML (110) below which the entire LSMO is in the interface state. If we attribute the total moment loss to all LSMO layers in the SL, then the average moment loss of this 3 ML (110)-thick interface is found to be a/3=0.33 μ_B per Mn ion, which accounts for about 8.8% of the saturation value of 3.7 μ_B/Mn. For the assumed linear profile, the magnetic moment starts from 3.2 μ_B at the outmost interface, which is as high as 87% of inner layer moment, and restores to its full value of 3.7 μ_B at the fourth layer from the interface.

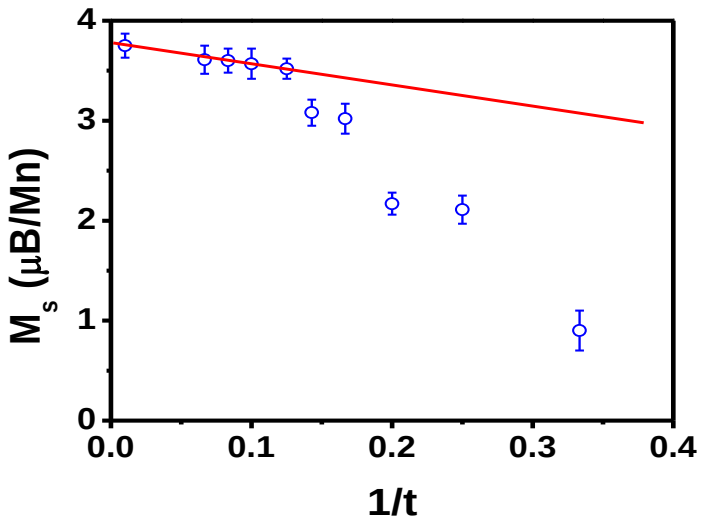

Figure II-10 Saturation magnetic moments at 2 T vs. 1/t, where t is the number of LSMO SL layers in a SL unit. The red line represents linear fitting $M=M_0-2a/t$. Above the critical thickness of 8 MLs, the inner layer moment is saturated to M_0 and the total loss of the interface moment remains fixed as the LSMO thickness varies. Below 8 MLs, the magnetic moments of both the inner and interface layers decrease with decreasing thickness.

In order to make direct comparisons, we also grow three (100)-oriented SL samples with same LSMO unit thicknesses and periodicities as those in the (110) SL samples. The 70-(100)SL, 7-(100)SL, and 5-(100)SL samples correspond to 100-(110)SL, 10-(110)SL, and 7-(110)SL samples respectively. The magnetic and transport properties are summarized in Table II-1.

SL component	*Ms* (μ_B)	M_0 (μ_B)	T_c (K)	T_p (K)	ρ ($\Omega \cdot cm$)
7-3-110	3.08	2.2	180	164	0.059
5-2-100	2.55	1.38	165	<85	0.23
10-3-110	3.57	2.5	265	285	0.024
7-2-1-100	3.0	1.8	245	258	0.050
100-3-110	3.75	3.3	337	$>T_c$	0.0033
70-2-100	3.76	2.1	330	$>T_c$	0.0044

Table II-1 Direct comparison of magnetic and transport properties between (100)- and (110)-oriented SL samples with same thickness and periodicities. The overall properties of (110)-oriented SLs are dramatically superior to that of (100)-oriented SLs.

Figure II-7 and Figure II-8 show the comparative M~T and ρ~T of (100)- and (110)-oriented samples with different LSMO thicknesses respectively. For 70-(100)SL and 100-

(110)SL (27 nm in thickness in both films), the observed saturation M are 3.80 and 3.75 μ_B per Mn ion, respectively, which are close to the theoretical value of 3.7 μ_B. The FM transition temperatures are 337 K and 330 K respectively. It demonstrates here that the bulk properties are recovered in both films. The T_c's of (100)-oriented SLs are consistently lower than those of (110)-oriented SLs at the same LSMO unit thickness. Magnetic moment of 5-(100)SL and 7-(100)SL is about 2.6 μ_B and 3.1 μ_B per Mn ion, respectively. These experimental moment values are consistent with previous reported values in literatures [Sahana *et al.*, 2001; Izumi *et al.*, 2001; Izumi *et al.*, 2001]. The reduction in moment per Mn ion (averaged over both inner and interface Mn ions) is 1.15 μ_B and 0.7 μ_B respectively for 5-(100)SL and 7-(100)SL samples, which are considerably larger than those of (110) counterparts (0.62 μ_B and 0.13 μ_B for 7-(110)SL and 10-(110)SL respectively). If we consider a more realistic interface profile, we may expect a greater reduction in interface moment at the (100) oriented interface. Additionally, the remanent moments are about 37% and 28% lower in (100)-oriented SLs than those in (110)-oriented SLs, suggesting strong spin canting state at (100) interfaces.

Because of the DE interaction, there is a strong correlation between the magnetism and conductivity in LSMO. We may expect a similar contrast in conduction behavior between (100) and (110) oriented interfaces. Indeed, we also observe remarkable differences in resistivity versus temperature behavior between (100)- and (110)-oriented SLs. 5-(100)SL sample shows an insulating behavior which suggests FM/AFM phase separation, whereas its (110) counterpart 7-(110)SL still shows a FM metallic behavior [Figure II-7 (b)]. This ferromagnetic metallicity behavior persists down to the 6-(110)SL,

which is twice as much as that of (110) interface state thickness as estimated from the linear fitting above. Interestingly, if we look at the resistivity ratio ρ(100)/ρ(110), we will find that it is nearly constant below T_c, as shown in Figure II-11. The resistivity ratio between different orientation SLs are 100 and 5 below T_c, respectively for 5-(100)SL/7-(110)SL and 7-(100)SL/10-(110)SL. These experimental results confirm that (110) oriented interface has more robust ferromagnetism and metallicity than (100) oriented interface.

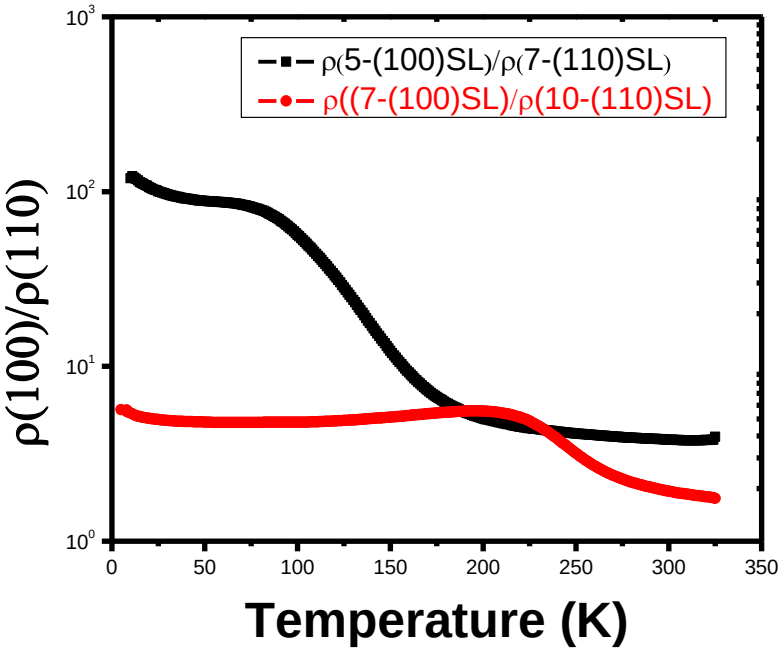

Figure II-11 Resistivity ratio of (100)- and (110)-oriented SL samples vs. T curves respectively for 5-(100)SL/7-(110)SL and 7-(100)SL/10-(110)SL.

II-4 Discussion

In the sections above, we qualitatively show that the (110) interface between STO and LSMO possesses more robust ferromagnetism and metallicity than its (100) oriented counterpart. We will discuss the possible underlying mechanisms of the observed strong ferromagnetism of (110) interface in this section. It is noted that (100) interface state is 6 ML (100) thick which approximately corresponds to 2.4 nm, nearly an order of magnitude larger than the Thomas-Fermi screening length L_{TF} which is ~ 0.3 nm only in LSMO, and the magnetic moment is only 40% of the bulk value. In a stark contrast to (100) oriented interface, for (110) oriented interface, the interface state is 3 ML (110) thick (~ 0.8 nm only) which is only about three times of L_{TF} ~ 0.3 nm and the magnetic moment is as high as 87% of the bulk value. This saturation interface moment is even larger than the moment at $LaMnO_3$ modified interface (~ 80%). These hard facts strongly suggest for (110) oriented interface the charge density modulation is the primary factor that determines its interface magnetism/metallicity. On the contrary, for (100) interface, other mechanisms than the charge density modulation must also play a decisive role in the suppressed interface magnetic state.

In a perovskite material with ABO_3 layered structure, each A ion is surrounded by eight B ions. As shown in Figure II-2, the red square indicates the La/Sr ions inside are surrounded by Mn and Ti ions at the interfaces. The Mn:Ti atom number ratio is 4:4=1 at the (100) oriented interface while this ratio is 6:2=3 at the (110) oriented interface. If we assume that the doped holes from La/Sr ions have equal chances going into Mn and Ti sites, then we can easily see that the charge transfer probability of Mn ion at (110)

interface is approximately half of that at (100) interface. It has been theoretically and experimentally confirmed that over-doping near the interface induced by CT is a major factor resulting in the suppression of interface magnetism [Zenia *et al.*, 2007], hence it is not surprising that the Mn ion moment at (110) interface is higher. In addition, because of preferential occupation in d_{z^2} or $d_{x^2-y^2}$ orbitals due to spin orbital coupling and crystal field, there is an orbital ordering with C- or A-type AFM configuration reported in literature resulted from the symmetry breaking and/or the strain effects at the (100)-oriented interface/surface of LSMO/STO. For the (110) oriented interface, however the crystal field variation due to the strain effects and/or symmetry-breaking is along [110] direction. The consequence of this twisted strain is it will not cause preferential occupation of e_g orbitals any more, i.e. e_g electrons are not forced to stay in the d_{z^2} or $d_{x^2-y^2}$ orbitals. Thus d_{z^2} or $d_{x^2-y^2}$ orbital ordering and consequently the AFM coupling are not favorable at the (110)-oriented interface/surface. Thirdly, there are two oxygen atoms between the adjacent (110) layers but only one between the adjacent (100) layers, as a result, the interlayer Mn-O-Mn DE coupling is stronger for (110). On the whole, for (110) interface, AFM coupling is intrinsically unfavorable. Weaker DE coupling strength at the interfaces could be mainly due to the reduced coordination number of Mn ions and the modulated charge profile. Note that the (110) FM properties may be further improved using similar strategy proposed by Yamada *et al*. However, greater CT and additional inherent AFM coupling due to the strain and/or orbital ordering make (100) interface inferior to (110) interface.

In summary, high quality (110)-oriented LSMO/STO SLs have been successfully

fabricated. We have demonstrated that the (110)-oriented LSMO/STO interface is intrinsically FM with a significantly higher magnetic moment (only about 8.8% lower than the saturation moment), which holds a great promise for spintronic applications. In addition, we emphasize that (110)-oriented interfaces have identical atomic arrangements and are anisotropic in [1-10] and [001] directions, which has unique merits for potential technological applications. We believe that (110)-oriented SL is a unique system for studying other strongly correlated electron systems [Ma *et al.*, 2009].

Reference

Haghiri-Gosnet, A. M. J. Phys. D: Appl. Phys. **36**, R127 (2003).

Volger, J., Physica **20**, 49 (1954).

Lu, Y. *et al.*, Phys. Rev. B **54**, R8357 (1996).

Sun, J. Z. *et al.*, Appl. Phys. Lett. **69**, 3266 (1996).

Ishii, Y. *et al.*, Appl. Phys. Lett. **87**, 022509 (2005).

Bowen, M. *et al.*, Appl. Phys. Lett. **82**, 233 (2003).

Ueda, K. *et al.*, Science **280**, 1064 (1998).

Brinkman, A. *et al.*, Nature Materials **6**, 493 (2007).

Takahashi, K. S. *et al.*, Appl. Phys. Lett. **79**, 1324 (2001).

Hong, X. *et al.*, Appl. Phys. Lett. **86**, 142501 (2005).

Kavich, J. J. Phys. Rev. B **76**, 014410 (2007).

Sahana, M. *et al.*, J. Appl. Phys. **89**, 6834 (2001).

Izumi, M. *et al.*, Phys. Rev. B **64**, 064429 (2001).

Izumi, M. *et al.*, Mater. Sci. & Eng. B **84**, 53 (2001).

Zenia, H. *et al.*, New J. Phys. **9**, 105 (2007).

Main contents in this section were published in Phys. Rev. B **79**, 174424 (2009).

Chapter III

Interface Engineering in Magnetic Tunnel Junction

III-1 Introduction

Magnetic tunnel junctions (MTJs) are the fundamental elements of hard disk drive and spin based non-volatile memory. Development of magnetic tunnel junctions has been driven for decades both by fundamental research and magnetic data storage/recording industry application appeal. The basic structure of a MTJ consists of an insulating barrier sandwiched by two ferromagnetic layers which have different coercive fields [Figure III-1]. The insulating layer is so thin that once we apply a bias voltage between the two ferromagnetic layers, electrons can tunnel through this insulating barrier layer [Tsymbal *et al.*, 2003]. In MTJs, at a certain bias voltage, the tunneling current depends on the relative orientation of magnetizations in the two ferromagnetic layers, and therefore the junction resistance itself depends on the relative orientation of magnetizations in the two ferromagnetic layers. We can control the magnetization configuration i.e. the logic state with an external magnetic field. Specifically, when the magnetizations of the two ferromagnetic layers are parallel to each other, we have resistance state denoted as R_P or $R_{\uparrow\uparrow}$ while we have junction resistance of R_{AP} or $R_{\uparrow\downarrow}$ in the anti-parallel state. This spin-dependent tunneling junction resistance is called tunneling magnetoresistance (TMR). The corresponding TMR ratio is defined as: $TMR = \frac{R_{\uparrow\downarrow} - R_{\uparrow\uparrow}}{R_{\uparrow\uparrow}}$. According to Julliere

model [Julliere, 1975], the tunneling magnetoresistance ratio can be simply described by $TMR = \frac{R_{\uparrow\downarrow} - R_{\uparrow\uparrow}}{R_{\uparrow\uparrow}} = \frac{2P_1P_2}{1-P_1P_2}$ where P_1 and P_2 are bulk spin polarization (SP) of the two ferromagnetic electrodes, respectively.

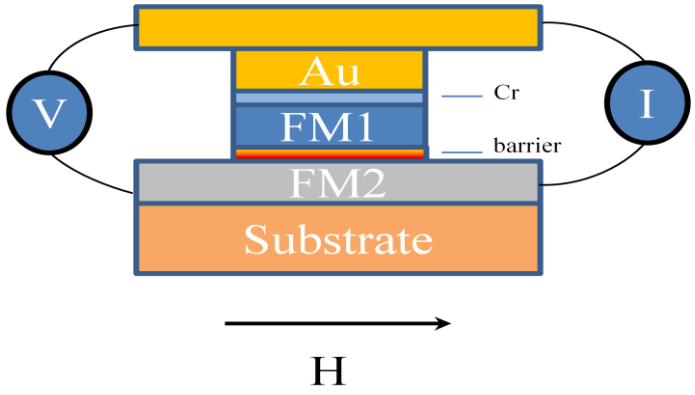

Figure III-1 Schematic view of a typical MTJ structure and its TMR measurement geometry in our experiments.

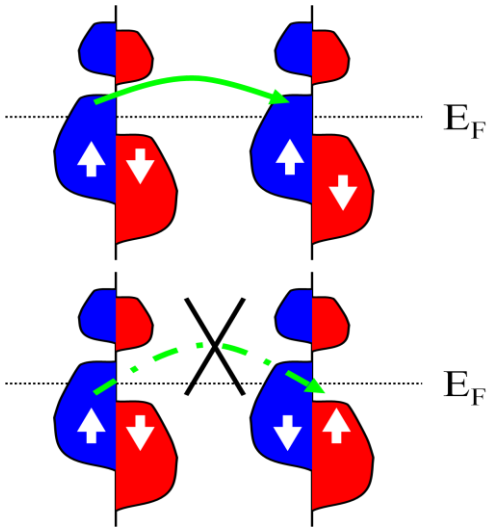

Figure III-2 Schematic view of a typical MTJ band structure and spin dependent tunneling.

In the original work of Julliere, the spin polarization in the ferromagnetic electrode is simply the difference of the density-of-states (DOS) in spin-up and spin-down sub-bands divided by their sum. In other words, SP can be written as: $P = \frac{N_{\uparrow}(E_F) - N_{\downarrow}(E_F)}{N_{\uparrow}(E_F) + N_{\downarrow}(E_F)}$ where $N_{\uparrow}(E_F)$ and $N_{\downarrow}(E_F)$ are the DOS in the bulk of ferromagnetic layer at the Fermi energy. From this simple model, we can readily find that as the spin polarization is increased in the ferromagnetic layer, an enhanced TMR can be expected. Hence, materials with good electrical conductivity and high spin polarization are always desired for spintronic applications. In reality, however, the physical mechanism governing the spin polarization of tunneling electrons is much more complex. It is the SP of tunneling electrons other than bulk material SP that governs the spin dependent transport behavior. Recent experimental findings show that the amplitude of the spin polarization, and even its sign, strongly depends on the barrier material and interface preparation state [Moodera *et al.*, 1999; Teresa *et al.*, 1999]. The tunneling electron spin polarization could be very different from its bulk spin polarization away from the interface. Tailoring and understanding the interface magnetic state at MTJ interface will thus shed light on the MTJ development and improvement.

Nowadays MTJs that are based on transition-metal ferromagnetic materials and Al_2O_3 (AlO) tunnel barriers can be fabricated with highly reproducible characteristics and TMR values up to 50% at room temperature [Tsymbal *et al.*, 2003]. Later on, much larger values of TMR observed in crystalline MTJs with MgO barriers further boosted interests in spin dependent tunneling research [Yuasa *et al.*, 2004; Parkin *et al.*, 2004]. MgO tunnel

barrier based MTJs are nowadays widely used in hard disk drives and magnetic random access memories.

Half-metallic oxides like $La_{0.7}Sr_{0.3}MnO_3$ (LSMO) have high spin polarization and very good chemical stability, which makes them promising candidates for MTJs integration. The spin-dependent tunneling process in MTJ will directly reflect the interface electronic/spin state between the insulating barrier and ferromagnetic electrode, which provides us a great tool to investigate the interface properties. In this section, we utilize this powerful structure to study the interface magnetism between STO/LSMO in both (100) and (110) orientations. Our STO tunnel barriers are epitaxially grown by PLD in either (100) or (110) orientation which always gives us very smooth and conformal interfaces between the insulating barrier and ferromagnetic electrodes.

In addition, we also successfully achieve high-quality Al_2O_3 (AlO)/LSMO and HfO_2 (HfO)/LSMO interfaces. Up to date, the synthesis of MTJ barriers are mainly focused on sputtering, MBE and PLD etc... Atomic layer deposition (ALD) is well-known for its ability to deposit smooth, stoichiometric and conformal ultra-thin oxides and is an ideal candidate to grow MTJ oxide tunnel barrier [Leskela *et al.*, 2002]. Although people tried to fabricate MTJ directly by ALD, however, it has never been reported with convincing device performance yet [Mantovan *et al.*, 2012]. To the best of our knowledge, it is the first time to successfully realize robust TMR in LSMO/AlO/Co or LSMO/HfO/Co magnetic tunnel junction devices with AlO (HfO) *ex-situ* grown by ALD in our case. Our data show a TMR ratio as high as 30% at 30 K at a 2 mV bias voltage and this TMR signal can persist up to 300 K, higher than that of STO(100) barrier based MTJs in the

same structure. Moreover, the resistance and area product of MTJs indicate AlO tunnel barrier is very uniform and pinhole free, which is critical for spintronic applications.

III-2 MTJ Fabrication

III-2-1 Film Preparation

We start from the LSMO/STO/LSMO MTJ structure. The trilayer system can be epitaxially grown by Pulsed Laser Deposition (PLD) onto $SrTiO_3$ (100) or (110) substrate with a typical size of 5mm×3mm×0.5mm. Commercially available STO substrates from Crystec is pre-etched and annealed in ozone as described in the previous section. With this modified substrate treatment, the RHEED intensity oscillations were readily obtained during LSMO growth, which indicates an excellent layer-by-layer growth mode [Figure III-3].

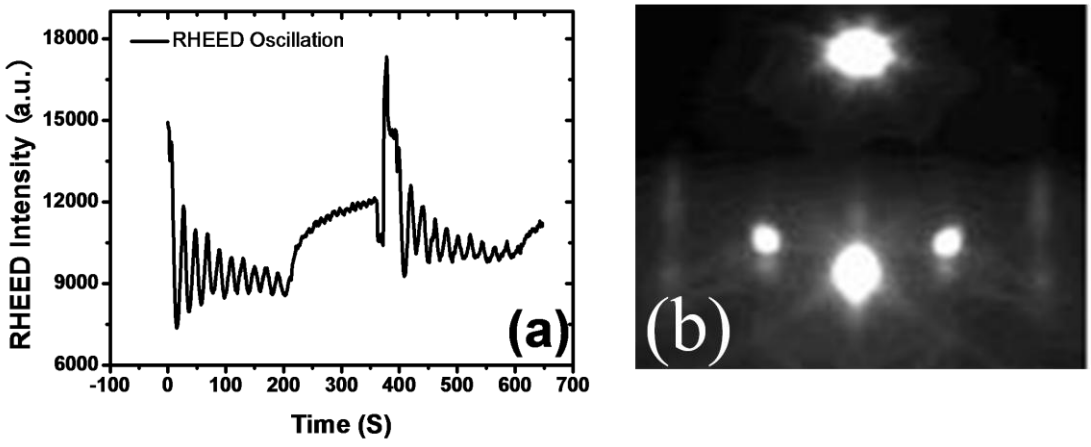

Figure III-3 (a) RHEED oscillation and (b) RHEED pattern for LSMO film during growth.

The growth temperature is kept at 800 ℃ and the oxygen pressure is 1 mTorr with 12 wt % of ozone. After LSMO growth, a STO film is epitaxially grown on top as tunnel barrier and the thickness of STO barrier varies from 6 ML to 10 ML. Following this, another layer of LSMO (~15-20 nm) is grown on top of STO. After growth the trilayer film is slowly cooled down to room temperature in ozone atmosphere and then immediately capped by a layer of 20 nm chromium deposited by a conventional E-beam Evaporator. This layer of Cr serves as a protection layer for the following processing steps. After this, we define Cr patterns with size from 5×5 μm^2 to 12×12 μm^2 by optical photolithography and Ar inductively coupled plasma (ICP) etching and these Cr patterns will serve as the ICP dry etching hard mask.

The Ar^+ ion milling technique is commonly used to define the magnetic tunnel junction areas for application. However, there are some critical consequences due to Ar^+ in our case. First of all, our Ar^+ milling process is done in an Oxford ICP etching system and there is a variation in etching rate even in the nominally same working condition. Secondly, Ar^+ introduces a serious implantation effect in the base LSMO electrode. Because the magnetism and conductivity of LSMO are very sensitive to doping, i.e. the charge state, this Ar^+ implantation effect always leads to a severely suppressed magnetism/conductivity of the base LSMO electrode. In experiment, we always observe a much lower T_c in the base LSMO electrode than its initial state before Ar^+ milling. This introduces an extrinsic effect if we want to study the intrinsic temperature dependent interface state. Figure III-4 shows an example of TMR vs. field from one MTJ device made by this Ar^+ milling technique. Even though we can obtain a relative decent TMR

signal as shown in Figure III-4, the bottom LSMO layer still has a suppressed T_c as confirmed by the resistivity vs. temperature measurement (not shown here).

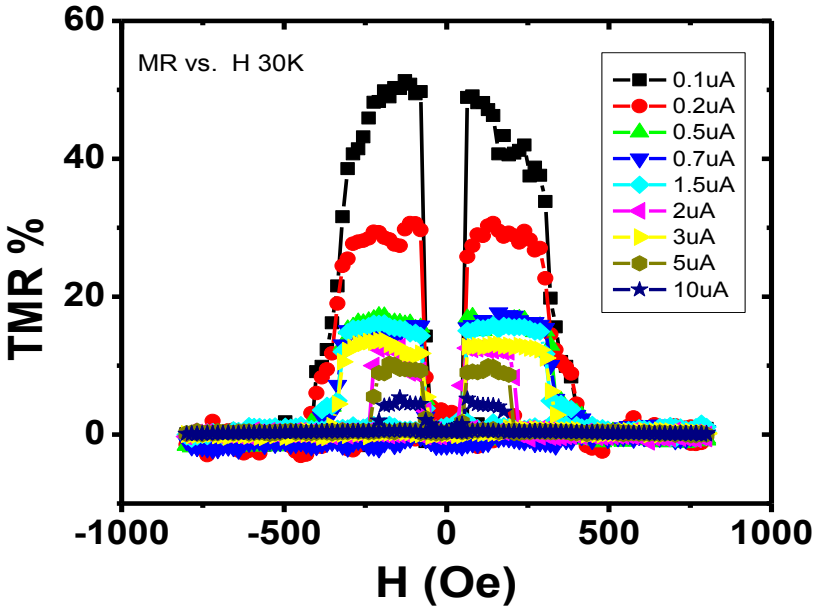

Figure III-4 TMR vs. H at 30 K for a LSMO/STO/LSMO-(100) device fabricated by Ar^+ milling technique. TMR persists up to 200 K only.

In order to avoid this detrimental side effect due to Ar^+ milling, we switch to LSMO/STO (AlO, HfO…)/Co structure fabricated by our specially designed shadow mask technique. In this way, we can avoid the Ar^+ milling process; this greatly enhances the device yield and performance. From our argument in the previous section, we learned that the interface between STO and base LSMO electrode in LSMO/STO(100)/LSMO is the interface that has severely suppressed magnetism. As long as we can preserve this interface in our study, we can make fair comparisons between different samples. In this sense the shadow mask technique works well for us. For LSMO/STO/Co structure, both

LSMO and STO layers are epitaxially grown by PLD as described in the previous section. For AlO or HfO barrier, we utilize the ALD technique to prepare them.

In the next step, the junction patterns are coated with 2000-Å SiO_2 grown by plasma enhanced chemical vapor deposition (PECVD). Following this, we use photo-lithography and reactive ion etching (RIE) to open the contact via right on top of tunnel junction areas. Finally, a metallization process completes the whole chip with a layer of Cr(10 nm)/Au(300 nm) deposited onto the top as contact electrodes. We have used the four-probe technique to measure the I-V curves and the junction tunneling resistance as a function of magnetic field using DC or AC technique. The magnetic properties of the pre-patterned trilayer film are measured in a Quantum Design SQUID system.

III-2-2 Atomic Layer Deposition Technique

Atomic layer deposition is a self-limiting process which involves a sequential surface chemistry reaction that takes place on the surface of a substrate. ALD is well known for its capability to deposit atomically thin and conformal films and thus very suitable for high quality tunnel barrier growth in MTJ devices [Leskela *et al.*, 2002]. In chemistry principle, ALD is similar to CVD technique but its reaction procedures involve two sequential steps [Cambridge NanoTech., Savannah100 Mannual]. The reaction chemicals in ALD are called precursors. We successfully grow high-quality AlO and HfO ultrathin tunnel barriers on LSMO epitaxial film. Here we take AlO barrier growth as an example to explain the procedures of ALD process.

For AlO growth, we use trimethylaluminium (TMA) and H_2O as precursors. The

growth temperature depends on the substrate material and growth rate requirement. In our case, the optimized growth temperature is 250 ℃. After we load a clean substrate with LSMO film into the ALD chamber, the growth of AlO thin film by ALD can be described by the following characteristic four steps: first, the first precursor which is H_2O vapor pulse in our case is pumped into the ALD chamber. This water vapor will react with LSMO and form hydroxyl on the top surface [Figure III-5 (a)]. The residual H_2O vapor will be pumped away. After a certain time interval, LSMO will be covered completely by hydroxyl and then a second precursor pulse which in our case is TMA is pumped into the ALD chamber. This second precursor will react with the pre-existing hydroxyl layer. During this reaction process, Al atoms in TMA molecule will substitute the hydrogen ions in the hydroxyls and form Al-O bonds, with CH_4 as a reaction product. This process will continue until all active hydroxyl are consumed by TMA molecules [Figure III-5 (b)]. All the residual TMA molecules are pumped away from the ALD chamber. After this step is completed, a water vapor pulse is pumped into the ALD chamber again. Because now the top surface on the substrate is not LSMO anymore, instead, it is a layer of $–CH_3$ groups from the previous TMA as shown in Figure III-5 (c). This TMA terminated surface will react with H_2O and form Al-O bond with CH_4 as the reaction product. Then TMA is pumped in to the ALD chamber again to react with the newly formed O-H terminated surface. From this we learn that for each precursor pulse, once active bonds created by the previous precursor are totally consumed, the reaction will automatically stop and all residual precursor molecules will be pumped away. Therefore it is a self-limiting growth process. Figure III-5 shows an example for a typical ALD process in which two cycles of

reaction is completed. One precondition is that the time interval between each precursor pulse needs to be optimized so that the reaction has enough time to complete itself. By tuning the growth parameters, we successfully achieve high-quality AlO thin film growth.

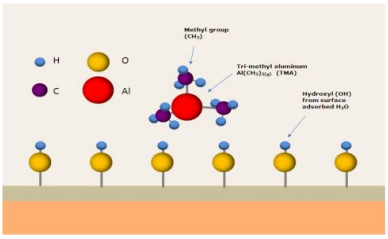

(a) Hydroxyl formation on the top surface

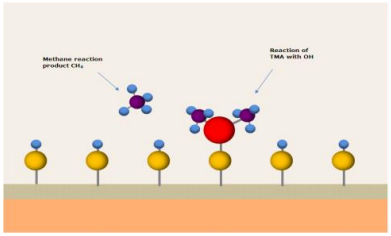

(b) Reaction between TMA and hydroxyl

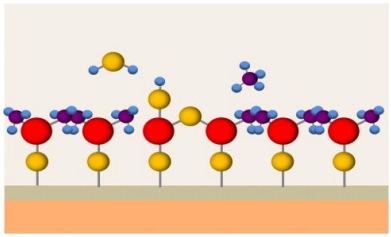

(c) Reaction between H2O and $–CH_3$ groups

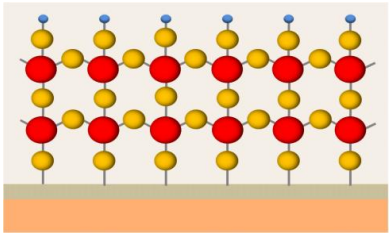

(d) Two cycles of reaction completed

Figure III-5 Example of two completed ALD cycles with H_2O and TMA precursors.

III-2-3 Shadow Mask Technique

The shadow mask will define our final MTJ devices. In our case, the typical pattern size ranges from $12 \times 12\ \mu m^2$ to $20 \times 200\ \mu m^2$. On such a small scale, it is not convenient to make the mask by conventional machining techniques. In order to do so, we use a thin Si substrate with thickness~200 μm as our shadow mask material. After carefully cleaning its surface in acetone bath, we deposit a layer of 100 nm Cr on top by electron beam deposition. Then we use photolithography and wet etching technique to selectively remove Cr to generate desired patterns. The areas free of Cr will be our final MTJ area locations. After this Cr selective removal, the whole Si wafer with Cr hard mask patterns on top is transferred into an Oxford ICP chamber. We use SF_6/C_4F_8 gases as etchant to deeply etch through Si at locations where Cr is selectively removed. In this way, we can define holes in a Si matrix with sizes ranging from $12 \times 12\ \mu m^2$ to $20 \times 200\ \mu m^2$.

We mount this shadow mask onto a XYZ stage and carefully align it with our LSMO/barrier bilayer film. In order to avoid the shadow effect during cobalt deposition, the first critical step is to make sure that the shadow mask contacts our sample surface intimately. Another important factor under concern is we need to place this XYZ stage with our sample/shadow mask together at a proper angle in the e-beam evaporator system so that cobalt beam can be evaporated perpendicular toward the surface plane and normal to the junction areas. By carefully doing so, we can always grow well-defined cobalt patterns onto the top of the tunnel barrier.

Figure III-6 shows the process of fabricating a Si shadow mask by a deep Si ICP etching technique.

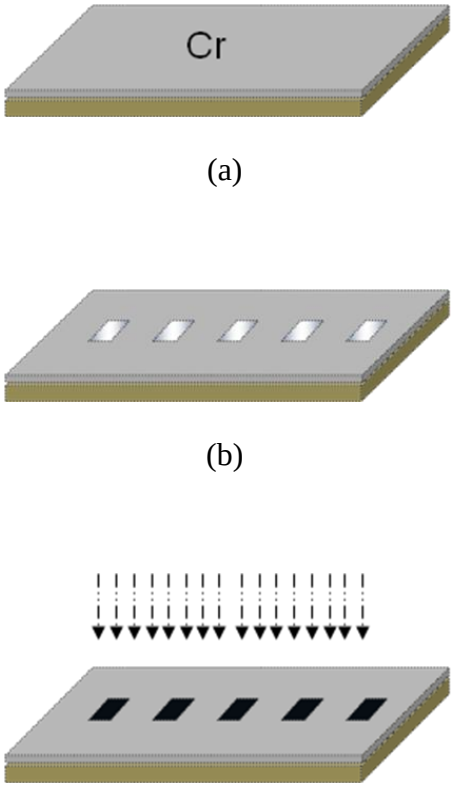

Figure III-6 Si shadow mask fabrication process by deep Si ICP etching (a) Cr coating on Si by e-beam evaporation (b) Cr pattern definition by photo lithography and wet etching and (c) Si deep ICP etching.

III-2-4 MTJ Fabrication Process

For MTJs with AlO or HfO barrier, we start from a LSMO film epitaxially grown by PLD. After we take LSMO out from the UHV chamber, we immediately expose LSMO film to ultraviolet light (UV) for 10 minutes. The purpose of this UV exposure is to make the LSMO surface wet to precursors especially water during AlO (HfO) growth in the ALD chamber. Following the UV treatment, LSMO film is transferred into the ALD

chamber with a background vacuum at 4.2×10^{-1} Torr. AlO films with thickness ranging from 1.2 to 2.1 nm were grown at 250 ℃ using alternating pulses of $Al(CH3)_3$ (TMA) and H_2O precursors (similar thickness range for HfO_2 barrier. Unless specifically pointing out, we always refer to AlO as our example). To ensure that the process is within a fully self-limited reaction process, the delay time between each precursor cycle is set at 45 s while the TMA and H_2O pulse durations are 15 ms each. The estimated deposition rate of roughly 0.08 nm per cycle is calibrated by AFM.

Before Co deposition, the LSMO film with Al_2O_3 barrier is post-oxidized by oxygen plasma in an EMS 1050 Plasma Asher at 100 W for 3.5 minutes (we will discuss this oxidation effect in details later). To avoid any interface contamination, 40 nm cobalt pattern is deposited through our shadow mask by an e-beam evaporator at an ambient pressure of 1×10^{-6} Torr. The size of cobalt pattern is either 25×80 μm^2 or 25×200 μm^2. In order to introduce a pinning effect to increase the coercive field of the Co film, the top surface of Co is oxidized by oxygen plasma to form a layer of antiferromagnetic CoO. Figure III-7 (b) shows an example of Co array right after e-beam evaporation. After that, the bottom LSMO electrode with a width of 250 μm is defined by standard photolithography and HF wet etching process. Following this LSMO base electrode definition, we use diluted HF (BOE) to selectively remove the STO (AlO or HfO) barrier at the two ends of the LSMO bottom electrode. Then we deposit a layer of Cr(10 nm)/Au(80 nm) for top contacts. 200 nm SiO_2 is grown on top by PECVD to passivate the sample and the top electrode via is selectively opened by photolithography and SiO_2 RIE. Finally top electrodes with Cr(10 nm)/Au(250 nm) are deposited by an e-beam

evaporator. Figure III-7 (a)-(f) demonstrates this MTJ fabrication process in detail.

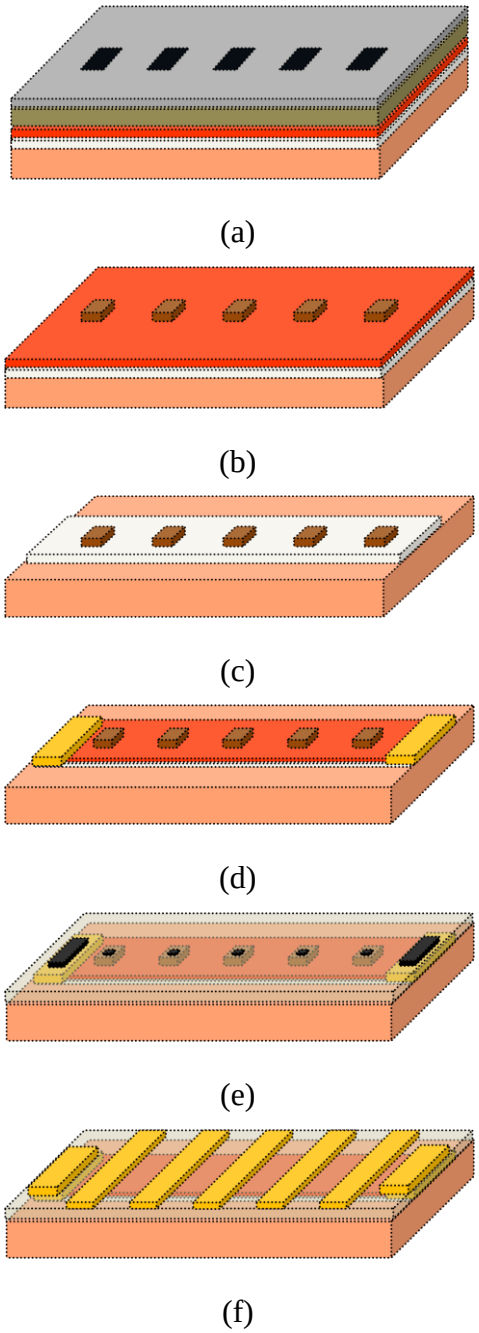

Figure III-7 MTJ shadow mask fabrication process: (a) Mask alignment (b) Co deposition (c) Bottom LSMO definition (d) Au and (e) SiO_2 deposition (f) Top electrodes deposition.

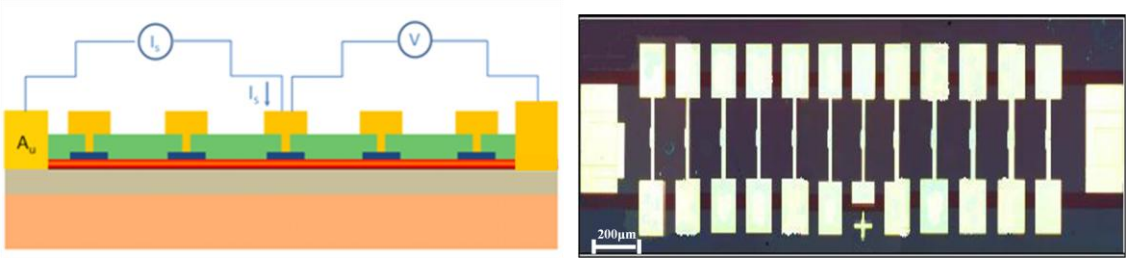

(a) (b)

Figure III-8 (a) MTJ measurement geometry (b) Optical image of completed MTJ arrays with top and bottom contacts. The active MTJ devices are located in the middle part of the vertical lines.

Figure III-8 (b) shows an optical image of a completed MTJ array with 11 devices in total sharing one common LSMO bottom electrode. Resistance of MTJ is measured either by a DC or AC method with the standard four probe geometry [Figure III-8 (a)]. Our TMR data shown here is taken at 40 K and at this temperature the bottom LSMO resistivity is about 600 μΩ·cm [Figure III-13], which has a sheet resistance much smaller than MTJ resistance and thus ruling out the possibility of current distribution effect [Van De Veerdonk *et al.*, 1997; Sun *et al.*, 1998].

III-3 Experimental Results and Discussion

A series of LSMO/AlO/Co MTJs are fabricated and we first study their magnetic field response of junction resistance at low temperature (40 K). Figure III-9 shows the magnetic field dependence of junction resistance measured at 40 K for three representative MTJs with AlO thickness of 1.2 nm, 1.6 nm and 2.1 nm, respectively. The

magnetic field is applied along the in-plane [001] direction which is the easy axis direction of the bottom LSMO electrode. All the AlO barriers of these three MTJs are treated by oxygen plasma for 3.5 minutes at 100 W before Co deposition. For MTJ with 1.2 nm AlO barrier, we can obtain only 8% TMR and no plateau appears in the TMR hysteresis loop except two sharp peaks in the anti-parallel state (blue solid triangles in the graph). This indicates the top cobalt and bottom LSMO electrodes cannot achieve a completely anti-parallel magnetization configuration; they are magnetically coupled together via pinholes of AlO barrier. As we increase the AlO thickness, however, the TMR ratio is significantly enhanced and the typical TMR plateaus start to appear in the TMR vs. H loop. For example, at 1.6 nm of AlO, we get a TMR ratio as high as 25% at a 5 mV bias (red open circles) and the typical resistance product (RA) is about 4.5×10^{8} $\Omega\cdot\mu m^2$.

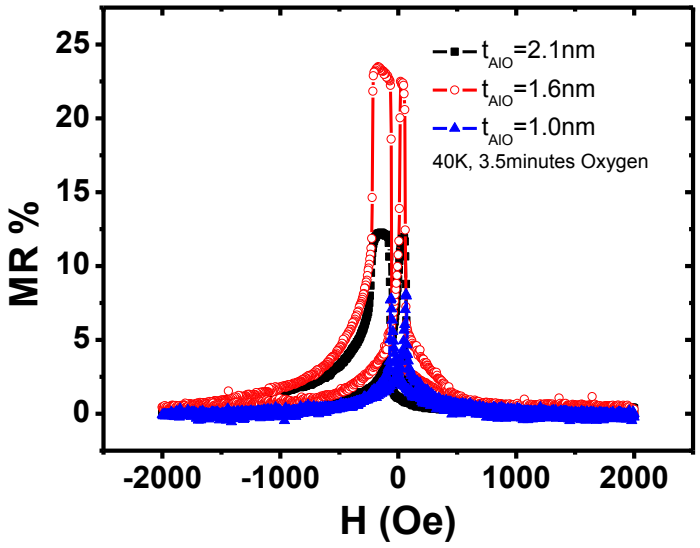

Figure III-9 MTJ TMR vs. H at 40 K for different AlO barrier thickness. Data shown here is for AlO thickness of 1.0 nm, 1.6 nm and 2.1 nm, respectively.

If we further increase the AlO barrier thickness the junction resistance greatly increases while the TMR ratio starts to decrease. The black solid square curve shows TMR ratio versus H behavior of a representative MTJ device with AlO barrier thickness at 2.1 nm and a much larger junction resistance 10^{10} $\Omega \cdot \mu m^2$. From our barrier thickness dependent TMR ratio study, we conclude that there is an optimal AlO barrier thickness around 1.6 nm that gives the highest TMR. Based on this experimental fact, our following study is then focused on MTJ devices with AlO barrier thickness at 1.6 nm which gives us the maximum TMR ratio. If we take the spin polarization (SP) of LSMO =95% as reported, then from the Julliere model, the corresponding Co SP is about 13.73% at the Co and AlO interface. Compared to Co bulk SP, this relative low SP of Co may be from interface contamination due to the *ex-situ* Co growth.

Oxygen deficiency in AlO barrier is a critical factor that affects the performance of MTJs. We systematically studied the post oxidation effect on AlO barrier by oxygen plasma. After AlO growth by ALD, we varied the oxidation time of the AlO barrier in oxygen plasma from an EMS 1050 Plasma Asher in the following cases: 0 minute, 2 minutes and 3.5 minutes with the same AlO barrier thickness (1.6 nm) and 100 W plasma power. Figure III-10 shows our main results at 5 mV bias and 40 K (Y-axis represents the resistance normalized to the resistance at 2000 Oe). With the same AlO barrier thickness, the device without post oxygen oxidation shows TMR at only 15% and more importantly, no clear TMR plateau appears. As we increase the oxygen oxidation dosage to 2 minutes, its TMR ratio starts to increase and the plateau starts to develop. At 3.5 minutes oxidation time, its TMR ratio reaches to the maximum of 25% and the device develops a well-

defined TMR plateau which demonstrates that the top cobalt and bottom LSMO achieve a completely anti-parallel magnetization configuration.

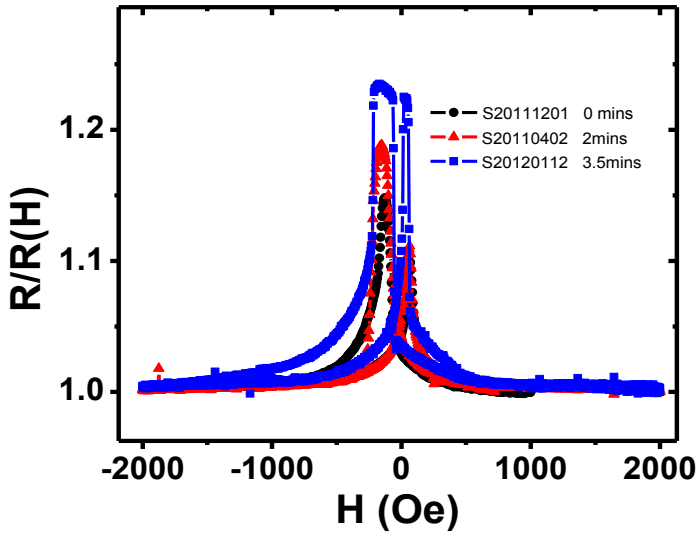

(a)

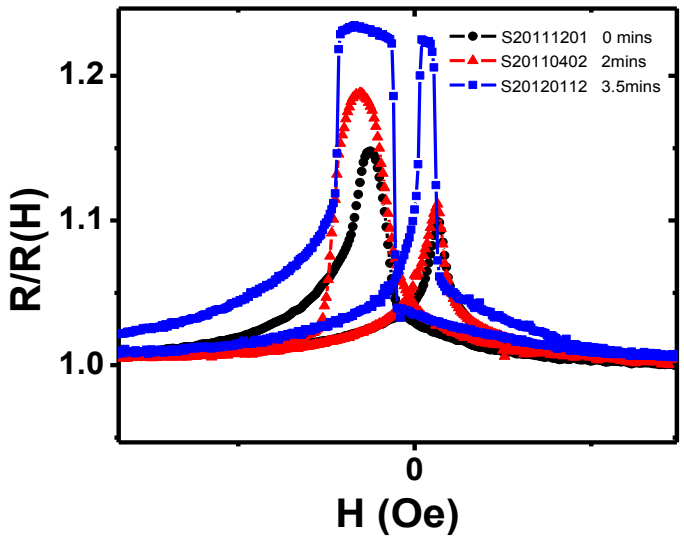

(b)

Figure III-10 (a) Oxygen oxidation dosage effect for TMR at 1.6nm AlO barrier thickness (b) Low field zoom in image.

These results from Figure-10 indicate that there could be pinholes in the as-grown AlO barrier where top and bottom magnetic layers are coupled to each other through these pinholes. Post oxygen oxidation can effectively remove these pinholes. One possible pinhole source may be due to the uncompensated $–CH_3$ groups during ALD growth, which will lead to the formation of pinholes. Oxygen ions can substitute these $–CH_3$ groups and make the AlO layer more condense and thus eliminating pinholes that are detrimental to TMR.

The temperature dependent TMR signal reflects how the interface spin state evolves as the bulk magnetism decreases. In order to study the temperature effect, we keep the bias voltage at 2 mV and vary temperature from 40 to 300 K to study its temperature dependence of TMR in the second device. To our surprise, even with this *ex-situ* grown AlO barrier, its TMR signal can persist up to 300 K, higher than that of the epitaxial STO(100) barrier based MTJ. This suggests that with this modified amorphous interface, we may effectively reduce the CT/OO effect since there is no preferential orbital for d-electrons in the AlO barrier. Figure III-11 shows representative TMR signal as a function of temperature for MTJs with two different barriers: (a) 1.6 nm thick amorphous AlO barrier; (b) 2.4 nm thick epitaxial STO barrier. From the figure, we can observe that TMR in LSMO/STO/Co starts to disappear at a relatively lower temperature compared with its AlO counterpart. Its bias voltage dependence behavior is shown in Figure III-12. As we can see from the figure, TMR ratio decreases rapidly as we increase the bias voltage. At 25 mV it decreases by about 50%. This fast decaying TMR ratio as a function of bias voltage may be due to a strong interface magnon scattering mechanism. This rapid

decreasing in TMR is repeatable in devices on different chips with the same AlO barrier thickness.

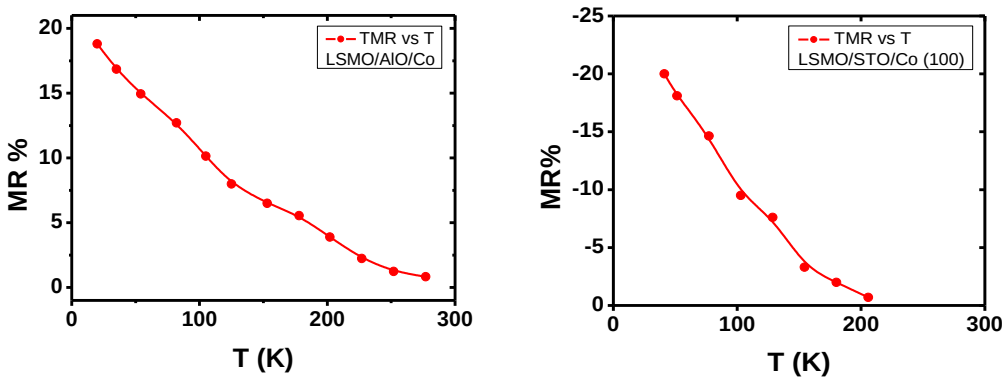

(a) (b)

Figure III-11 TMR signal as a function of temperature for two different barrier based MTJs. (a) is for AlO barrier at 1.6 nm while (b) is for STO barrier at 2.4 nm.

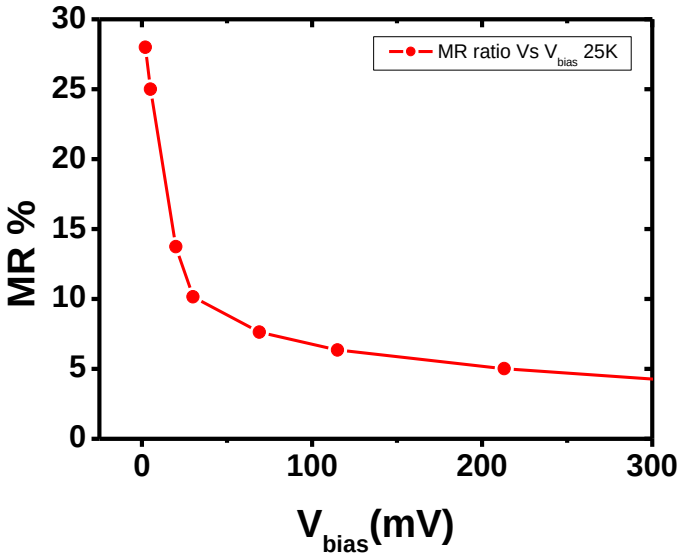

Figure III-12 Bias voltage dependence of TMR at 25 K for one LSMO/AlO/Co MTJ.

Figure III-13 shows temperature dependent electrical transport behavior of a typical MTJ device with AlO barrier at 1.6 nm. Solid green circles show junction resistance as a function of temperature and solid red squares are for temperature dependent TMR ratio. The open blue circles represent LSMO bottom electrode sheet resistance which is more than one order of magnitude smaller than the junction resistance. We notice the correlation between the junction resistance peak position and the temperature where TMR disappears. This interesting fact indicates a possibility that the junction resistance strongly depends on the interface electronic state and the interface SP through SO coupling.

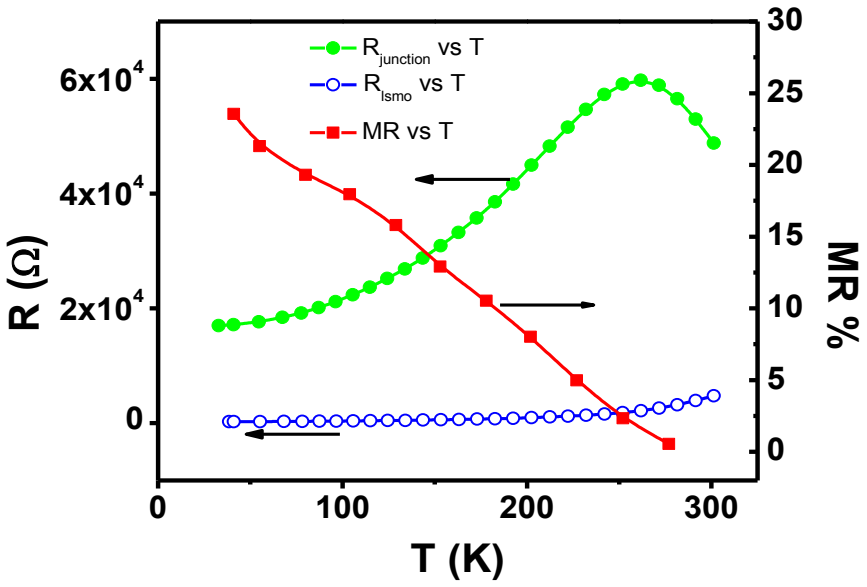

Figure III-13 Temperature dependence of one AlO barrier based MTJ device junction resistance (green), TMR ratio (red) and LSMO bottom electrode sheet resistance (blue).

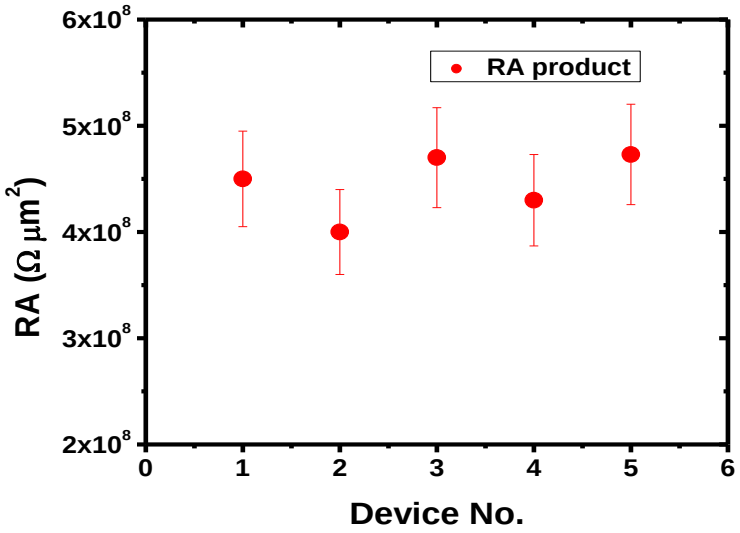

Figure III-14 RA product for 5 randomly selected devices on the same chip. Error bar represents a 10% tolerance. All the RA products are well within this 10% accuracy range.

In addition, good repeatability and uniformity are two critical features for practical applications. In order to qualify the AlO tunnel barrier grown by ALD, we randomly selected 5 devices from the 11 sharing the same LSMO bottom electrode as shown in Figure III-8 (b), and compared their RA product. The result is shown in Figure III-14. Red error bar corresponds to a 10% variation. This low RA variation indicates a very good barrier uniformity of AlO.

Beside AlO barrier, we also developed HfO tunnel barrier in LSMO/HfO/Co structure by ALD and studied its TMR behavior. In contrary to MTJ with AlO barrier which gives us a negative TMR (R(H) < R(0)), HfO barrier based LSMO/HfO/Co MTJ gives us an inverted TMR signal, that is R(H) > R(0). FigureIII-15 demonstrates one example for

HfO based MTJ device which has a HfO thickness of 1.7 nm. Data is taken at 40 K with -10 mV bias voltage.

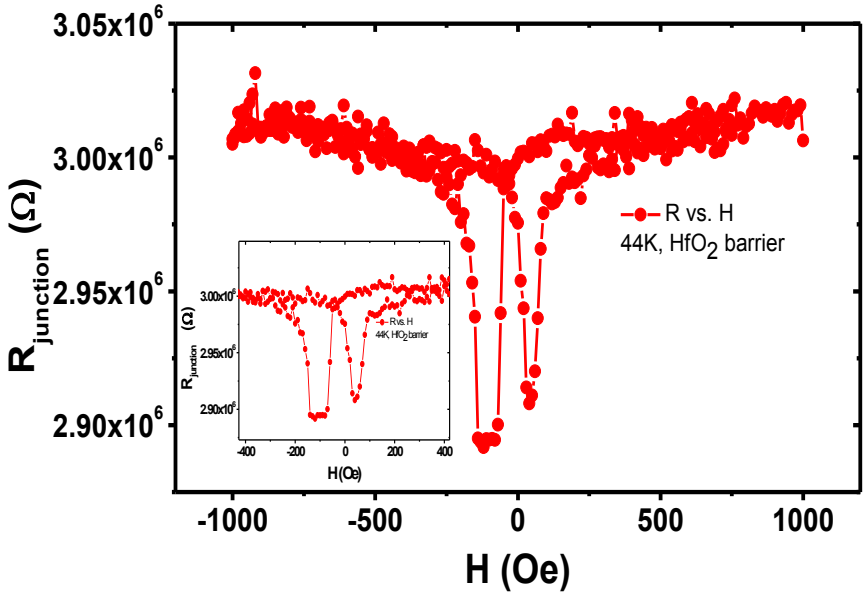

Figure III-15 MTJ R vs. H at 40 K for 1.7 nm HfO barrier thickness. Data shown here is for taken at 40 K with 10 mV bias voltage. Inset shows low field zoom in picture. MTJ size is 20×200 μm^2.

This inverted TMR can be understood by a d-electron bonding picture at the cobalt-oxide interface. Due to the strong s-d hybridization at the interface, we assume that the s component of the density-of-states (DOS) is suppressed within the d-band of cobalt and thus tunneling of the d-component in cobalt DOS governs the TMR. Cobalt has a negative spin polarization for 3d electron component and this leads to an inverted TMR. This model does explain the sign of TMR in a number of devices involving Co electrodes. [De Teresa *et al.*, 1999; Tsymbal el al., 2003]. Similar inverted TMR signal is also

observed in LSMO/STO/Co MTJ devices with LSMO and STO epitaxially grown both in (100) and (110) orientation. As shown in Figure III-16, (110) oriented MTJ does have a higher working temperature and higher TMR value than its (100) oriented counterparts with the same nominal STO barrier thickness.

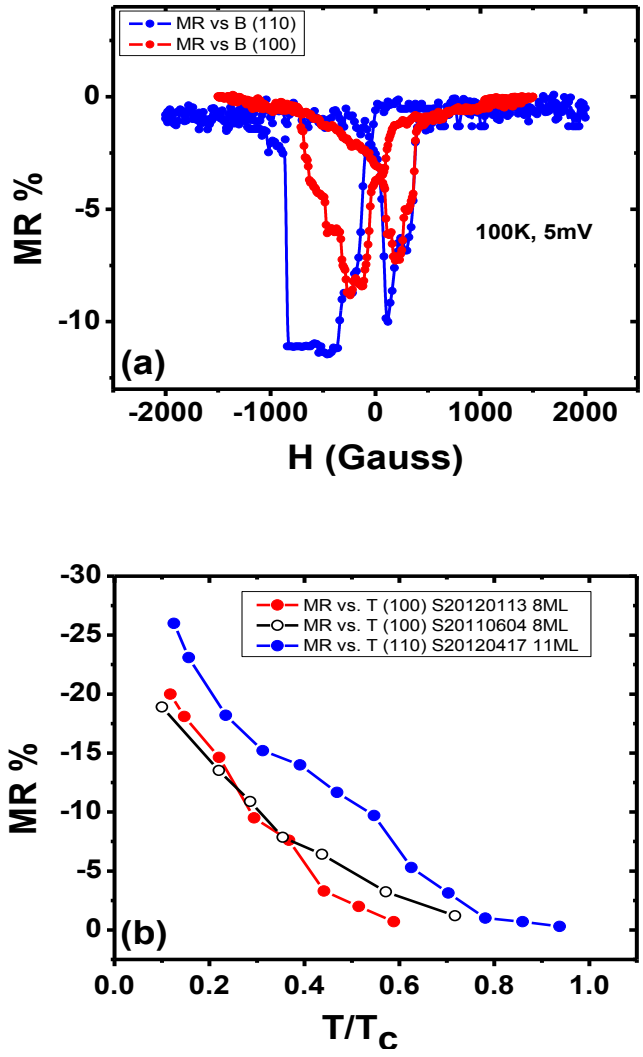

Figure III-16 (a) MTJ R vs. H with 3.1 nm STO barrier in (100) and (110) orientation, respectively. (b) TMR vs. T for both (100) and (110) oriented MTJs.

In summary, we successfully grew high-quality Al_2O_3 and HfO_2 tunnel barriers on LSMO with very good uniformity by ALD. The newly developed shadow mask technique enables us to engineer and study the interface issue between different oxide barriers and LSMO film. For oxide barrier grown by ALD, a systematic study on post oxygen oxidization shows that there are pinholes in the as-grown Al_2O_3 (HfO_2). Oxygen oxidization for the barrier can effectively eliminate pinholes and enhance the MTJ performance.

Al_2O_3 barrier produces a negative TMR while HfO_2 and STO in both (100) and (110) orientations give rise to an inverted TMR. These inverted TMR can be understood by the d-electron tunneling model. We also studied the temperature dependence of TMR magnitude as well as MTJ junction resistance. The consistence between TMR disappearing temperature and the junction resistance peak indicates a possibility that this temperature dependent behavior is dominated by interface metallicity and magnetism which calls for a more detailed study.

Reference

Tsymbal, E. Y. *et al.*, J. Phys.: Condens. Matter **15**, R109 (2003).

Julliere, M. Phys. Lett. **54A**, 225 (1975).

Moodera J. S. *et al.*, Ann. Rev. Mater. Sci. **29**, 381 (1999).

De Teresa, J. M. *et al.*, Phys. Rev. Lett. **82**, 4288; Science **286**, 507 (1999).

Parkin, S. S. P. *et al.*, J. Appl. Phys. **85**, 5828 (1999).

Yuasa, S. *et al.*, Nat. Mat. **3 (12)**, 868 (2004).

Parkin, S. S. P. *et al.*, Nat. Mat. **3 (12)**, 862 (2004).

Leskela, M. *et al.*, Thin Solid Films **409**, 138 (2002).

Mantovan, R. *et al.*, Thin Solid Films **520**, 4820 (2012).

Cambridge NanoTech. Savannah100 ALD system Mannual.

Van De Veerdonk, R. J. M. *et al.*, Appl. Phys. Lett. **71**, 2839 (1997).

Sun, J. J. *et al.*, J. Appl. Phys. **83**, 6694 (1998).

Chapter IV

Introduction to Graphene

IV-1 Discovery of Graphene

Carbon-based electronic materials have been extensively studied in several forms such as carbon nanotube (CNT), fulleren molecules, diamond and other organic materials. These materials are involved in many research areas such as field effect transistors (FET), spintronic devices, and single electron transistors and so on [Baughman *et al.*, 2002; Rueckes *et al.*, 2004; Xiong *et al.*, 2004]. Graphene, a single layer of carbon atoms packed in a honeycomb lattice structure is a rising star material since its first experimental realization in 2004 [Novoselov *et al.*, 2004]. However, at the beginning, graphene was only studied theoretically for its electrical [Wallace, 1947] properties as an imaginary material. The long standing opinion that hampers people to study it experimentally is that people believe at finite temperatures the lattice dislocations or defects will destabilize the crystal structure due to thermal fluctuation in 2D crystal [Peierls, 1935; Landau, 1937]. This long time hard ice was broken up only after two physicists, Geim and Novoselov from the University of Manchester successfully isolated the first graphene layer in 2004 [Novoselov *et al.*, 2004]. This newly discovered material then surges as the hottest research topic in condensed matter physics.

The mechanism accounting for the existence of a robust single layer 2D graphene is that the strong carbon-carbon bonds in graphene will prevent thermal fluctuations from

destroying the crystal structure so that a stable 2D carbon atom layer can survive. In addition, the crumpling in the third dimension, i. e. the ripple, could raise the elastic energy in graphene and thus suppress the thermal vibrations at finite temperatures [Geim, *et al.*, 2007]. In reality, there are some other 2D materials obtained in experiments, such as a single layer boron nitride, half-layer BSCCO [Novoselov *et al.*, 2005] or the recent realization of one atomic layer MoS_2 etc…[Radisavljevic *et al.*, 2011]. However, none of these materials attracts as much attention as graphene does due to its unique electronic band structure and exotic physical properties associated to its peculiar band structure.

IV-2 Lattice and Electronic Band Structure of Graphene

Graphene is an allotrope of carbon and its crystal structure consists of one-atom-thick 2-dimensional sheet of sp2-bonded carbon atoms that are densely packed in a honeycomb crystal lattice. This honeycomb lattice itself does not belong to the Bravais lattice category. However, if we set two atoms into one unit cell, then graphene has a 2D hexagonal lattice structure as shown in Figure IV-1. In order to describe it quantitatively, we can choose $\vec{a}$ and $\vec{b}$ as the primitive unit vectors as shown in Figure IV-1:

$$\vec{a} = a_0(\frac{\sqrt{3}}{2} + \frac{3}{2}) \text{ and } \vec{b} = a_0(\frac{\sqrt{3}}{2} - \frac{3}{2}) \qquad (1)$$

where a_0 is the distance between two adjacent carbon atoms in the graphene sheet. As to the reciprocal lattice, for this 2D system, we can set a third vector as $\vec{c} = 1\hat{z}$ in $\hat{z}$ direction. Then we can get its reciprocal lattice by the following procedure:

$$\vec{a}^{*} = 2\pi \frac{\vec{b} \times \vec{c}}{\vec{a} \cdot (\vec{b} \times \vec{c})} = \frac{2\pi}{a_{\circ}} (\frac{\sqrt{3}}{3} + \frac{1}{3}) \text{ and } \vec{b}^{*} = 2\pi \frac{\vec{c} \times \vec{a}}{\vec{a} \cdot (\vec{b} \times \vec{c})} = \frac{2\pi}{a_{\circ}} (-\frac{\sqrt{3}}{3} + \frac{1}{3}) \qquad (2)$$

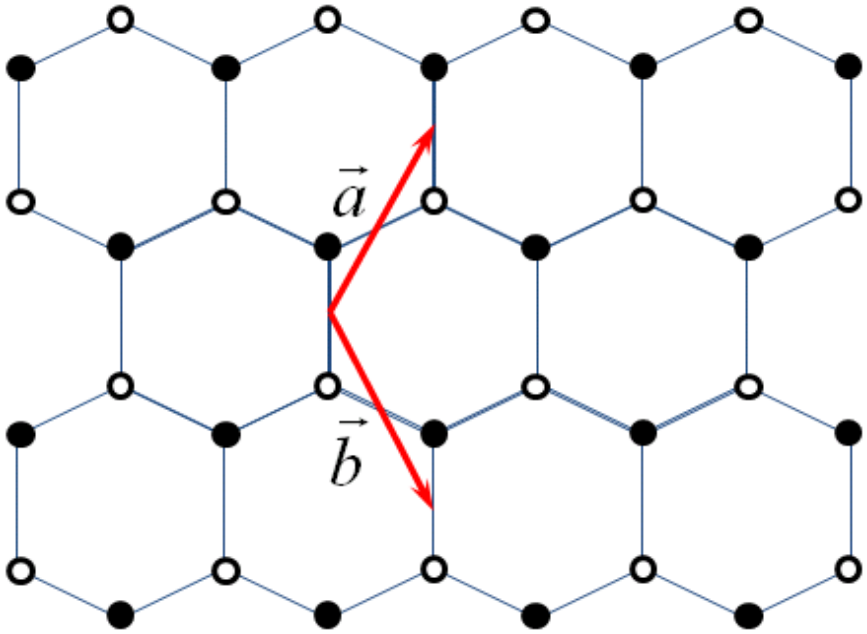

● Carbon atom at A site

○ Carbon atom at B site

Figure IV-1 Graphene lattice structure in real space.

Its Brillouin zone is also a 2D hexagon with six corners and they also belong to two distinct sets. With each set, there are three identical corners. Therefore there are actually two distinct points in the first Brillouin zone. Figure IV-2 shows a schematic view of the first Brillouin zone of graphene.

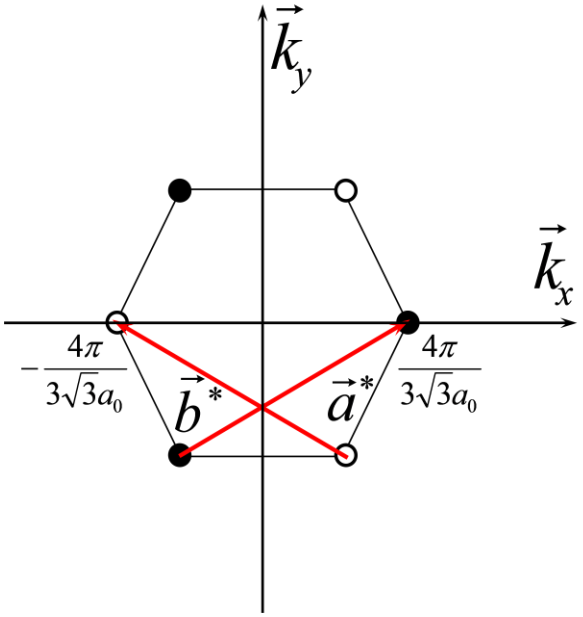

Figure IV-2 Schematic view of the first Brillouin zone in graphene in the reciprocal space.

In the single particle scheme, if we neglect the spin-orbital coupling in graphene, then the tight-binding Hamiltonian can be written as (within second quantized notation) [Shtengel, 2007]

$$H_{TB} = \mu \sum_i c_i^+ c_i - t \sum_{i \neq j} (c_i^+ c_j + c_j^+ c_i) \qquad (3)$$

Here, in the second term, the summation is performed over all nearest neighbors at sites i and j. *t* describes the "hopping" nature of electrons in graphene. Since it is a single particle Hamiltonian, we can easily rewrite it in the basis of Wannier states $\left|\vec{R}\right\rangle$:

$$H_{TB} = \mu \sum_R \left|\vec{R}\right\rangle\left\langle\vec{R}\right| - t \sum_R \sum_\delta \left|\vec{R}\right\rangle\left\langle\vec{R}+\delta\right| \qquad (4)$$

where δ are vectors connecting each carbon atom to its three nearest neighbors. From the honeycomb lattice structure of graphene, we know that each primitive unit cell contains 2 non-equivalent sites A and B (solid and open circles) and they belong to two distinct sublattices. It is natural for us to introduce two sets of Wannier functions $\left\langle r \middle| \vec{R}_A \right\rangle$ and $\left\langle r \middle| \vec{R}_B \right\rangle$ to describe electrons localized around the two distinct sites of each sublattice. From our previous statement, we can conveniently define

$$\left| \vec{R}_A \right\rangle \equiv \left\langle r \middle| \vec{R}_A \right\rangle \equiv \left| \vec{R} + \delta_A \right\rangle \equiv \left| \vec{R}, A \right\rangle \qquad (5)$$

$$\left| \vec{R}_B \right\rangle \equiv \left\langle r \middle| \vec{R}_B \right\rangle \equiv \left| \vec{R} + \delta_B \right\rangle \equiv \left| \vec{R}, B \right\rangle \qquad (6)$$

Here $\delta_A = a_0(0, \frac{1}{2}), \delta_B = a_0(0, -\frac{1}{2})$ are displacements of A and B atoms from the center of A and B atoms, respectively. With the definition of the Wannier states for each sublattice, the Hamiltonian becomes:

$$\begin{aligned} H_{TB} = \mu \sum_R \left\{ \left| \vec{R}, A \right\rangle \left\langle \vec{R}, A \right| + \left| \vec{R}, B \right\rangle \left\langle \vec{R}, B \right| \right\} - t \sum_R \left\{ \left| \vec{R}, A \right\rangle \left\langle \vec{R}, B \right| \right. \\ + \left| \vec{R}, A \right\rangle \left\langle \vec{R} + \vec{a}, B \right| + \left| \vec{R}, A \right\rangle \left\langle \vec{R} - \vec{b}, B \right| + \left| \vec{R}, B \right\rangle \left\langle \vec{R}, A \right| \\ \left. + \left| \vec{R} + \vec{a}, B \right\rangle \left\langle \vec{R}, A \right| + \left| \vec{R} - \vec{b}, B \right\rangle \left\langle \vec{R}, A \right| \right\} \end{aligned} \qquad (7)$$

After we make a Fourier transformation we find that

$$\left| \vec{R}, A \right\rangle = \frac{1}{\sqrt{N}} \sum_k e^{-i\vec{k}\cdot\vec{R}} \left| \vec{k}, A \right\rangle \quad (8) \text{ and inversely, } \left| \vec{k}, A \right\rangle = \frac{1}{\sqrt{N}} \sum_R e^{i\vec{k}\cdot\vec{R}} \left| \vec{R}, A \right\rangle \qquad (9)$$

We can do the same transformation for Wannier states at site B.

After plugging these transformation results into eq. 7, we obtain the new Hamiltonian as:

$$H_{TB} = \mu \sum_{R} \left\{ \left| \vec{k}, A \right\rangle \left\langle \vec{k}, A \right| + \left| \vec{k}, B \right\rangle \left\langle \vec{k}, B \right| \right\}$$
$$- t \sum_{k} \left\{ \left| \vec{k}, B \right\rangle \left\langle \vec{k}, A \right| (1 + e^{i\vec{k}\cdot\vec{a}} + e^{-i\vec{k}\cdot\vec{b}}) + \left| \vec{k}, A \right\rangle \left\langle \vec{k}, B \right| (1 + e^{-i\vec{k}\cdot\vec{a}} + e^{i\vec{k}\cdot\vec{b}}) \right\} \quad (10)$$

Up to now, we can identify that the Hamiltonian matrix is:

$$H_{TB} = \begin{pmatrix} \mu & -t(1 + e^{-i\vec{k}\cdot\vec{a}} + e^{i\vec{k}\cdot\vec{b}}) \\ -t(1 + e^{i\vec{k}\cdot\vec{a}} + e^{-i\vec{k}\cdot\vec{b}}) & \mu \end{pmatrix} \quad (11)$$

Solve the eigen function of this tight-binding Hamiltonian we obtain:

$H_{TB} \begin{pmatrix} \phi_1 \\ \phi_2 \end{pmatrix} = \varepsilon \begin{pmatrix} \phi_1 \\ \phi_2 \end{pmatrix}$ where $\Phi = \begin{pmatrix} \phi_1 \\ \phi_2 \end{pmatrix}$ is the wave function, the eigenvalues are:

$$\varepsilon_k = \mu \pm t \sqrt{3 + 4\cos(\frac{\sqrt{3}}{2} k_x a_o)\cos(\frac{3}{2} k_y a_o) + 2\cos(\sqrt{3} k_x a_o)} \quad (12)$$

If we set the reference vector $\vec{k} = k_x \hat{e}_x$, then along $\hat{e}_x$ direction, we obtain:

$$\varepsilon_{k_x} = \mu \pm t \sqrt{3 + 4\cos(\frac{\sqrt{3}}{2} k_x a_o) + 2\cos(\sqrt{3} k_x a_o)}$$
$$\varepsilon_{k_y} = \mu \pm t \sqrt{5 + 4\cos(\frac{3}{2} k_y a_o)} \quad (13)$$

From the dispersion relation as shown above, we immediately find that, while the gap remains positive in the $\hat{e}_y$ direction, it vanishes in the $\hat{e}_x$ direction at the corner of the

Brillouin zone, i.e. $k_x = \frac{4\pi}{3\sqrt{3}a_o}$. Since there are two distinct corners in the first Brillouin zone where the band gap vanishes linearly as k approaches to the corners—these corners are well known by a term "Dirac Points" and this is the main feature of graphene distinct from normal materials which leads to many exotic physical properties. Thermoelectric power, one of these physical properties will be discussed in detail in the following two chapters. Figure IV-3 is a 3D plot of graphene energy dispersion relation. The corners of the hexagonal Brillouin Zone correspond to six Dirac Points (K and K') [Wilson, 2006].

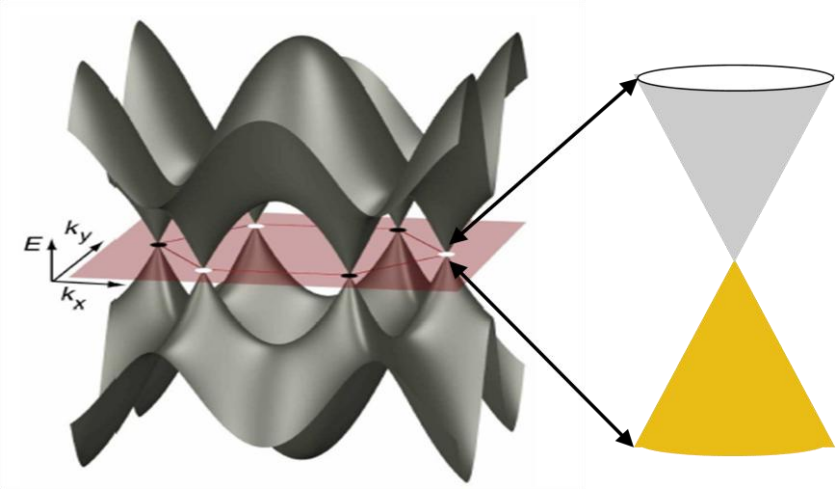

Figure IV-3 3D plot of graphene energy dispersion relation. The corners of the hexagonal Brillouin Zone correspond to six Dirac Points (K and K') [Wilson, 2006].

IV-3 Thermoelectric Power in Graphene

From the previous derivation, we already knew that the electron energy is linearly dependent on the quasi-momentum, and this can be well described by the massless

particle Dirac function near the Dirac Point except the light speed c is replaced by the Fermi velocity υ_F : $H\psi = \hbar\upsilon_F \sigma \cdot \vec{P}\psi$ (14) $\psi = \begin{pmatrix} \psi_A \\ \psi_B \end{pmatrix}$ (15)

One interesting prediction from this Dirac equation is that the carrier is massless, i.e. the carrier mass is zero. Experimentally, the cyclotron mass of graphene as a function of energy was measured by Novoselov *et al.* in 2004 [Novoselov *et al.*, 2005]. The following picture shows their results:

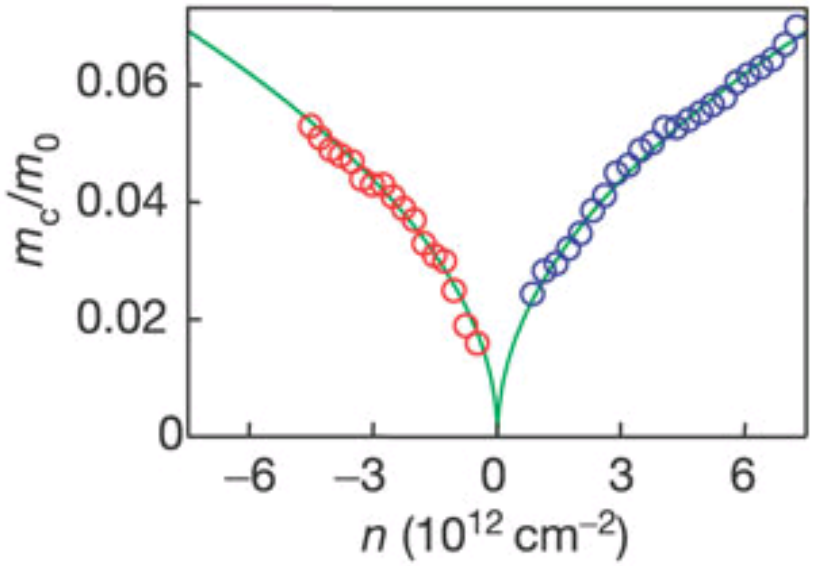

Figure IV-4 Cyclotron mass m_c of electrons and holes as a function of their concentration [Novoselov *et al.*, 2005].

Because the carrier mass is very small near Dirac point, we can expect very high carrier mobility in graphene under an external electrical field. Indeed, the latest experiments show hole mobility as high as 10^5 cm^2/Vs in suspended graphene [Du *et al.*,

2008; Bolotin *et al.*, 2008; Castro *et al.*, 2010]. This excellent electronic property of graphene making graphene a promising material for high-speed electronic devices has attracted the world's attention on both fundamental research and promising application appeal. On the other hand, however, the carrier mobility of graphene is not immune to the environment such as charge impurities scattering [Das Sarma, *et al.* 2011]. We develop a new method to improve graphene mobility: by removing the surrounding charged impurities we effectively obtain a clean graphene charge environment and high graphene carrier mobility. Based on this, we systematically studied the mobility dependent graphene thermoelectric properties.

In any conductor, one can always observe an electric field generated by a temperature gradient in the conductor. This electric field, which is induced by the carrier diffusion under the driving force of the temperature gradient, can be conventionally written as:

$$\vec{E}_{th} = \vec{S} \cdot \nabla \vec{T} \quad (16)$$

where $\vec{S}$ is called Seebeck coefficient or thermopower and $\nabla \vec{T}$ is the temperature gradient in the conductor.

So generally speaking, we can obtain both electrical and thermal current density for a transport process in a conductor as following:

$$\begin{aligned} J_e &= -\frac{L_{11}}{T} \nabla \vec{\mu} - \frac{L_{12}}{T^2} \nabla \vec{T} \\ J_Q &= -\frac{L_{21}}{T} \nabla \vec{\mu} - \frac{L_{22}}{T^2} \nabla \vec{T} \end{aligned} \quad (17)$$

Here μ is the sum of chemical and electrical potentials $\mu = \Delta\varepsilon + \Delta\upsilon$, L_{ij} are matrix

elements related to electrical conductivity, thermal conductivity and thermopower through the following equations [Shi, 1993]:

$$\begin{aligned} L_{11} &= \frac{\sigma T}{e^2} \\ L_{22} &= T^2(\kappa + T\sigma S^2) \\ L_{12} &= L_{21} = -\frac{ST^2\sigma}{|e|} \end{aligned} \qquad (18)$$

There are only 3 independent coefficients in a longitudinal transport problem. In the degenerate free-electron gas limit, we can obtain the thermopower by solving the Boltzmann equation and it can be described by the following equation:

$$\begin{aligned} S &= \frac{\pi^2 k_B^2 T}{3e}\left(\frac{\partial \ln \sigma(E)}{\partial E}\right)\Big|_{E_F} \\ \sigma(E) &= \frac{e^2}{4\pi^3\hbar^2}\iint_{fs}\left(\frac{\partial E}{\partial k_x}\right)^2 \frac{\tau(k)}{|\nabla_k E|}dS \end{aligned} \qquad (19)$$

This is called the Mott relation and S is often referred as diffusion thermopower. Since the thermopower is related to the energy derivative of the conductivity at the Fermi energy, the Mott relation provides us with a sensitive probe to detect its transport properties since we can conveniently tune both the carrier density and type in graphene (This carrier density tuning is essentially Fermi level tuning). Mobility affects its electrical properties directly in graphene; therefore, it is very natural to understand from the Mott relation that mobility will also play a significant role in thermopower of graphene. In our work, we have prepared graphene devices with relatively low carrier

mobility, and then tune their mobility within a certain range. As a starting point, we analyze our thermoelectric power (TEP) and electrical conductivity data. In high mobility state, we found that there is an excellent correlation between the energy derivative of TEP coefficients and electrical conductivity under high magnetic fields. Secondly, we deliberately vary mobility in the same graphene device and monitor the dependence of graphene Seebeck and Nernst coefficients on mobility. Our data shows that at high mobility state, TEP can effectively reveal the zeroth Landau Level sub-features up to 150 K and the central Nernst signal peak linearly depends on carrier mobility.

IV-4 Device Fabrication and Measurement Geometry

IV-4-1 Graphene Exfoliation

In this work, we studied thermoelectric properties of single layer graphene. All these single layer graphene flakes are exfoliated from either highly ordered pyrolytic graphite (HOPG from SPI) or Kish graphite (Covalent Materials USA Inc.). HOPG is well known for its high degree of three-dimension ordering and layered structure just like mica. It is easy to peel off as a multilayer piece. Kish graphite, on the other hand, has a relative smaller size and suitable for single layer graphene exfoliation. Figure IV-5 shows optical images of HOPG and Kish graphite, respectively.

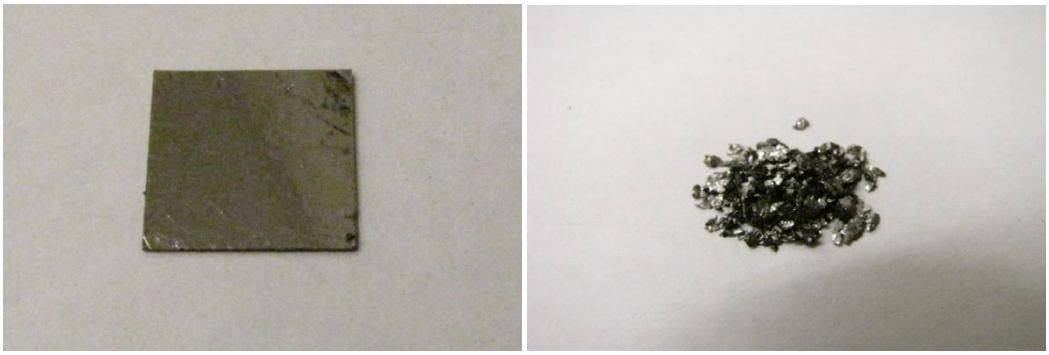

(a) (b)

Figure IV-5 Optical microscope image of HOPG (a) and Kish Graphite (b).

To produce thin graphene pieces, Novoselov and Geim invented a “Drawing approach” in 2004 and then the mechanical exfoliation method became popular. We use highly doped p-type silicon (0.5 mm in thickness) with 300 nm thermally oxidized SiO_2 layer on top as graphene supporting substrate. The SiO_2 insulating layer serves as a gating dielectric material while the highly doped Si serves as the backgate. Commercially available 6-inch wafers from University Wafer were cut into 5×5 mm^2 chips by a wire saw. Then the small pieces of Si wafer were carefully cleaned in an ultrasonic acetone bath, followed by 10 minutes immersion in H_2O_2 to remove possible organic contaminations and make the surface wet to graphene. After this the wafer is thoroughly rinsed by IPA and then DI water for 5 minutes, respectively. Finally, the wafer is blown dry by nitrogen gas. Typically wafers cleaned by these steps are ready for graphene exfoliation and has good adhesion to graphene flakes. For some devices, we anneal the substrate in Ar atmosphere with rapid thermal annealing (RTA) just before graphene

exfoliation to make sure that there is no water absorbate residual. Our experimental data shows that the annealing procedure does not produce any obvious difference.

To exfoliate graphene flakes onto the clean SiO_2/Si wafer, we first gently lay down a piece of scotch tape which is about 15 cm long and fix it onto a flat aluminum block surface with the adhesive side facing up. Then, we place HOPG or Kish graphite (for Kish graphite, we need to manually cleave the graphite piece first and then stick the flat surface to the tape) pieces onto the adhesive surface of the Scotch tape. Then we use a clean plastic tweezers to gently press the HOPG or Kish graphite toward the Scotch tape to make sure they stick to each other firmly. After this, we remove the HOPG or Kish pieces from the Scotch tape. There will be thin graphite flakes left on the scotch tape now. Secondly, we fold the scotch tape so that the tape will contact the other side of the graphite piece and then gently peel it off. Repeat this step 4-5 times and then place this tape with graphite side onto the SiO_2/Si surface. During this process, make sure that the tape is very flat on the wafer and then gently press it with a gum eraser. For a high graphene flake yield, we intentionally press this gum eraser for 1 minute and then release it. After gently remove the scotch tape from SiO_2/Si wafer, graphene flakes are left on the SiO_2 surface and subject to subsequent inspection. We use a Nikon Eclipse LV150 optical microscope to locate the single layer graphene pieces. Figure IV-6 shows our typical optical image of graphene flakes exfoliated by this mechanical method. Figure IV-6 (a) shows a large single layer graphene (SLG) piece from the Kish graphite while Figure IV-6 (b) shows graphene pieces from the HOPG where both SLG and few layer graphene are observed. From our optical inspection and statistics, we find that, under the same

preparation procedure, both HOPG and Kish Graphite give us a similar single layer graphene yield while the size of SLG from Kish is always larger than that from HOPG (Figure IV-6). There is some scotch tape residual left on SiO_2/Si substrate after exfoliation. The scotch tape residual can be removed by oxygen annealing at 300℃ for one hour. However, this annealing process can sometimes introduce unexpected charge doping effect and shift the Dirac point toward a higher value. So for our device shown here, we did not do this annealing process as long as our graphene flake is free of tape residual.

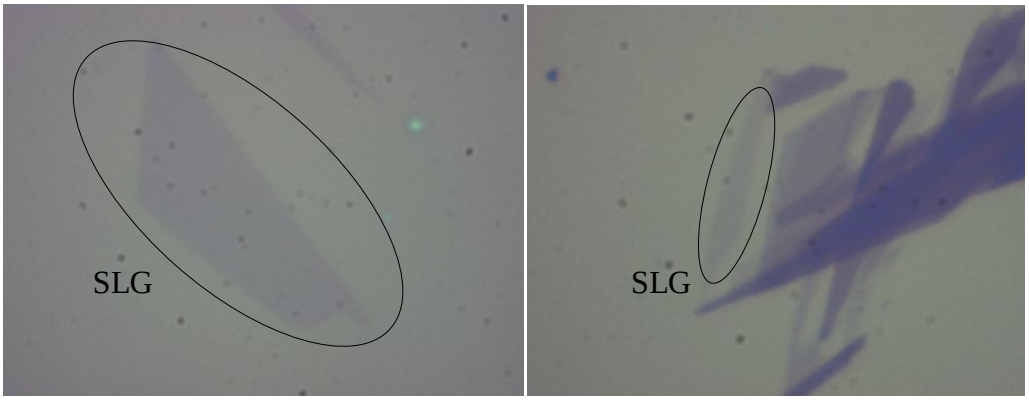

(a) (b)

Figure IV-6 Optical microscope image of single layer graphene flakes from Kish Graphite (a) and HOPG (b). Graphene flakes are enclosed in black ellipses.

IV-4-2 Electron Beam Lithography

After graphene flakes are exfoliated onto SiO_2 and located under the optical microscope, we use electron beam lithography (EBL) to pattern the graphene field effect transistor with a local heater and thermometers. First of all, a layer of methyl methacylate

(MMA) is spin-coated at 3200 rpm for 45 s and baked at 180℃ for 20 minutes. After we cool the chip down to room temperature in the air, another layer of poly methyl methacrylate (PMMA) is spin-coated at 3200 rpm for 45 s and baked at 180 ℃ for 20 minutes again. The purpose of MMA layer is to provide an undercut layer after pattern development so that this promotes the lift-off process. With these two properly baked MMA/PMMA resist layers, we transfer our sample into a LEO SUPRA 55 SEM/E-beam lithography system and perform the pattern writing. The electron accelerating voltage is set at 20 KV. Depending on the feature size we write, different electron beam parameters are properly adjusted. Table IV-1 shows our pattern feature sizes and corresponding electron beam exposure parameters.

Feature size	Beam aperture	Beam current	Exposure dosage
<5 μm	20 μm	75 pA	400 area dose
>5 μm	120 μm	2000 pA	430 area dose

Table IV-1 LEO EBL writing parameters for our Graphene FET devices.

After electron beam exposure, our samples are developed in the mixed solvent of Methyl isobutyl ketone (MIBK) and Isopropanol (IPA) (MIBK:IPA=1:3) for 65 s. Because the developing rate of MMA is much higher than that of PMMA (the actual developing rate depends on the concentrate weight of MMA and PMMA), we thus develope patterns with a undercut. This undercut is needed to facilitate the next lift-off

process. Ti/Au metal as contact electrodes are then deposited by electron beam evaporation after the pattern is well developed. Typically, for our graphene devices, the thickness of Ti is always 10 nm while the thickness of gold is either 50 nm for alignment mark or 80 nm for measurement electrodes. After metallization process, a final lift-off process is done in an acetone bath at room temperature followed by a thorough IPA/DI water rinsing. Because we have the undercut structure, the lift-off process is easily to be completed and no extra metal residual left on the graphene device after lift-off.

In order to generate a fine electrodes pattern on graphene at the desired position accurately, we have to align the electron beam with graphene sample before writing. Alignment mark is essential for this alignment procedure. We pre-define a large array (1.4 mm × 1.4 mm) of cross patterns with 60 μm spacing between every two crosses. We first write this cross array covering the location of graphene flake on SiO_2 substrate. Followed by Ti/Au evaporation and lift-off process, crosses alignment mark matrix is readily obtained. We first locate graphene flake with reference to a specific labeled cross and then align the electron beam to this labeled cross as a reference. After this, we can know the coordinates of our graphene flake relative to the origin of electron beam.

The typical size of our graphene is about 5 μm×15 μm. In order to make electrical connections, we need fine electrode contacts right on graphene and large bonding pads connected to those fine leads on graphene. Typically, those fine electrodes on graphene have a width ~1 μm and large bonding pads have a size of 100 μm×100 μm. For thermoelectric measurement purpose, we also need to fabricate a micro heater at one end of graphene and two four-termianl local thermometers. The local micro heater is sitting

about 2 μm away from graphene flake while the thermometers are located right on top of graphene. These two local thermometers also serve as thermal voltage monitors and electrodes to measure voltages for regular electrical transport measurements. There are 4 more electrodes sitting between the two thermometers. Figure IV-7 shows a completed fabrication process for a graphene FET device.

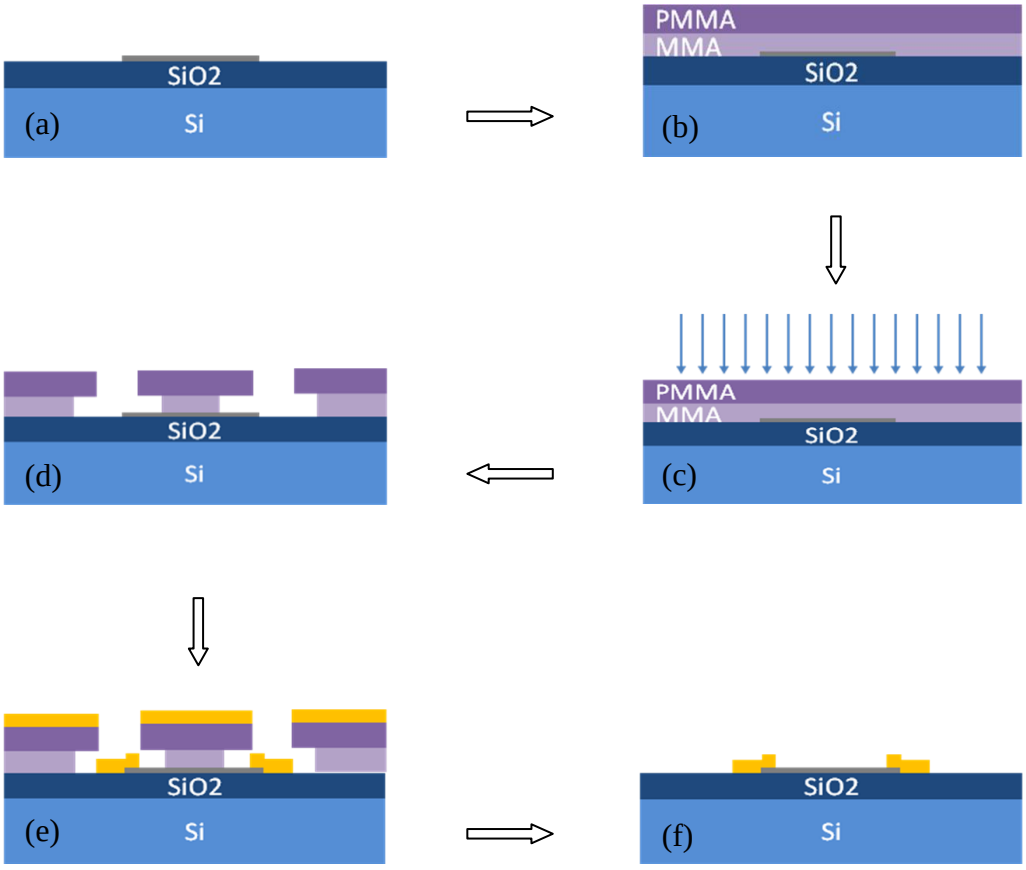

Figure IV-7 A typical process to fabricate a FET. (a) Graphene exfoliation (b) Spin coating of MMA and PMMA (c) E-beam patterning (d) E-beam pattern development (e) Metal electrodes deposition and (f) Lift-off.

IV-5 Experimental Details

As shown in the inset of Figure IV-8 (b), various Ti(10 nm)/Au(80 nm) leads are for measuring both longitudinal and transverse thermo-voltage (or Hall field) responses ΔV_x (1 & 6) and ΔV_y (2 & 4, and 3 & 5). Local temperatures and therefore the temperature difference ΔT along the longitudinal direction in response to heating power are detected by leads 1 and 6. A micro heater [red in Figure IV-8 (b)] is fabricated near one end of the graphene device to generate a temperature gradient when it is turned on. The typical heating power from this heater is 20-50 mW. The local temperatures are measured by the resistance thermometry (leads 1 and 6) which consists of two short segments of Ti/Au spanning across the graphene flake. Their four terminal resistances are recorded before and after the heater is turned on.

With the heater off, we measure the temperature dependence of the two thermometry resistance as our reference. The resistance change of these thermometers is converted to the local temperature change by comparing with the pre-measured resistance vs. temperature curve for Ti/Au. This resistance thermometry allows us to measure small temperature rises (~ 10 mK) for temperatures down to ~10 K. At each temperature, both the thermo-voltage responses and temperature changes between heater-on and heater-off are obtained. With these experimental measurements geometry, the Seebeck and Nernst coefficients can be determined by $S_{xx} = -\frac{\Delta V_x}{\Delta T}$ and $S_{xy} = -S_{yx} = \frac{\Delta V_y}{\Delta T}\frac{L}{W}$, respectively, with L being the separation between the thermometry contacts and W being the separation of the transverse voltage contacts. All the low-temperature magneto-transport and

magneto-thermoelectric transport measurements are carried in either Oxford He3 or PPMS system which covers the temperature range of 2 – 300 K and magnetic field up to 8 T (He3) or 14 T (PPMS) respectively.

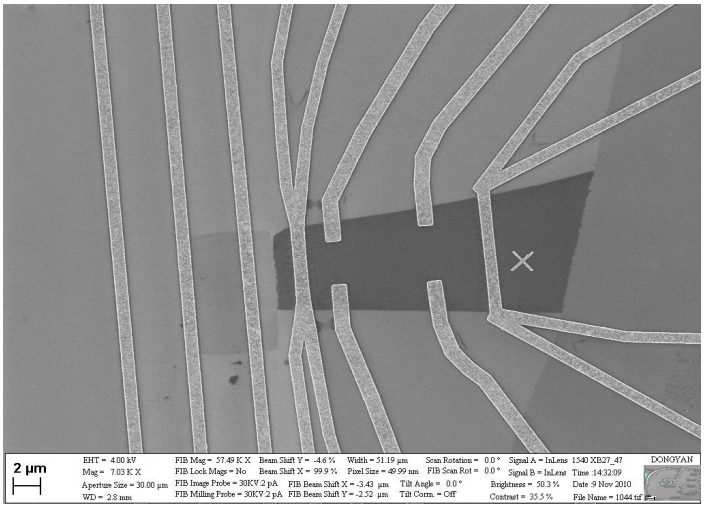

(a)

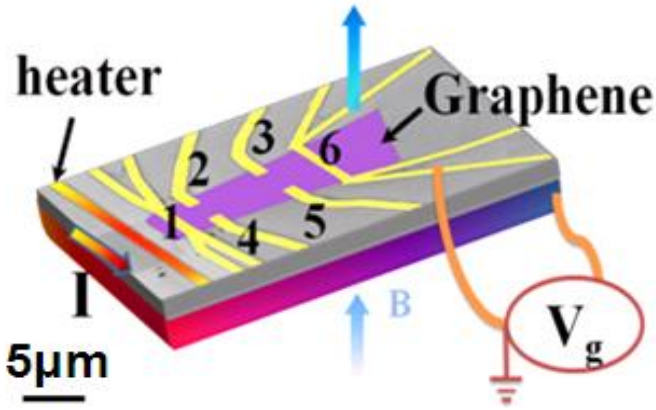

(b)

Figure IV-8 Schematic view of Graphene FET device with local thermometers and micro heater. (a) SEM image of one real device (b) False colored picture of a real device on SiO_2/Si.

IV-6 Graphene Mobility Tuning

In reality, the as-prepared graphene devices on SiO_2 do not always show high mobility larger than 10000 cm^2/Vs. The underlying mechanism that affects graphene carrier mobility has been a subject of extensive investigations ever since the inception of graphene devices [Novoselov, *et al.* 2004, Hwang, *et al.* 2007, Morozov, *et al.* 2008, Chen, *et al.* 2008]. It is believed that charge impurities on SiO_2 surface are one source of long range scattering which greatly suppresses graphene device mobility. People tried alternative approaches to improve graphene mobility. For example, by removing SiO_2 substrate, mobility as high as 2×10^5 cm^2/Vs has been obtained which suggests the importance of Coulomb scattering in graphene transport properties [Du, *et al.* 2008, Bolotin, *et al.* 2008]. Although such complicated device fabrication approach works well to improve graphene mobility, the mobility of finished devices is fixed and can vary from device to device. There is no convenient way to tune graphene mobility in a reversible way. However it is extremely important to have high mobility graphene device for application as well as fundamental research since a lot of exotic physical phenomena can be only revealed in high mobility states. Charged impurities from molecular adsorption, photoresist residues, and charges trapped on substrates during device fabrication are believed to be the main sources of long-range scattering which limits the carrier mobility [Schedin, *et al.*, 2008, Casiraghi, *et al.* 2007]; therefore, it seems logical to remove these scattering sources to achieve higher mobility state in graphene devices sitting on SiO_2 substrates. We recently developed a unique approach, namely, placing organic molecules and nanoparticles (NPs) adjacent to pristine graphene, to significantly enhance the

mobility [Wang *et al.*, 2010]. Using this approach, we do not only obtain higher mobility but also show a large degree of tunability in both carrier mobility and the charge neutral point position by controlling the charge environment of graphene on SiO_2 substrates. This provides us with the capability to systematically study TEP with different mobility state in the SAME graphene device.

The mobility in as-fabricated graphene devices by this way ranges from 1,500 to 5,500 cm^2/Vs at room temperature. To control the charge environment, we place 5-6 drops toluene solution of NPs such as iron oxide (mainly γ-Fe_2O_3 with a diameter of 13 nm) bound with ligand molecules on top of as-fabricated graphene with various concentrations. (The latest experimental results confirm that without NPs but toluene solution only can lead to the same mobility behavior of graphene, which indicates this mobility tuning capability is due to toluene). Since our experiments are done with toluene solution with NPs, we will present results with iron oxide NP solution treatment in this section as an example.

The blue curve in Figure IV-9 shows sheet resistance R_{xx} of a pristine state graphene device (i.e. without NPs, organic ligand molecules, or solvent) as a function of gate voltage V_g at 300 K. From Drude model the conductivity $\sigma = ne\mu$, where n is carrier density and μ is carrier mobility. The capacitance of our SiO_2/Si substrate is ~110 $af/\mu m^2$. So simply, we can deduce the carrier mobility by $\mu = \frac{1}{e}\frac{d\sigma}{dn} = \frac{1}{e}\frac{d\sigma}{(\frac{c}{e})dV_g} = \frac{1}{e}\frac{d\sigma}{dV_g}$.

The carrier mobility of the device shown in Figure IV-9 is ~4000 cm^2/Vs and the Dirac point is located at +16.5 V at room temperature. If we place 6 drops of iron oxide NP

solution and completely dry it, when we sweep gate voltage now, the behavior would be significantly different. The very first feature is that two resistance peaks in R versus V_g appear as shown in the following Figure IV-10.

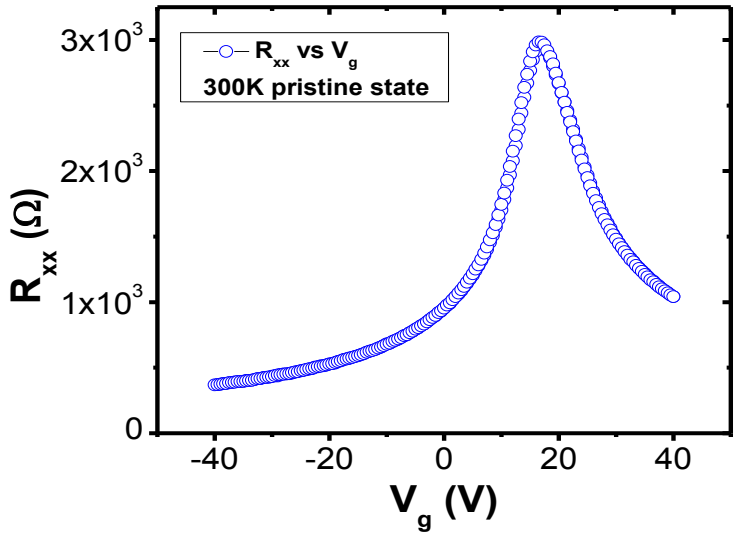

Figure IV-9 Sheet resistance vs. gate voltage of one graphene device at 300 K.

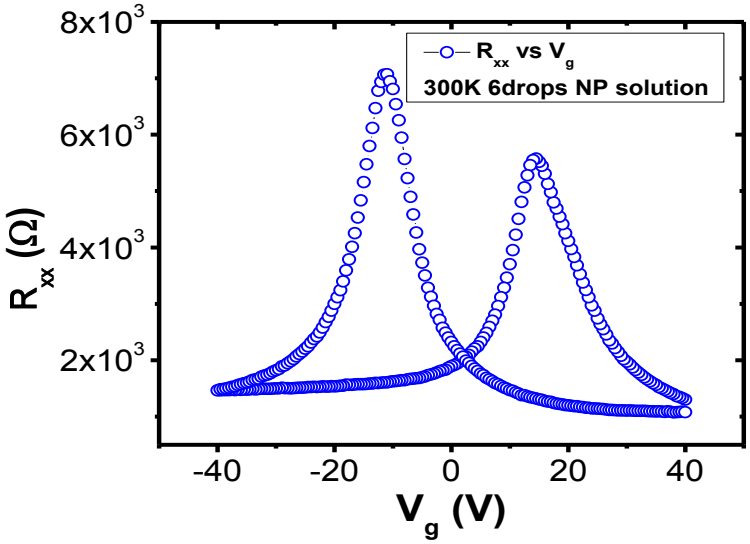

Figure IV-10 Sheet resistance vs. gate voltage with 6 drops NP solution on top.

We repeatedly sweep gate voltage with various starting and finishing V_g and with different gate voltage ranges so that we start and end with different carrier density in graphene. The R versus V_g hysteresis loop starts to appear if V_g exceeds a certain value in the previous sweep. We find that the peak position depends sensitively on the maximum voltage. This phenomenon suggests a bi-stable, i.e. two possible resistance states for a given V_g. In other words, the carrier density in graphene and thus the resistivity is not unique to V_g any more. We know that such bi-stability does not exist in pristine graphene device; therefore, the bi-stability must be caused by ligand-bound NP solution. Clearly, the external electric field alters the charge state in NP solution adsorbed on graphene which is not a unique function of the electric field, and in turn this will lead to the R versus V_g hysteresis in graphene. Because the adsorbed toluene molecules or NPs do not provide any parallel current path, all the conductivity must come from graphene itself.

From the R versus V_g loop, we immediately find another surprising consequence: the carrier mobility is greatly enhanced around the two peaks. After 6 drops of NPs containing solution are applied, the room temperature mobility increases to 8500 cm^2/Vs near the two resistance peak locations (nominal Dirac points). People argue that graphene mobility is very sensitive to organic molecules such as photoresist residues, which can trap charge impurities and consequently lead to additional scattering. Apparently, by applying NP toluene solution, we create a physically dirty environment on graphene. But we do not introduce adverse effect on the carrier mobility; on the contrary, we create a cleaner charge environment and this enhances the mobility by an entirely unexpected factor of ~200%.

At room temperature, to our surprise, with toluene solution absorbate on top, graphene device resistance always undergoes a time dependent relaxation process. Upon the application of a fixed V_g, the graphene resistance will continuously increase as a function of time. Figure IV-11 shows a good example how the resistance evolves as a function of time as we set gate voltage at a certain value at 295 K [Wang *et al.*, 2010].

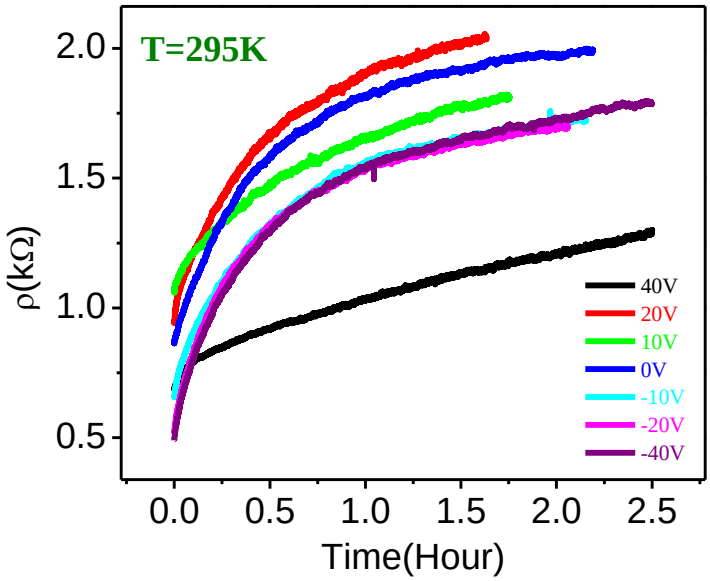

Figure IV-11 Time dependent graphene resistance at different set gate voltages at 295K [Wang *et al.*, 2010].

It is worth mentioning that no matter what value the gate voltage is set (in the same sense, graphene initial state could be either in hole or electron side at any concentration) the graphene resistance always climbs up or in other words, moves towards the charge neutral point value as a function of time. This phenomenon suggests that the graphene

device does not prefer to carry extra electrons or holes once there is a layer of toluene absorbate. The presence of molecules nearby provides a charge reservoir that accepts and stores the extra charges in graphene. The characteristic time for the relaxation process is about 2,000 s for this device at room temperature, which is much slower than gate sweeping rate; therefore, we can ignore this time-dependent process during normal gate sweeping. More interestingly this hysteretic behavior can be frozen at temperature below 250 K, i.e. there is no hysteresis any more at low temperature and its final charge state depends on the charge state before frozen. One consequence of this interesting phenomenon is that the carrier mobility in graphene is tunable, i.e. we can achieve different mobility state in the same device by freezing its different room temperature charge state. For example, if we first set V_g at an arbitrary value at room temperature and wait for a certain time, and then we quickly cool the device to low temperatures at the same V_g, At temperature below 250 K, the double peaks and associated R versus V_g hysteresis disappear, in the meantime, the time dependence in resistance is no longer present either. These two facts reveal that the initial room temperature charge state right before cooling in NPs is frozen, and a varying V_g only modulates the carrier density in graphene at low temperature, just as in regular pristine graphene. It occurs maybe because the links between graphene and toluene molecule become very resistive at low temperatures as observed in many other molecular systems.

Depending on the resistivity value in the pre-cooled state which can be set by controlling the waiting time at room temperature, the resulting low-temperature mobility can vary literally anywhere within a certain range. Figure IV-12 shows sheet resistance vs.

V_g behavior of one device at 150 K.

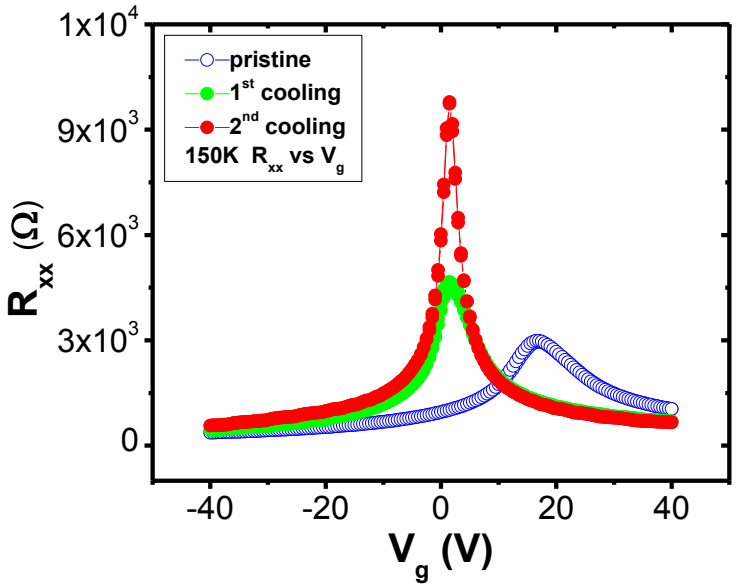

Figure IV-12 Sheet resistance as a function of gate voltage V_g for device A to be discussed in Chapter V and VI.

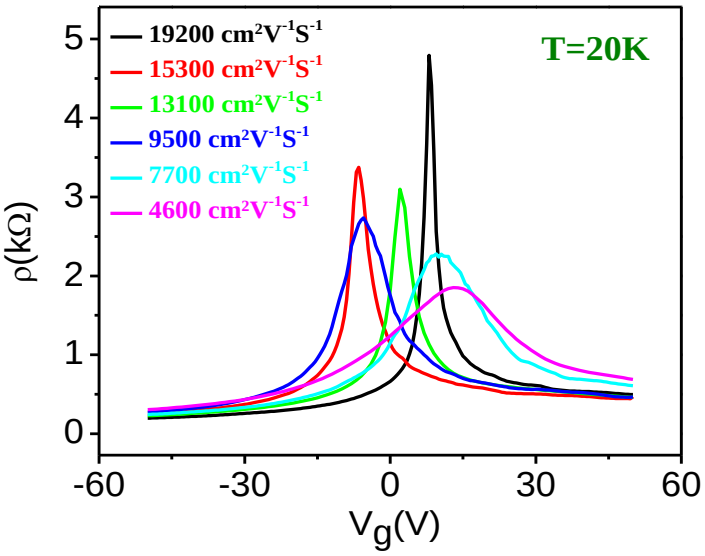

Figure IV-13 Different mobility states in the same device after tuning [Wang *et al.*, 2010].

From Figure IV-12, we find that the Dirac point in the pristine state is about +16.5 V while it is about 1V in the NP solution treated state. In addition, the mobility increases from 4250 to 12900 cm^2/Vs, a factor of 3! In our case, because the cooling rate is low in He3 system, it is relatively hard to get too many mobility states at low temperature. If we cool the device down very fast at different charge state at room temperature, more low temperature mobility states can be achieved by fast freezing its charge state.

In the example from Wang's result as shown in Figure IV-13, the tuned lower limit is even lower than that in the pristine state which is 5500 cm^2/Vs. The key to tuning the carrier mobility is the pre-cooled charge state which can be accurately monitored and set by the time-dependent resistivity. The closer the graphene is to the charge neutral state (i.e. resistivity maximum) before frozen, the greater the low-temperature mobility becomes. By this way, we can not only widely tune the carrier mobility but also the position of Dirac point. If we set gate voltage at a certain value and wait for a long time so that the resistivity of graphene can climb up to or very close to the charge neutral point, then if we quickly cool the device down to low temperature, its Dirac point will be close to that gate voltage. High mobility in all cases is obtained by setting the device at an arbitrary gate voltage at high temperature and then cooling down after its resistivity climbs close to the maximum. This fact suggests that almost all mobile charges initially residing in graphene are transferred to toluene molecules or NPs, which in turn produce an electric field on graphene.

Reference

Baughman, R. H. *et al.*, Science **297**, 787 (2002).

Rueckes, T. *et al.*, "Nanotube Films and Articles", US 6,706,402, (2004).

Xiong, Z. H. *et al.*, Nature **427**, 821(2004).

Novoselov K. S. *et al.*, Science **306**, 666 (2004).

Wallace, P. R., Phys. Rev. **71**, 622 (1947).

Nemanich, R. J. *et al.*, Phys. Rev. B **20**, 392 (1979).

Peierls, R. E., Ann. I. H. Poincare **5**, 177 (1935).

Landau, L. D., Phys. Z. Sowjetunion **11**, 26 (1937).

Geim, A. K. *et al.*, Nature Materials **6**, 183 (2007).

Novoselov, K. S. *et al.*, Proc. Natl. Acad. Sci. **102**, 10451 (2005).

Radisavljevic, B. *et al.*, Nature Nanotechnology **6**, 147 (2011).

Shtengel, K., Physics 240A at UC Riverside, Homework Solution.

Wilson, M., Physics Today **59**, 21 (2006).

Novoselov, K. S. *et al.*, Nature **438**, 197 (2005).

Du, X. *et al.*, Nature Nano. **3**, 491 (2008).

Bolotin, K. I. *et al.*, Phys. Rev. Lett. **101**, 096802 (2008).

Castro, E. V. *et al.*, Phys. Rev. Lett. **105**, 266601 (2010).

Das Sarma, S. *et al.*, Rev. Mod. Phys. **83**, 407 (2011).

Shi, J. PhD Thesis, (1993).

Schedin, F. *et al.*, Nature Mater. **6**, 652 (2007).

Casiraghi, C. *et al.*, Appl. Phys. Lett. **91**, 233108 (2007).

Wang, D. Q. *et al.*, Nano Lett. **10**, 4989 (2010).

Chapter V

Mobility Dependence of Graphene Thermopower

V-1 Introduction

Carrier transport properties of graphene have attracted much recent research interest, both for its electrical and thermal transport. Transport properties of graphene are not only determined by its unique band structure, but also strongly influenced by the impurity scattering and various interaction effects. Within the diffusive transport regime, graphene shows excellent carrier mobility comparable to or better than that of the conventional semiconductors like Si or Ge, which has been a subject of extensive theoretical and experimental studies. For example, a wide range of carrier mobility, from 1000 to 60000 cm^2/Vs, has been demonstrated in exfoliated graphene devices on SiO_2 and h-BN substrates [Tan *et al.*, 2007; Dean *et al.*, 2010]. However, as we discussed in the previous section, substrate-supported graphene devices are always susceptible to interfacial phonon scattering and a varying degree of charged impurity scattering from disorders on the substrates [Chen *et al.*, 2008; Adam *et al.*, 2008]. In suspended graphene devices, mobility as high as 200,000 cm^2/Vs was realized by removing those scatterings mechanisms [Bolotin *et al.*, 2008; Du *et al.*, 2008].

Disorders will not only affect the electrical transport properties such as carrier mobility, but also play an important role in the thermoelectric and magneto-thermoelectric transport properties. Conversely, the thermoelectric transport can serve as

a unique tool to probe various effects on diffusive transport. The disorder effect on magneto-thermoelectric transport has been studied in both theories [Ugarte *et al.* 2011; Gusynin *et al.*, 2006; Zhu *et al.*, 2010] and experiments [Zuev *et al.*, 2009; Wei *et al.*, 2009; Checkelsky *et al.*, 2009; Wang *et al.*, 2011; Liu *et al.*, 2012]. For example, the dependence of S_{xx} and S_{xy} on carrier mobility was theoretically predicted for various regimes of classical transport. In quantizing magnetic fields, a universal scaling for both electrical and thermoelectric transport coefficients was found for various disorder strengths [Zhu *et al.*, 2010]. However, even the experimental results for high Landau levels (LLs) are in agreement with theories prediction, there is still a discrepancy on the trend of the Seebeck coefficient near the zeroth LL [Zhu *et al.*, 2010]. In most experiments, because the as-fabricated substrate supported graphene devices always have random and fixed mobility values so that the direct relationship between the transport coefficients and mobility thus the disorders could not be easily established experimentally. In the previous section, we have shown that the low-temperature mobility of graphene can be reversibly tuned via controlling the high-temperature resistance level using ligand-bound Fe_2O_3 nanoparticles plus toluene molecules in the same device [Wang *et al.*, 2010]. This reversible mobility tuning capability provides us an unprecedented opportunity to systematically study how the charge impurity and charged disorders would affect transport properties in the same graphene devices. The purpose of this section is to establish the dependence of the magneto-thermoelectric transport properties of single-layer graphene on the carrier mobility which reflects the disorder status with this new capability.

All experimental results shown here are from two representative graphene devices (A and B). Data from other devices show qualitatively the same behavior. We use Fe_2O_3 NP toluene solution to tune the carrier mobility of the two devices. In order to obtain different mobility states, we need to fast cool down graphene devices in different charging states at room temperature. However, because both He3 and PPMS cannot achieve a fast cooling process, the tuning capability is limited and we cannot achieve as many mobility states as in fast cooling procedure. For device A we obtain three distinct mobility states at temperatures below 250 K by this relatively low cooling rate tuning while for device B we get four distinct mobility states.

V-2 Effect of Mobility on Zero-field Electrical and Thermoelectric Transport

In order to qualify our graphene device, we start with high-temperature measurement without any external magnetic field first. Figure V-1 (a) shows sheet resistance R_{xx} vs V_g behavior of one device at 150 K (the same one as Figure IV-12). The Dirac point in the pristine state of this device is about +16.5 V while it is about 1 V in the NP solution treated state. In addition, the mobility increases from 4560 to 12900 cm^2/Vs, a factor of 3. Figure V-1 (b) shows the electrical conductance σ vs. relative gate voltage ΔV_g for three distinct mobility states in device A. The corresponding mobility in these three states are 4560, 8500 and 12900 cm^2/Vs respectively. Similarly, the mobility of device B is tuned into 4 different states: 7000, 9330, 15330, and 17000 cm^2/Vs. Clearly, from Figure V-1 (b)

we learn that the low-mobility state has a broader minimum conductivity plateau, which is consistent with earlier experimental observations. The shrunk minimum conductivity plateau suggested a suppressed charged impurity scattering [Tan *et al.*, 2007].

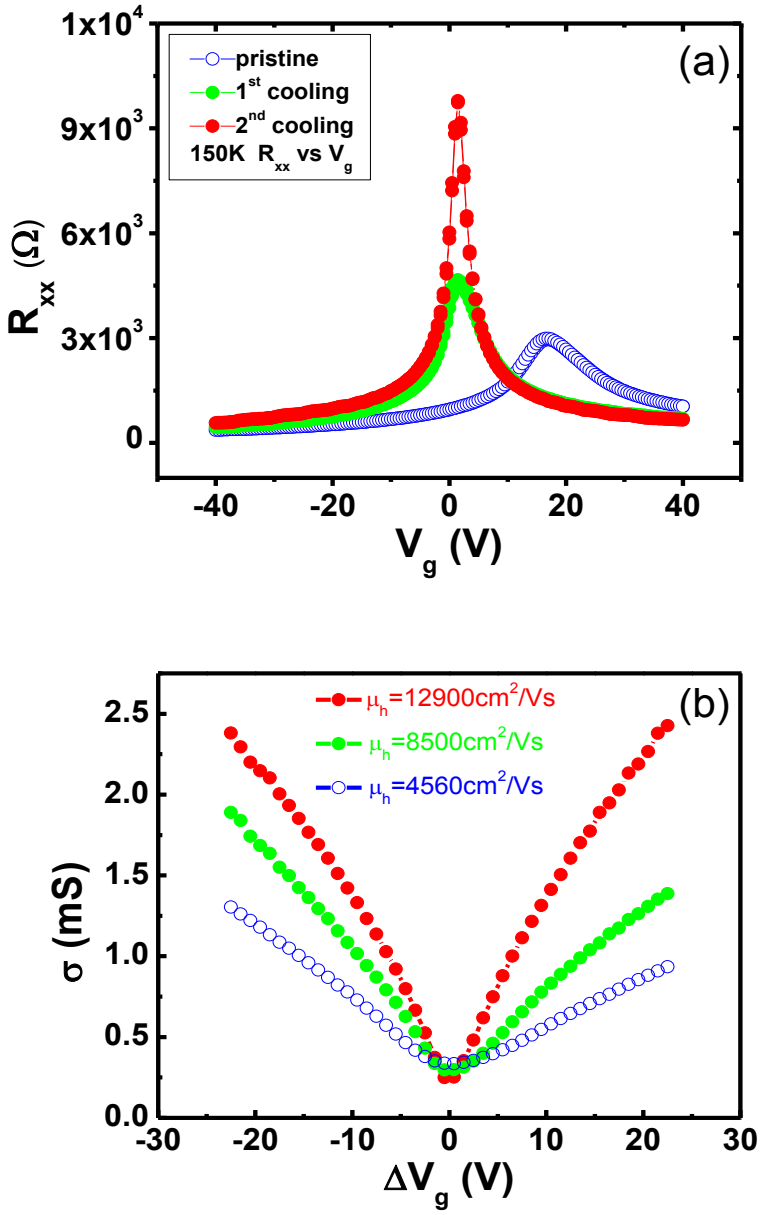

Figure V-1 (a) Sheet resistance vs. gate voltage and (b) Conductance vs. relative gate voltage in the same device (device A) in three distinct mobility states in zero-field.

Now let us switch to the thermoelectric transport result at the same temperature in the same device with zero magnetic field. Figure V-2 shows the corresponding Seebeck coefficient S_{xx} of the same device at those different mobility states, measured in zero magnetic field at 150 K.

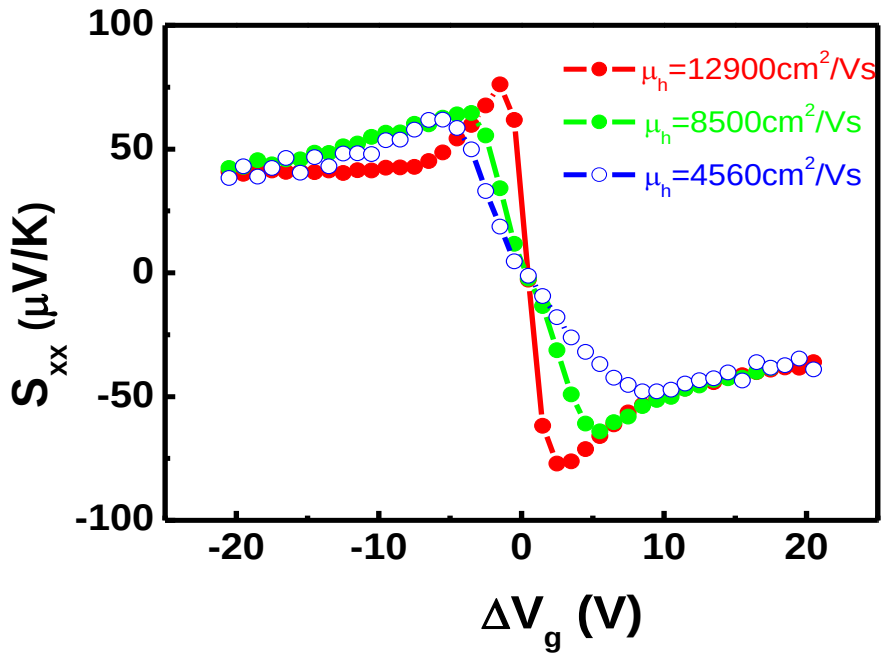

Figure V-2 Seebeck coefficient S_{xx} vs relative gate voltage ΔV_g at zero magnetic field in the same device (device A) in three distinct mobility states at 150 K.

First of all, from Figure V-2 we can see that the Seebeck coefficient passes zero at the Dirac point, where the carrier type switches. On hole carrier side (left side of Dirac point), S_{xx} is positive and on electron carrier side, it is negative. When ΔV_g, which is a measure of carrier density approaches zero, the magnitude of S_{xx} first increases, then reaches a maximum, and then decreases toward zero. This general gate-tunable feature in

S_{xx} is true even for bi-layer graphene devices [Hao *et al.*, 2010; Nam *et al.*, 2010; Wang *et al.*, 2010]. For different mobility states, this maximum value of S_{xx} near charge neural point is different. It increases from ~50 to 75 μV/K, as the mobility increases from 4560 to 12900 cm^2/Vs. There is a divergent trend in S_{xx} seen in high-mobility states and this salient feature is accompanied by a sharper peak-to-dip transition at the vicinity of Dirac point. This results show that the low-mobility state has a broader peak-to-dip transition in S_{xx} while the high-mobility state has a much narrower and more divergent peak-to-dip transition. It is helpful for us to combine both electrical and thermoelectric measurement results together. The width of the minimum conductivity plateau was previously shown to be related with the amount of charged impurities in graphene [Tan *et al.*, 2007]. Therefore, the peak-to-dip width in S_{xx} is also related to the amount of charged impurities. In low-mobility states, the divergent trend is significantly smeared. The diverging behavior was previously found to vary with the low effective carrier density n in the vicinity of the Dirac point, as $\sim 1/\sqrt{n}$ [Wei *et al.*, 2009]. Note that S_{xx} for all mobility states converges to the same values at high gate voltage regime on both electron and hole sides. At high ΔV_g, we expect that the effective carrier density n is much greater than the magnitude of the charge density fluctuations n^* induced by charged impurities near the Dirac point and all transport properties are dominated by the intrinsic other than the induced carriers [Wang *et al.*, 2011]. Therefore, for different carrier mobility states, S_{xx} differs significantly only at low carrier densities. We conclude that the more divergent behavior in higher mobility states is a consequence of smaller n^* due to the reduced amount of charged impurities.

V-3 Mobility Effect on Magneto-thermoelectric Transport: 150 K data

In the previous section, we discussed the mobility effect on zero-field electrical and thermoelectric transport and observed a stark contrast between low and high mobility states. In the presence of high magnetic field, this contrast is much stronger. When we apply a temperature gradient, there is a transverse thermoelectric voltage starts to develop in an external magnetic field perpendicular to the temperature gradient direction and this transverse thermoelectric voltage is called Nernst voltage. In addition to this, the longitudinal thermal voltage also has a response to this external magnetic field. We study the mobility effect on Seebeck coefficient first. Figure V-3 (a) shows S_{xx} of device A in a relatively low mobility states: 8500 cm^2/Vs for a set of magnetic fields measured at 150 K as a function of gate voltage. From the experimental results, we can see that at and below 2 T, S_{xx} has very similar behavior as that in zero field (Figure V-2) except the peak and dip positions indicated by arrows are pushed toward larger V_g i.e. higher carrier density regime. When we increase the amplitude of magnetic fields, in the low-mobility state, the main peak and dip continue to extend to higher V_g. As a result, a broader peak-to-dip transition regime near the Dirac point is developed. At field above 4 T, there is a small kink developed near the Dirac point and at 8 T, this small kink becomes a small plateau feature. In previous study, all the results are obtained in relative low mobility state, and people observed that at the Dirac point even the S_{xx} polarity could be reversed, i.e. S_{xx} is negative at hole side while it is positive at electron side. This reversed polarity is not consistent with carrier type as in conventional conducting material. After we tune the mobility to a higher value in the same device (12900 cm^2/Vs in this case), instead of

the reversed polarity S_{xx}, however, in astounding contrast, there is an additional pair of sharp peak and dip sub-feature appearing near the Dirac point starting from 4 T, while the main peak and dip are also pushed to higher V_g as in the low-mobility state [Figure V-3 (b)]. The sub-features close to the Dirac point increase in magnitude and shift their positions to higher V_g as the magnetic field strength increases.

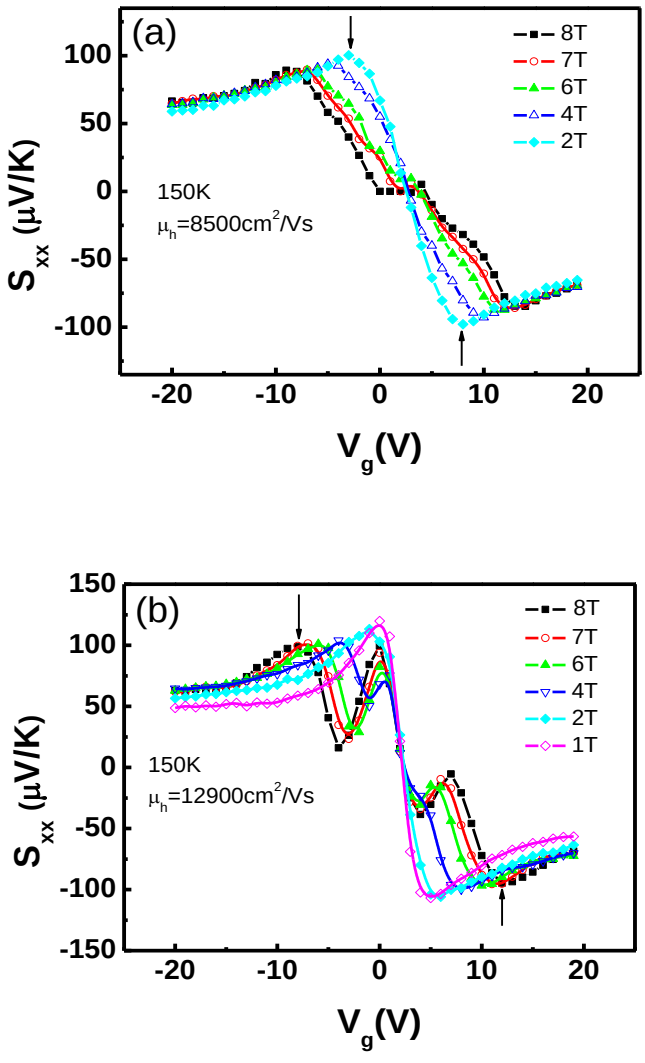

Figure V-3 Seebeck coefficient S_{xx} vs. V_g for different magnetic fields in low (a) and high (b) mobility states of device A measured at 150 K.

Those main peak-dip features correspond well to those low mobility state main peak-dip features in magnitude and position. It is the additional sub-features that distinguish the two mobility states. In low mobility state, we can observe a plateau structure near the Dirac point while we can get this additional peak-dip pair in high mobility state. It seems that the plateau feature in the low-mobility state at 8 T could be just a precursor of the fully-developed peak-dip sub-features observed in the high-mobility state starting to appear even at low magnetic fields. Similar Seebeck sub-features, but all with an opposite polarity, i.e., S_{xx} being negative (positive) on the hole (electron) side which has an opposite sign with that of high LL peaks (dips), have been observed in other samples with mobility less than 5,000 cm^2/Vs in previous literature [Zuev *et al.*, 2009; Wei *et al.*, 2009]. In the high-mobility states, however, the sign of the sub-features sides with that of S_{xx} peaks/dips at high LLs.

In the linear response regime, the charge current in response to an electric field and a temperature gradient can be written as $J = \hat{\sigma}\vec{E} + \hat{\alpha}(-\vec{\nabla}T)$, where J is the electric current and E the electric field, both thermoelectric coefficients S_{xx} and Sxy are related to the tensor elements of the conductivity $\hat{\sigma}$ (or resistivity $\hat{\rho}$) and the thermoelectric conductivity $\hat{\alpha}$. For the Seebeck coefficient S_{xx}, $S_{xx} = \rho_{xx}\alpha_{xx} - \rho_{xy}\alpha_{xy}$ where ρ_{xy} and α_{xy} are the Hall resistivity and transverse thermoelectric conductivity and ρ_{xx} and α_{xx} are the corresponding longitudinal components. At higher LLs, S_{xx} has a definitive sign for electrons or holes as it is dominated by the contribution from the second term $\rho_{xy}\alpha_{xy}$. However, as both ρ_{xy} and α_{xx} change signs at the zeroth LL, S_{xx} changes sign as well but

its polarity is determined by the relative strength of these two terms. The opposite polarity is found to be a strong disorder effect, i.e. the disorder-broadened LL width is much larger than the scale of $k_B T$. Our experiments present the first direct observation that the polarity of S_{xx} switches when the mobility increases, indicating that the reduced LL width in high-mobility samples is comparable with $k_B T$, as predicted. Another possibility is this polarity reversal may be caused by the zeroth LL splitting. In high mobility state and under high magnetic field, the zeroth LL splits into two distinct electron and hole LLs. While we will discuss this issue later, the sharp contrast in S_{xx} between the low and high mobility states clearly demonstrates the effect of disorder on the thermoelectric transport properties near the Dirac point, which is usually not easily seen in the electrical conductivity, especially at this high temperature.

In addition to the longitudinal Seebeck effect, we also systematically studied the mobility effect on the transverse Nernst signal. Figure V-4 (a)-(c) show the Nernst signal S_{xy} at 150 K in device A for three different mobility states. S_{xy} in graphene always has a main peak at the Dirac point, accompanied by a pair of side dip and peak as observed previously [Zuev *et al.*, 2009; Wei *et al.*, 2009; Checkelsky *et al.*, 2009]. In different mobility states, the central peak position varies due to the variation of Dirac point position. We also plot the Nernst data with reference to the Dirac point using ΔV_g instead as our x-axis plot reference [Figure V-4 (d)]. In the highest mobility (12900 cm^2/Vs) state, the Nernst central peak height, $(S_{xy})_{max}$ at 8 T reaches ~190 μV/K, which corresponds to 22 μV per K per unit magnetic field, and this is over four times larger than the previously reported value (~5 μV/KT) [Wei *et al.*, 2009]. As the mobility increases, $(S_{xy})_{max}$

increases and the full width at half maximum (FWHM) decreases which also suggests a lower charged impurity scattering rate. More interestingly, as shown in the inset of Figure V-4 (d), $(S_{xy})_{max}$ is directly proportional to the carrier mobility. It is usually unfair to compare S_{xy} among different samples with different native mobility values. Our mobility tuning capability allows us to compare the effect of disorder/mobility and draw reliable conclusions about the carrier mobility dependence on thermoelectric transport effect.

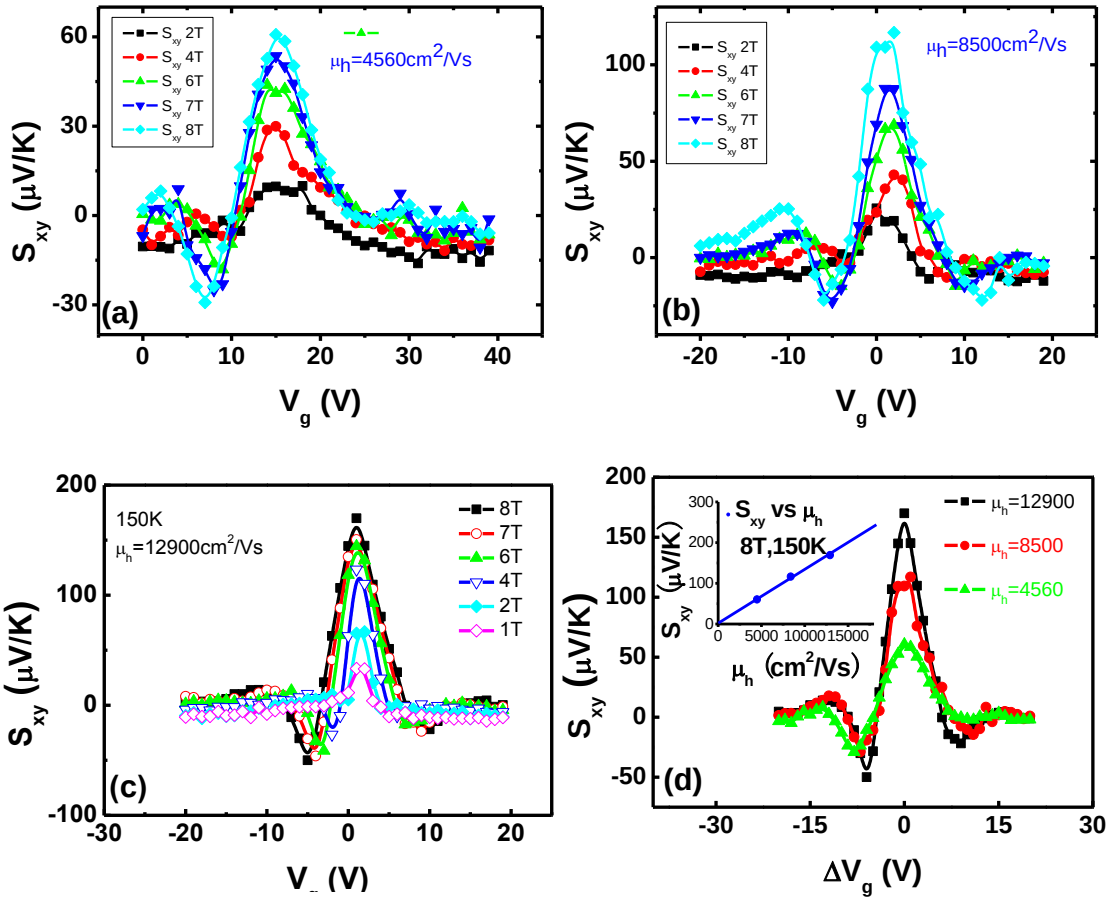

Figure V-4 Nernst signal S_{xy} at 150 K in device A for three distinct mobility states under different magnetic fields (a)-(c). (d) Shows Nernst signal S_{xy} reference to Dirac point at 8 T. The inset in (d) demonstrates that S_{xy} is linearly proportional to carrier mobility within this mobility regime.

For a fixed mobility state, we also measure the Nernst peak height at different magnetic fields. In the highest mobility (12900 cm^2/Vs) state, the magnetic field dependence of S_{xy} is displayed in Figure V-4 (c). At low fields (< 2 T), no side features are present near the central peak. As the magnetic field strength increases, two side dips appear with a slight asymmetry, accompanying the linear increase in the central peak height. It is interesting to note that in the high-mobility state the full width half maximum (FWHM) of the central peak is broadened by the magnetic field strength as $\sim\sqrt{B}$ as shown by Figure V-5 (a). In addition, the Nernst central peak height itself linearly depends on magnetic field as shown in Figure V-5 (b). As the mobility decreases, the central peak is clearly broadened. By comparing S_{xx} with S_{xy} in Figure V-3 (b) and Figure V-4 (d) we do not observe any obvious features in S_{xy} that correspond to the sub-features in S_{xx}.

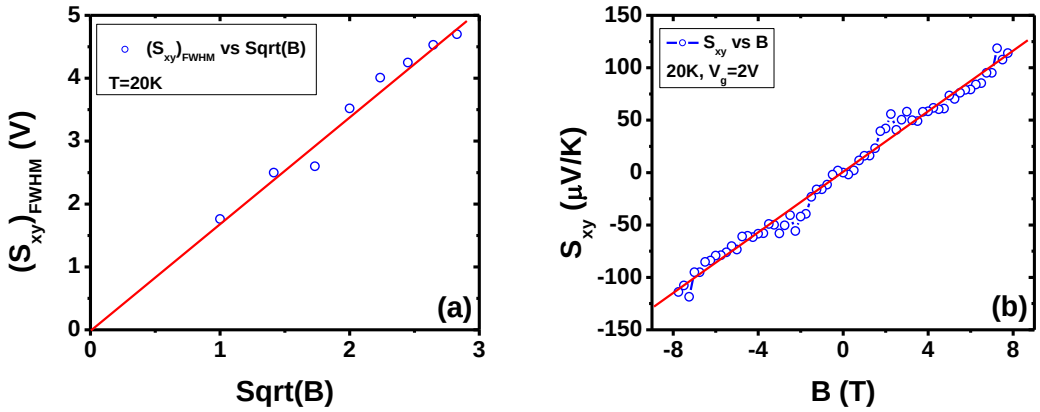

(a) (b)

Figure V-5 (a) FWHM of the central Nernst peak as a function of square root of B (b) Nernst central peak height as a function of B field magnitude. All data taken at 20 K.

To carefully study the sub-feature behavior in S_{xx} that emerges in high-mobility states near Dirac point, we have carried out more detailed measurements of S_{xx} up to 14 T in PPMS for a second high-mobility sample at 150 K (device B, with the highest mobility of 17000 cm^2/Vs). Although there is an asymmetry between the electron and hole side, the sub-features near the Dirac point are well developed as shown in Figure V-6.

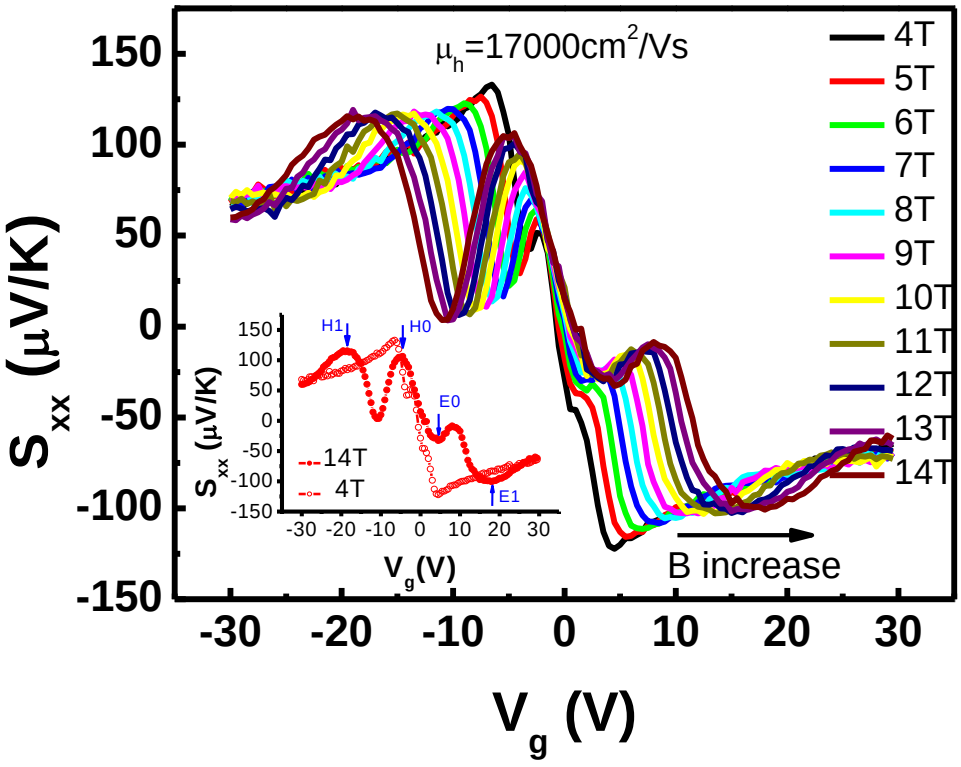

Figure V-6 Seebeck coefficient S_{xx} of device B at its highest mobility state measured at 150 K up to 14 T. The inset shows the contrast between two magnetic fields (4 T and 14 T).

The main peak and dip at $V_g \sim \pm 20$ V correspond to those main peaks and dips in device A. In order to identify these main peak-dip features, we cool device A down to 20 K where well developed quantum oscillations and plateaus emerge in σ_{xx} and σ_{xy}. By comparing the S_{xx} data with the 20 K results in σ_{xx} and σ_{xy}, we find a perfect alignment between these main peak/dip and the first Landau levels for 150 K data, and thus the main peak and dip can be identified as the first Landau levels (LLs), i.e. n= -1 and n= +1, respectively, labeled as H1 and E1 accordingly. If we track the magnetic field dependence of the LL positions in V_g for device A at 20 K, then we can expect a linear behavior as shown in Figure V-7 (a). Since the sub-feature related carrier density is well within n= ±1 LLs, the sub-features most likely originate from the zeroth LL, labeled as H0 and E0 as shown in the inset of Figure V-6. We track the magnetic field dependence of the positions in V_g of E0, H0, E1 and H1 for device B at 150 K. Interesting they all follow straight lines (Figure V-7 (b)) similar to that for higher LLs in device A. The top and bottom lines are for n= ±1 LLs respectively and the two inner lines are for the two sub-features. This linear magnetic field dependence of the positions is understood since the degeneracy of LLs is proportional to the magnetic field. We find that the slope of H1 and E1 lines is approximately 4 times as large as that of H0 and E0. We know that for the zeroth LL, there are two sub-levels on each side of the Dirac point: 2 electron sub-levels and 2 hole sub-levels. If the zeroth LL splits, as schematically shown in the inset, then the E0 peak appears when the chemical potential passes through the middle of the two electron sub-levels, so that the filling is one. As the chemical potential passes through the middle of the next group of sub-levels, i.e. n= +1, four levels are filled (two are from n= 0 and the

other two are from n= +1), so that the filling factor and therefore the slope for E1 is four times as large. The same relationship exists between H0 and H1. This trend continues as the higher LLs are filled and it is indeed seen in the low-temperature data. In high-mobility states, it appears that the splitting of the zero[th] LL is sufficiently larger than the disorder broadening and $k_B T$ so that the sub-features are resolved.

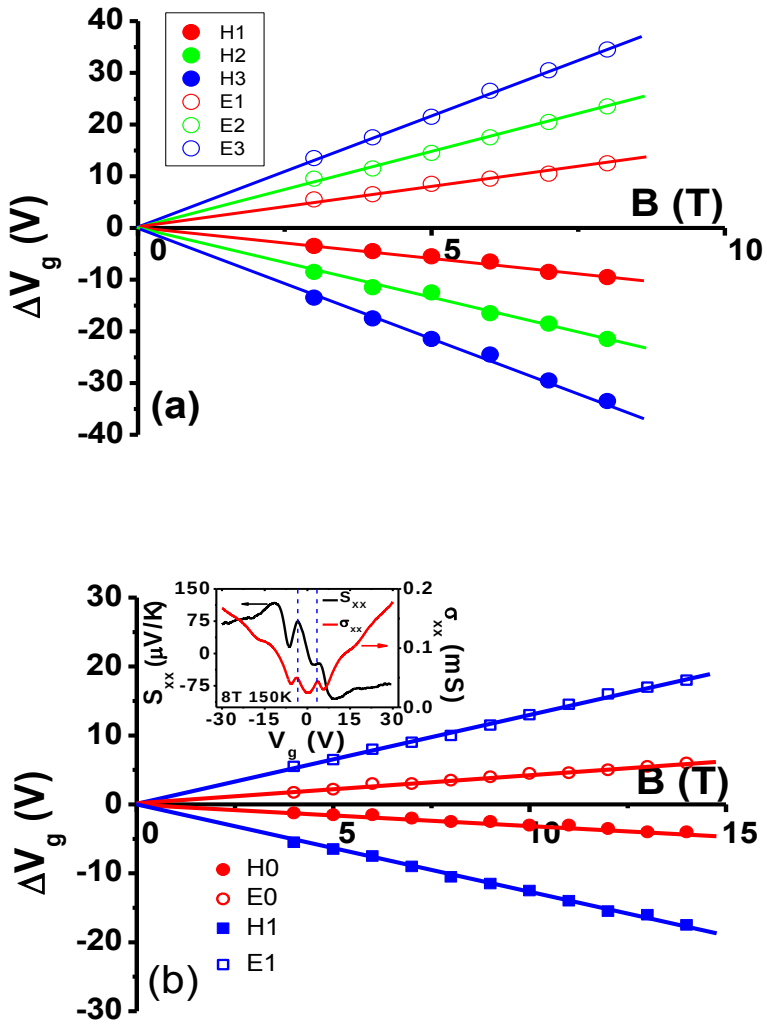

Figure V-7 Magnetic field dependence of the LL positions in V_g (a) for device A at 20 K and (b) for device B at 150 K.

V-4 Effect of Mobility on Low-T Magneto-thermoelectric Transport

All the previous sections present thermoelectric transport results at a relatively high temperature of 150 K. At low temperature, we can expect a strong quantized effect under external magnetic field. We therefore perform the low-temperature magneto-thermoelectric measurement at 20 K. At this temperature, both S_{xx} and S_{xy} develop a series of quantum oscillations in the high mobility state. Figure V-8 (a) and (b) show results from device A for selected quantizing magnetic fields. The evenly spaced peaks and dips in S_{xx} [Figure V-8 (a)] are identified as LLs, i.e. n= ±1, ±2, ±3…, as they are matched well with the characteristic half-integer quantum Hall features in σ_{xx} in Figure V-8 (b) and the plateaus in σ_{xy} (not shown here) taken under the same conditions. As shown in Figure V-8 (a), the occurrence and evolution of the sub-features denoted by black arrows in S_{xx} as a function of the applied magnetic field are evident. The sub-features remain to have the same polarity as that of the high LL peaks and dips, which is consistent with the observations at 150 K. At low fields, both the magnitude and period of the quantum oscillations are smaller. Compared with the low-mobility states, the high-mobility states typically show more clear oscillations. At 4 T, as many as six LLs can be clearly resolved on each side. At 20 K, similar to S_{xx}, more side peaks associated with more LLs can be observed in S_{xy}. In fact, the peaks and dips in S_{xx} correspond well to the zeros in S_{xy}, which are consistent with earlier observations [Wei *et al.*, 2009]. In the highest mobility state of device A where μ=12900 cm^2/Vs, $(S_{xy})_{max}$ is also proportional to the magnetic field, with a slope ~19 μV/KT, comparable with the value of 22 μV/KT at 150 K. In device B, the low-temperature peak height $(S_{xy})_{max}$ also increases as the

mobility increases [Figure V-9 (a)], while the other side-peaks do not seem to be sensitive to the mobility change.

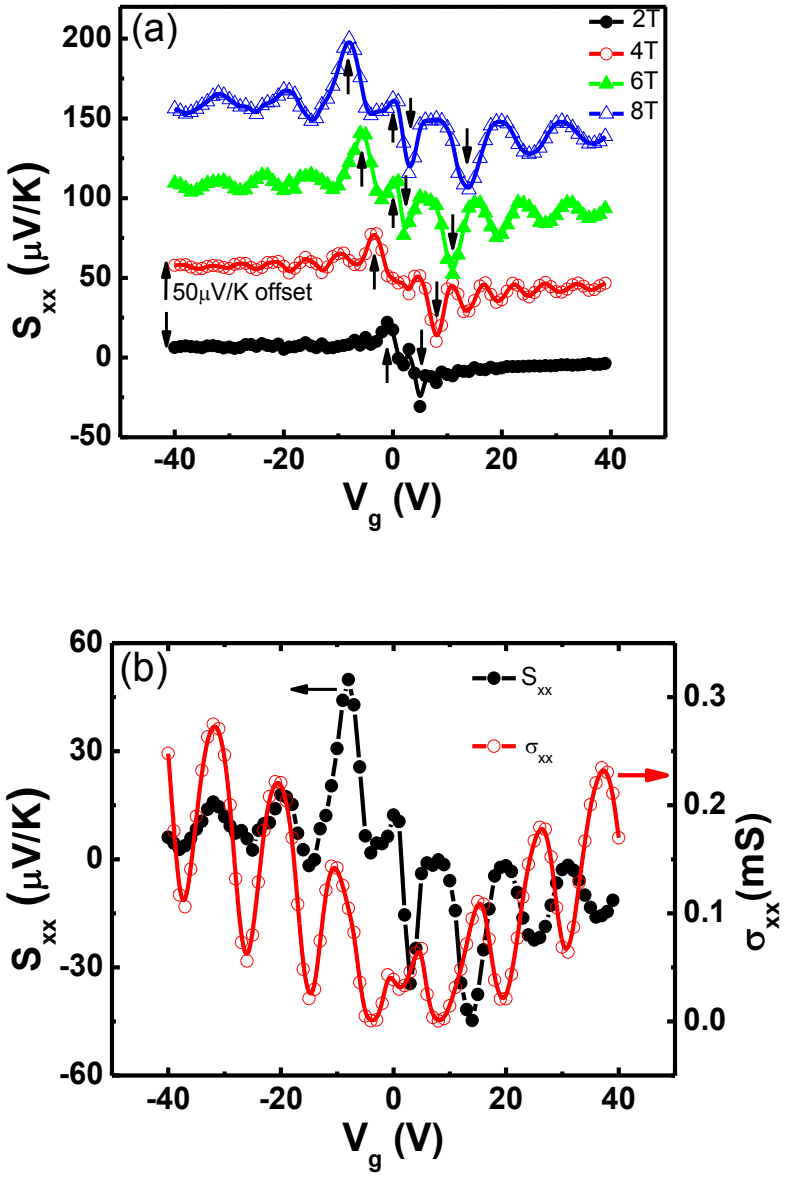

Figure V-8 (a) Quantum oscillations in S_{xx} vs. V_g for different quantizing magnetic fields for device A at 20 K (curves are offset for clarity). Arrows indicate how the peaks shift as the magnetic field is varied. (b). both σ_{xx} and S_{xx} taken at 20 K are plotted together to show the correspondence of the sub-features near the Dirac point.

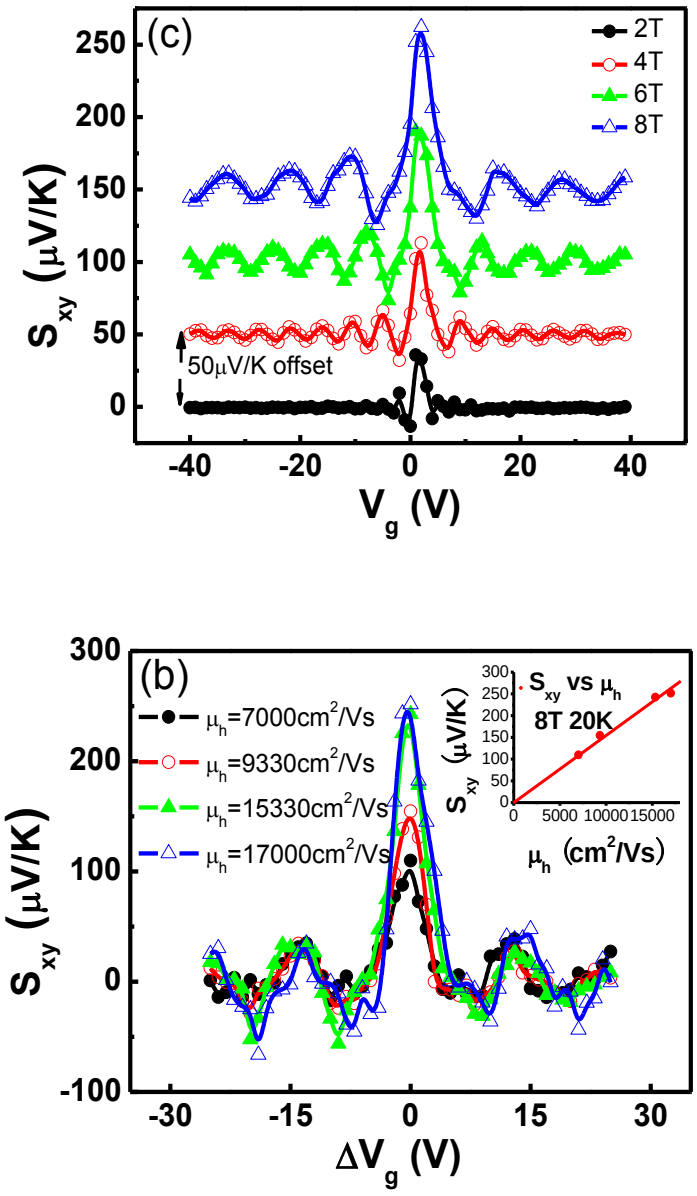

Figure V-9 (a) Quantum oscillations in S_{xy} for different quantizing magnetic fields for device A at 20 K. (b) S_{xy} for device B measured at 8 T and 20 K for four different mobility states. Inset shows the linear dependence of the central S_{xy} peak height on carrier mobility.

Similar linear mobility dependence of $(S_{xy})_{max}$ is observed in device B [inset of Figure V-9 (b)] (similar to the inset of Figure V-4 (d)). This mobility dependence agrees qualitatively with the theoretical calculations with different degrees of disorder. Hence, the Nernst effect may serve as a unique probe for studying the effect of disorder in graphene. Here we observe that both devices show S_{xy} central peak height linearly depends on carrier mobility, where device A is at 150 K while device B is at 20 K.

Now let us switch back to the sub-features near the Dirac point in high mobility state. We observe a double-peak feature in σ_{xx} in both device A and B, implying an insulating state emerging at the Dirac point (As shown in Figure V-8 (b) for device A). The double-peak feature persists up to ~ 150 K (Figure V-10 for device B at 150 K). The sub-features in S_{xx} correspond well to the double peak positions in σ_{xx} both at low temperature (20 K for sample A) and high temperature (150 K for sample B) and the position remains the same as temperature varies. As this feature only exists in high-mobility samples, we could rule out the disorder-driven quantum Hall liquid to insulator transition. Instead, this may be attributed to an insulating phase of many-body origin, which has been under extensive discussions [Abanin *et al.*, 2006&2007; Zhang *et al.*, 2006; Jiang *et al.*, 2007; Checkelsky *et al.*, 2008]. Although the sub-features in S_{xx} alone can be just an intrinsic effect of the zeroth LL as indicated by the numerical calculations based on non-interacting electrons, the correlation with the occurrence of the double-peak structure in σ_{xx} suggests that the electron-electron interaction may be responsible in high-mobility graphene. Another indication is from the peak value of S_{xy}, which is determined dominantly by α_{xy}/σ_{xx}. As σ_{xx} decreases at the Dirac point with the emergence of an insulating state,

$(S_{xy})_{max}$ is greatly enhanced. Hence, a thorough study of both electrical and thermoelectric transport properties in high-mobility graphene may shed light on the fundamental origin of the sub-features and their relation to electron-electron interaction.

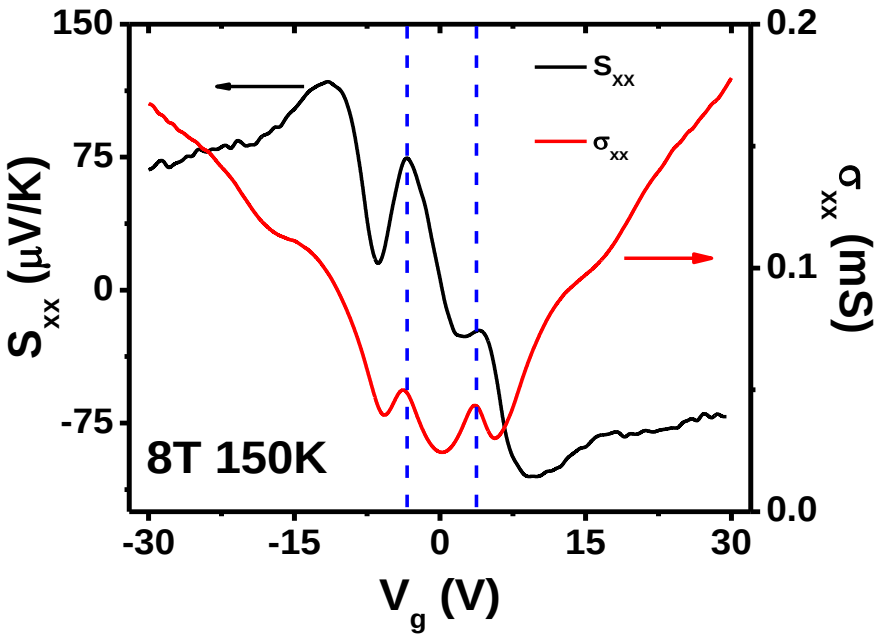

Figure V-10 Quantum oscillation of S_{xx} and σ_{xx} in device B measured in 14 T at 150 K. There is an excellent alignment between the sub-feature in S_{xx} and double peak in σ_{xx} within the zeroth LL.

V-5 Conclusion

In summary, we have investigated the thermoelectric transport properties in the same devices with systematically tuned carrier mobility. In high mobility samples, thermoelectric transport coefficients reveal additional features even at relatively high temperatures and modest magnetic fields near Dirac point. The polarity of the sub-

features is associated with the degree of disorders as predicted. In high-mobility states, the polarity of the sub-features sides with that of the main LL features. Similar to high LL peak positions, the sub-feature positions follow the same linear magnetic field dependence. When we align the thermoelectric transport coefficient with electrical transport coefficient σ_{xx}, these features are found to be correlated with the double-peak feature in the conductivity. Both features are only observable in high-mobility states, suggesting their electron-electron interaction origin. In addition to this, we have also demonstrated that the central Nernst peak height at the Dirac point is directly proportional to the carrier mobility, which offers a new possibility of exploring the interplay between disorder and electron-electron interaction in graphene. The central Nernst peak height linearly depends on magnetic field amplitude, which is consistent with prediction of Mott relation in semi-classical regime.

Reference

Tan, Y. W. *et al.*, Phys. Rev. Lett. **99**, 246803 (2007).

Dean, C. R. *et al.*, Nature Nanotechnology **5**, 722 (2010).

Chen, J. H. *et al.*, Nature Nanotechnology **3**, 206 (2008).

Adam, S. *et al.*, Proc. Natl. Acad. Sci. U.S.A. **104**, 18392 (2007).

Bolotin, K. I. *et al.*, Phys. Rev. Lett. **101**, 096802 (2008).

Du, X. *et al.*, Nature Nanotechnology **3**, 491 (2008).

Ugarte, V. *et al.*, Phys. Rev. B **84**, 165429 (2011).

Gusynin, V. P. *et al.*, Phys. Rev. B **73**, 245411 (2006).

Zhu, L *et al.*, Phys. Rev. Lett. **104**, 076804 (2010).

Zuev, Y. M. *et al.*, Phys. Rev. Lett. **102**, 096807 (2009).

Wei, P. *et al.*, Phys. Rev. Lett. **102**, 166808 (2009).

Checkelsky, J. G. *et al.*, Phys. Rev. B **80**, 081413 (2009).

Wang, D. Q. *et al.*, Phys. Rev. B **83**, 113403 (2011).

Liu, X. F. *et al*, Solid State Commun. **152 (6),** 469 (2012).

Wang, D. Q. *et al.*, Nano Lett. **10**, 4989 (2010).

Hao, L *et al.*, Phys. Rev. B **81**, 165445 (2010).

Nam, S. G. *et al.*, Phys. Rev. B **82**, 245416 (2010).

Wang, C. R. *et al.*, Phys. Rev. B **82**, 121406(R) (2010).

Abanin, D. A. *et al.*, Phys. Rev. Lett. **96**, 176803 (2006).

Abanin, D. A. *et al.*, Phys. Rev. Lett. **98**, 196806 (2007).

Zhang, Y. *et al.*, Phys. Rev. Lett. **96**, 136806 (2006).

Jiang, Z. *et al.*, Phys. Rev. Lett. **99**, 106802 (2007).

Checkelsky, J. G. *et al.*, Phys. Rev. Lett. **100**, 206801 (2008).

Chapter VI

Derivative Relations

VI-1 Introduction

In conventional two-dimensional electron gas (2DEG), Chang and Tsui [Chang and Tsui, 1985] first discovered the empirical relation between the longitudinal resistivity R_{xx} and the Hall resistivity R_{xy}, i.e.

$$R_{xx} = \alpha_r \cdot \frac{B}{n} \frac{dR_{xy}}{dB}, \qquad (1)$$

with n being the carrier density, B the magnetic field and α_r a B-independent constant. Later on it is found this derivative relation holds remarkably well in a number of other 2DEG systems in both integer and fractional Hall regimes [Rötger *et al.*, 1989; Morawicz *et al.*, 1990; Stormer *et al.*, 1992; Allerman *et al.*, 1995]. Although the microscopic origin of this empirical relation is still under debate, it has been proposed [Vagner *et al.*, 1988; Simon *et al.*, 1994] that due to inhomogeneities existing on different length scales, local fluctuations in the Hall resistivity via carrier density fluctuations could affect the global longitudinal resistivity. More recently, Tieke *et al.* [Tieke *et al.*, 1997] experimentally demonstrated another similar but very important derivative relation between the longitudinal (S_{xx}) and transverse (S_{yx}) thermoelectric transport coefficients in a traditional GaAs/$Ga_{1-x}Al_xAs$ 2DEG, i.e.

$$S_{yx} = \alpha_s \cdot \frac{B}{n} \frac{dS_{xx}}{dB}, \qquad (2)$$

As shown in Figure VI-1, they first demonstrate that in thermoelectric transport, the transverse Nernst coefficient can be well reproduced by derivative of the longitudinal Seebeck coefficient with respect to magnetic field multiplied by an empirical constant α_s. In the mean time, they showed that this derivative relation in thermoelectric coefficient is equivalent to the resistivity derivative relation under certain conditions.

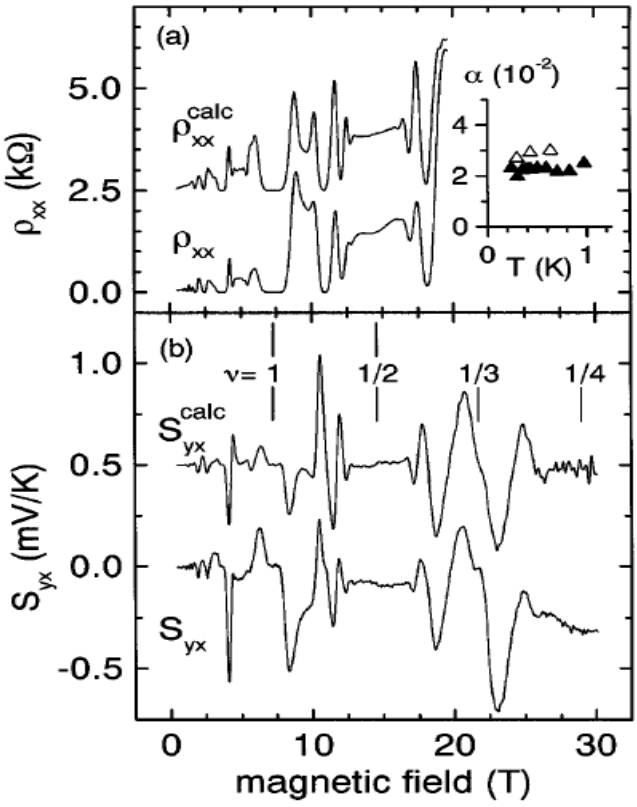

Figure VI-1 Derivative relation in Quantum Hall Effect regime from Tieke in 1997 (a) Experimentally measured longitudinal ρ_{xx} and calculated ρ_{xx}^{calc} by eq. (1) as a function of B at constant carrier density (b) Experimentally measured transverse S_{xy} and calculated S_{xy}^{calc} by eq. (2) as a function of B at constant carrier density [Tieke *et al.*, 1997].

This raises further interesting questions about the fundamental physical mechanism of both relations. For example, both S_{xx} and S_{yx} are usually dominated by the phonon drag contribution at low temperatures in 2DEG systems [Fletcher *et al.*, 1986]. The fact that this derivative relation holds for thermoelectric transport coefficients in 2DEGs suggests that the validity of the relations seems to be more universal.

In conventional 2DEG systems [Pudalov *et al.*, 1983], it is not frequent to vary carrier density *n*, not to mention the carrier type. In fact, the empirical relations were originally found and subsequently verified for fixed carrier density *n* and varying magnetic *B*-field. However, in principle, both carrier density and carrier type can be tuned by electrostatic gating technique in a 2DEG system. In the quantum Hall regime, since the filling factor is $\nu = \frac{nh}{eB}$, the derivative to magnetic field B can be converted into derivative to carrier density n by the following relation:

$$\nu = \frac{nh}{eB} >> \frac{d}{dn} = \frac{d}{d\nu}\frac{d\nu}{dn} = \frac{d}{dB}\frac{dB}{d\nu}\frac{d\nu}{dn} = -\frac{B}{n}\frac{d}{dB} \qquad (3)$$

Graphene is an ideal but unique 2DEG system whose carrier type and density can be easily tuned by electron static gating technique. This provides us with an excellent prototype system to study this derivative relation for varying carrier density. In addition, for a graphene device sitting on SiO_2/Si substrate, the relation between its carrier density and the applied gate voltage is determined by the capacitance relation: $en = C_g V_g$. Here e is absolute value of electron charge and *n* is carrier number density. If we plug this capacity relation into equation (1) and (2) we can express the derivative relation for both electrical and thermoelectric transport coefficients as following:

$$R_{xx} = -\alpha_r \frac{e}{C_g} \frac{dR_{xy}}{dV_g}, \qquad (4)$$

and $S_{yx} = -\alpha_s \frac{e}{C_g} \frac{dS_{xx}}{dV_g}$, or

$$S_{xy} = \alpha_s \frac{e}{C_g} \frac{dS_{xx}}{dV_g}, \qquad (5)$$

where e is the absolute value of the electron charge; C_g is the SiO_2 gate capacitance; α_s is an n-independent constant, and V_g is the gate voltage that controls the carrier density and carrier type. Hence, from our point of view, it is expected that these relations hold when n is tuned instead. This is the starting point of this section. By varying n, the relative length scale of local inhomogeneities can be changed and therefore the effect of local density fluctuations on global dissipation can be investigated, which offers a different perspective to examine the validity of the empirical relations. Graphene is such an ideal 2D electron system for this purpose, because as we mentioned previously, the charge carriers can be smoothly tuned from electrons to holes through the charge neutrality point or the Dirac point, and vice versa [Novoselov *et al.*, 2004; Geim *et al*, 2007]. In addition, compared with conventional 2DEG, the distinct Dirac dispersion relation of graphene could bear unusual consequences in both electrical and thermoelectric transport properties as well as the derivative relations. Furthermore, we already demonstrated that the charged impurity state and consequently the carrier mobility can be tuned in the same devices [Wang *et al.*, 2010]. So we can examine the derivative relations as we tune the mobility and consequently the charged impurity state, while leaving everything else unchanged so that we can obtain information at different transport length scale. Previous reported graphene

thermoelectric transport experimental results seem to suggest that the diffusion thermopower dominates [Zuev *et al.*, 2009; Wei *et al.*, 2009; Checkelsky *et al.*, 2009], which is different from the situation in conventional 2DEGs where the thermopower is dominated by phonon-drag. Here we report our first experimental study on both electrical and thermoelectric transport coefficients and their derivative relations in the quantum Hall regime as both carrier density and magnetic field are varied independently.

VI-2 Experimental Results

All data in this section are collected from device A and B discussed about in chapter V whose mobility are tuned using the mobility tuning approach previously described. The measurements were carried out in an Oxford cryostat which covers the temperature range from 2 to 300 K and magnetic fields up to 8 T. In this section, we only demonstrate low-temperature data which show clear quantum Hall plateaus and quantum oscillations, because at high temperature, without clear quantum oscillations, it is hard to study this derivative relation with characteristic features.

We measured all the electrical and thermoelectric transport coefficients at 20 K for device A and made 2D plot as shown by Figure VI-2. Each pair, R_{xx} and R_{xy}, or S_{xx} and S_{xy}, is taken simultaneously under exactly the same conditions as V_g is swept at fixed B-fields, so that when we take derivative, all fluctuations will not come in. In order to obtain these 2D maps, we measured a number of gate voltage V_g dependent curves for different B-fields. The Dirac point in the raw data is located at ~ +2 V, but in the figures the data are plotted against the relative Dirac point for clarity, so we use ΔV_g instead. We can

clearly identify multiple plateaus or quantum oscillations corresponding to different Landau levels (LL). When the chemical potential passes LLs R_{xx} peaks at local maximum while S_{xx} shows either peaks or dips, with peaks corresponding to hole LLs and dips corresponding to electron LLs. In the quantum Nernst signal S_{xy}, there is always a main positive peak right at the Dirac point or the zeroth LL, accompanied by a pair of side peak-dip feature at each LL on both sides.

In order to study the derivative relation between various transport coefficients, we first study how these transport coefficients and derivative relations evolve as a function of B. We draw a vertical line at fixed V_g=+25 V and data along this line shows B dependent behavior. Results are shown in Figure VI-3. Under these conditions, all transport coefficients show characteristic features such as the half-integer quantum Hall effect in R_{xy} and quantum oscillations in other coefficients. Both experimentally measured R_{xx} (S_{xy}) and calculated R_{xx}^{Calc} (S_{xy}^{Calc}) are displayed in Figure VI-3 (a) (3 (b)), where R_{xx}^{Calc} and S_{xy}^{Calc} are obtained from experimentally measured R_{xy} and S_{xx} by applying Eqs.1 and 2 respectively. The black curves are experimentally measured data for both R_{xx} and S_{xy} vs. B while red curves are for calculated results. It is clear that the main oscillatory features in both R_{xx} and S_{xy} correspond well to those in R_{xx}^{Calc} and S_{xy}^{Calc} calculated from independently measured R_{xy} and S_{xx}. This excellent correspondence justifies the validity of the derivative relations for both electrical and thermoelectric transport coefficients at this representative electron density (~ 1.7×10^{12} cm^{-2}) for graphene whose charge carriers are massless Dirac Fermions other than traditional carriers in a 2DEG.

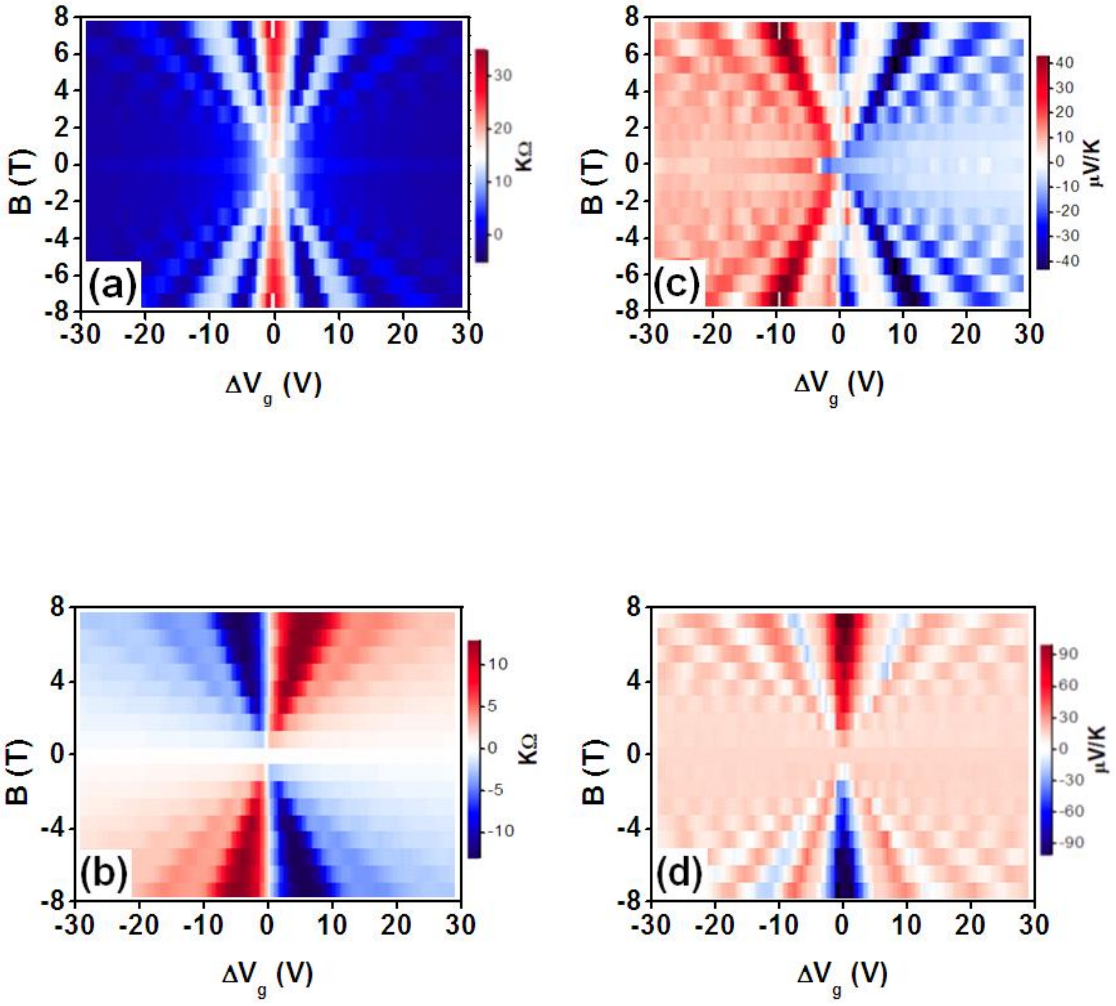

Figure VI-2 2D plots of four measured transport coefficients of device A with varying gate voltage and varying magnetic field: R_{xx} (a), R_{xy} (b), S_{xx} (c), and S_{xy} (d). Each pair, R_{xx} and R_{xy}, or S_{xx} and S_{xy}, were measured simultaneously, and all four coefficients were measured at T= 20 K. The plot is made with respect to relative gate voltage ΔV_g.

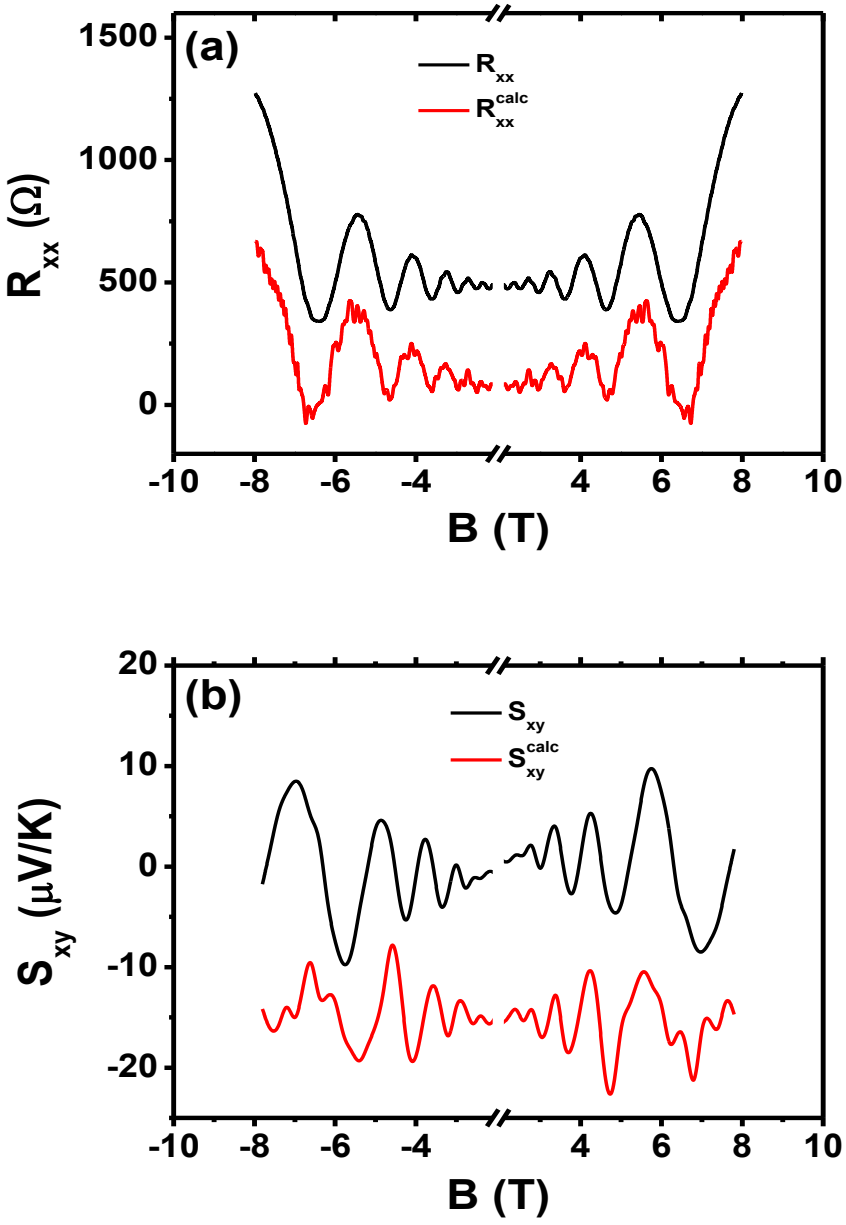

FigureVI-3 (a) Experimentally measured R_{xx} and calculated R_{xx}^{Calc} (using Eq. 1) from R_{xy} vs. B. (b) Experimentally measured S_{xy} and calculated S_{xy}^{Calc} (using Eq. 2) from S_{xx} vs. B.

We can easily tune both carrier density and carrier type of graphene by electrostatic gating technique. In traditional 2DEG it is not convenient to do so. At fixed magnetic field B, by sweeping V_g we can access different LLs and the Dirac point. This offers a convenient way to examine the validity of the derivative relations in another degree of freedom: derivative to *n* instead of B. We take the 4 T line scans in Figure VI-2 to do analysis as shown in Figure VI-4. At 4 T, we can easily obtain up to six LLs on each side of the Dirac point and this indicates very high sample quality.

The fact that there are as many as 6 LLs on each side provides us enough comparison space to investigate this derivative relation in quantum hall regime. Figure VI-4 (a) shows longitudinal electrical transport coefficients i.e. R_{xx} as in Figure VI-3 (a), except that it is now plotted as functions of V_g for B=4 T. In this case, because resistivity R_{xx} always has a large peak value at the Dirac point, it will make oscillatory features at other LLs not so evident. To make a better comparison for the oscillatory features that have smaller magnitude, we exclude the central peak region and display it separately later in Figure VI-5 and 6. Here we should note that the peaks in R_{xx} in Figure VI-4 (a) correspond to the zeros in quantum Nernst signal in Figure VI-4 (b).

We apply Eqs. 4 and 5 to calculate R_{xx}^{Calc} and S_{xy}^{Calc} from the independently measured Hall and Seebeck coefficients, and then show them in the same figures as experimental results. Except for the zeroth LL, features in experimentally measured R_{xx} and S_{xy} for all other LLs match very well with the corresponding features in calculated R_{xx}^{Calc} and S_{xy}^{Calc}.

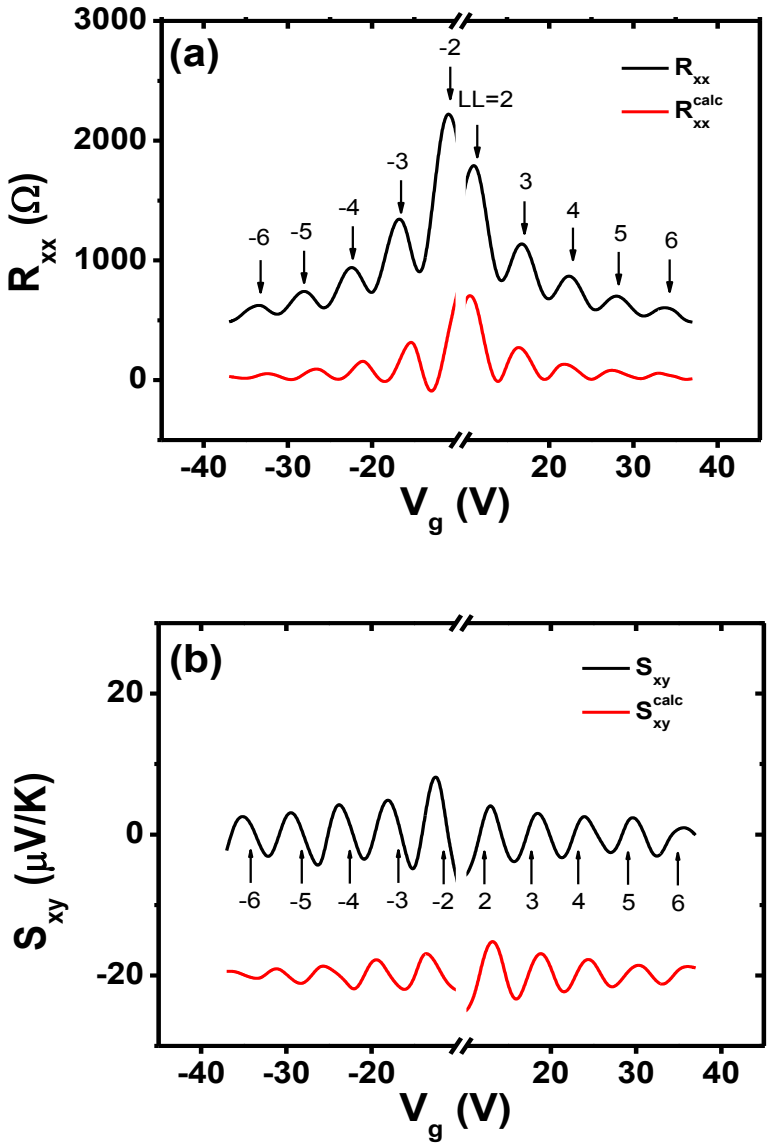

Figure VI-4 (a) Experimentally measured R_{xx} and calculated R_{xx}^{Calc} (using Eq. 4) from R_{xy} vs. gate voltage at B = 4 T and T= 20 K. The peaks are labeled by LL indices. (b) Experimentally measured S_{xy} and calculated S_{xy}^{Calc} (using Eq. 5) from S_{xx} vs. gate voltage under the same conditions as in (a).

When we sweep the gate voltage V_g through Dirac point from negative to positive, the carrier type switches from hole to electron. From the single particle picture, we expect R_{xy} to switch the sign from positive to negative too which will give rise to a negative R_{xx}^{Calc} at the Dirac point according to Eq. 4. But in experiment, we actually get a positive R_{xx} peak, so it is not consistent with calculated value as shown by Figure VI-5

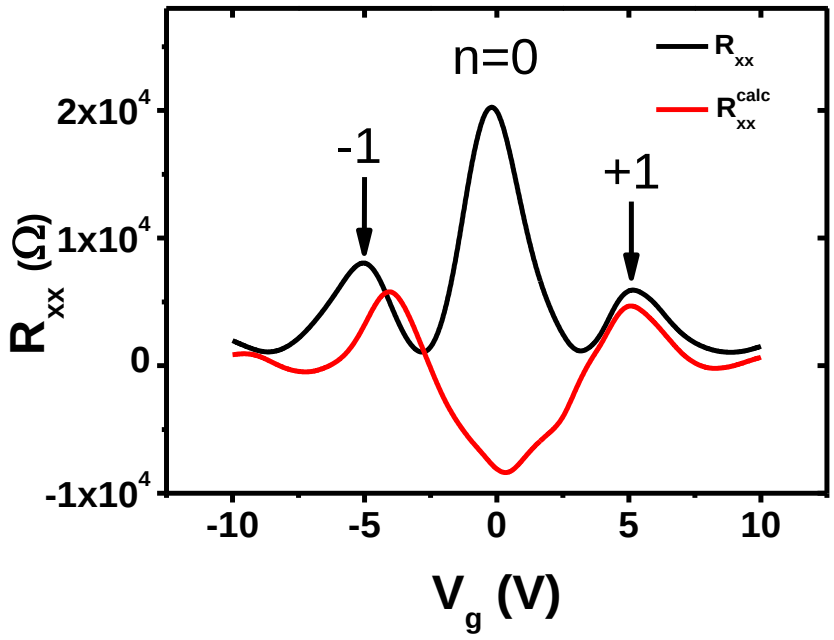

Figure VI-5 Comparison between experimentally measured R_{xx} and calculated R_{xx}^{Calc} at the vicinity of Dirac point.

Similarly, as V_g is swept through the Dirac point from the negative side, S_{xx} passes zero from positive to negative and this produces a negative peak S_{xy}^{Calc} as well at the

Dirac point according to Eq. 5 [Figure VI-6]. Both Eqs.4 and Eqs.5 fail at the zeroth LL. This inconsistency is clearly unphysical. We will discuss more about this later. Away from the zeroth LL, the derivative relations hold quite well in both polarity and the decreasing trend of the oscillation amplitude at higher densities. For the thermoelectric transport coefficient, we also note that while the match is perfect on the electron side, there is a phase shift between the measured and calculated curves on the hole side. We also observe similar phase shift at different magnetic fields. The phase shift behavior is much smaller in electrical transport coefficient.

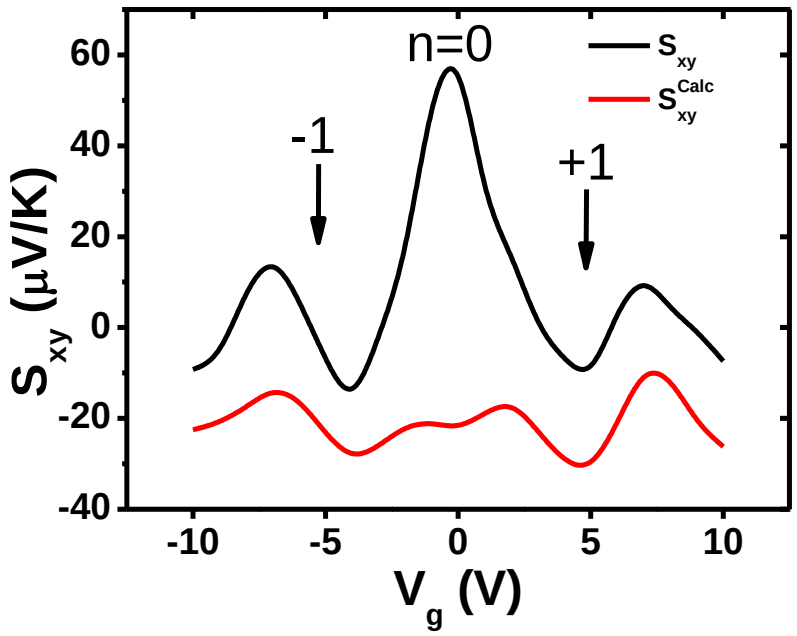

Figure VI-6 Comparison between experimentally measured S_{xx} and calculated S_{xx}^{Calc} at the vicinity of Dirac point.

In the original work of Chang & Tsui, the equation contains *n* in the denominator, which is in the same form as our Eq. 1. In the same spirit, Eq. 2 also contains *n*. Whether this *n* appears in Eqs.1 and 2 does not have any consequence if *n* is fixed while *B* is swept in experiments. In later literatures, this *n* was dropped from the equations. In our experiments, however, we sweep V_g so that *n* is a variable now. Obviously, the presence or absence of *n* does have important consequences when *n* is not fixed any more. Eqs. 4 and 5 are equivalent to Eqs. 1 and 2; therefore, *n* cancels out. In Figure VI-4 both R_{xx}^{Calc} and S_{xy}^{Calc} are calculated with Eqs. 4 and 5, i.e. without *n* in front. To distinguish the two cases, we have also calculated R_{xx}^{Calc} and S_{xy}^{Calc} with *n* in Eqs. 4 and 5 as shown in Figure VI-7. We find that by including *n* in front, the oscillation amplitude of both R_{xx}^{Calc} and S_{xy}^{Calc} stay approximately constant, which obviously disagree with the observed decreasing trend in the amplitude of R_{xx} and S_{xy} as *n* increases [Figure VI-7 (a) and Figure VI-7 (b)]. Hence we conclude that Eqs. 1-5 are consistent with our experimental data; therefore, both pre-factors α_r and α_s defined in our way are independent of *n*. We have used the *n*-independent pre-factors extracted from our data to calculate the dimensionless pre-factors in Tieke's work for the particular carrier density of their samples, and found reasonable agreement with each other.

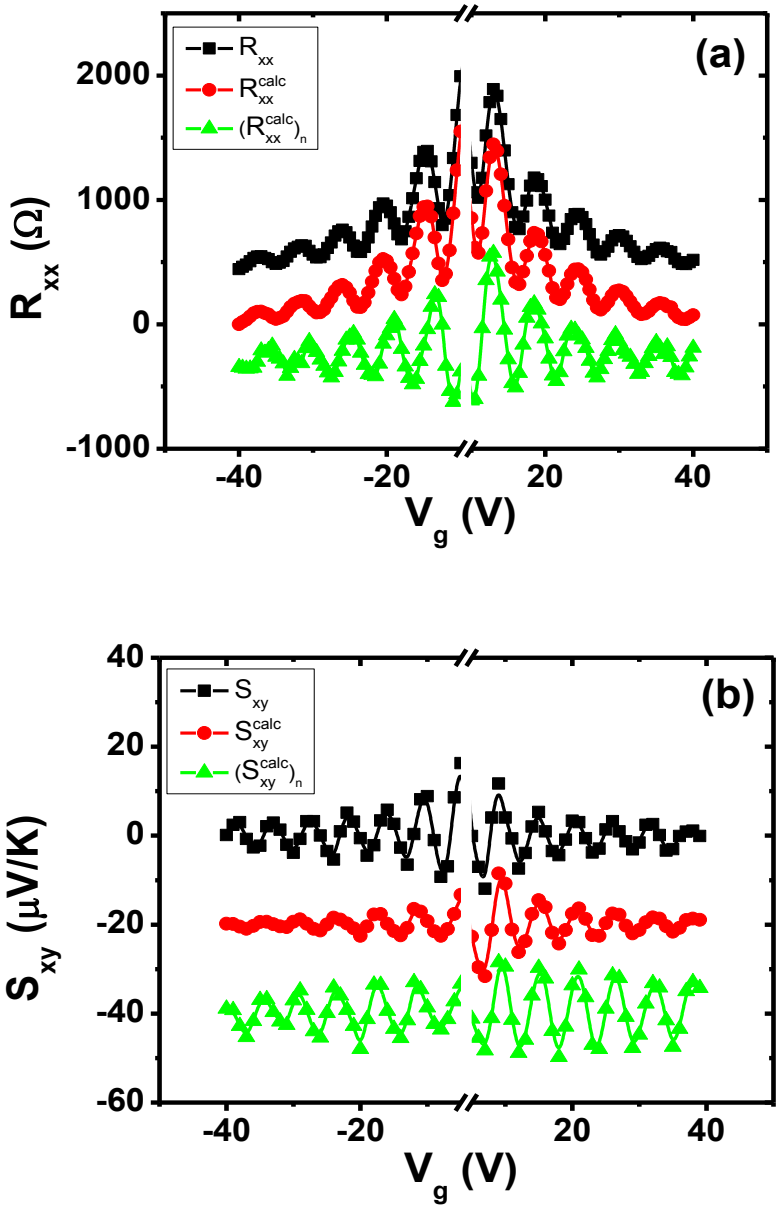

Figure VI-7 (a) Measured R_{xx} and calculated R_{xx}^{Calc} [red: without *n* and green: with *n*] (b) Measured S_{xx} and calculated S_{xx}^{Calc} [red: without *n* and green: with *n*].

VI-3 Discussion

In our previous paragraphs, we have just demonstrated that the empirical relations hold very well for high densities or high LLs. At low densities, e.g. approaching the zeroth LL, however, the relations does not hold as we discussed earlier. To focus on low densities, we sweep the magnetic field at a constant gate voltage.

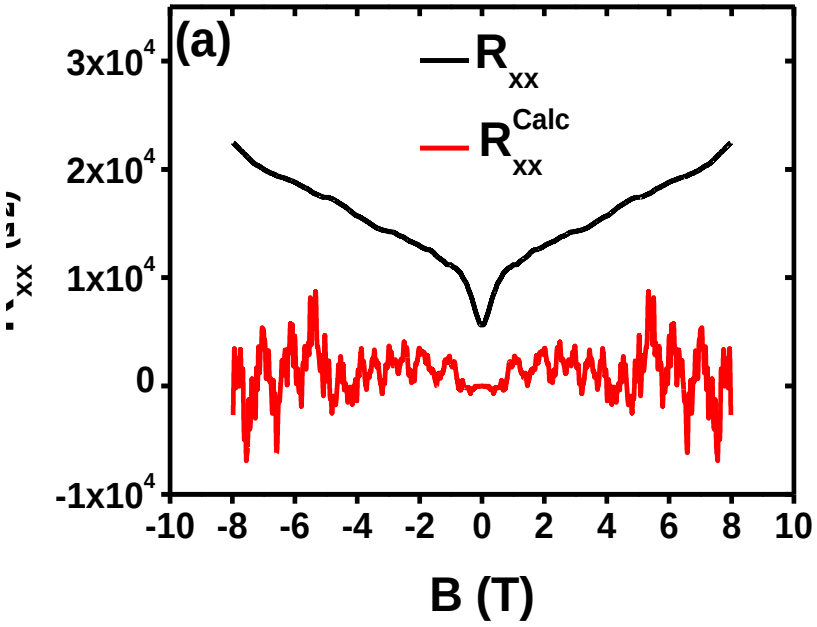

Figure VI-8 Comparison of R_{xx} and R_{xx}^{Calc} vs. B at V_g= +2 V, at the Dirac point.

Figure VI-8 shows the comparison of R_{xx} and R_{xx}^{Calc} for V_g= +2 V (at the Dirac point) in a varying magnetic field at 20 K. R_{xx} monotonically increases as B increases, but in the meantime R_{xy} only increases slightly so that R_{xx}^{Calc} stays nearly constant. Apparently, near the Dirac point, the behaviors of R_{xx} and R_{xy} are qualitatively different from those at

higher carrier density regime, and the derivative relation does not hold any more. The increasing trend in R_{xx} is similar to the high-field insulating behavior reported previously [Checkelsky *et al.*, 2008]. Therefore, the relations are likely complicated or even rendered invalid by new physics occurring at the Dirac point. Further investigation of the zeroth LL behavior is desired to fully understand this interesting phenomenon.

Beside the carrier density tuning, we are able to tune the low-temperature mobility as we discussed in previous sections. In device B which has been discussed about in Chapter V, we have succeeded in setting four different mobility values and obtaining quantum Seebeck and Nernst data at low temperatures. In general, the higher the mobility, the better quality data the device has. We find that the relation between S_{xx} and S_{xy} (i.e. Eq. 5) holds well for all mobility states away from the Dirac point. From those results, we obtain the pre-factor, α_s, for different mobility values. We plot the pre-factor, α_s as a function of carrier mobility as shown in Figure VI-9. Apparently, parameter α_s does not change significantly with the carrier mobility. Instead, it stays a constant within the experimental accuracy range. In graphene, one school of thoughts is that the mobility is largely determined by the charged impurities that have a direct consequence on the carrier density fluctuations near the Dirac point [Hwang *et al.*, 2007 and 2008]. By varying carrier mobility, the fluctuations in carrier density and their length scales may be varied; therefore, one might expect parameter α_s to be different. Our results indicate that within the tunable range of the mobility, neither the derivative relations nor the pre-factor is obviously affected. This result agrees with the previously reported results in conventional 2DEG systems in the quantum transport regime.

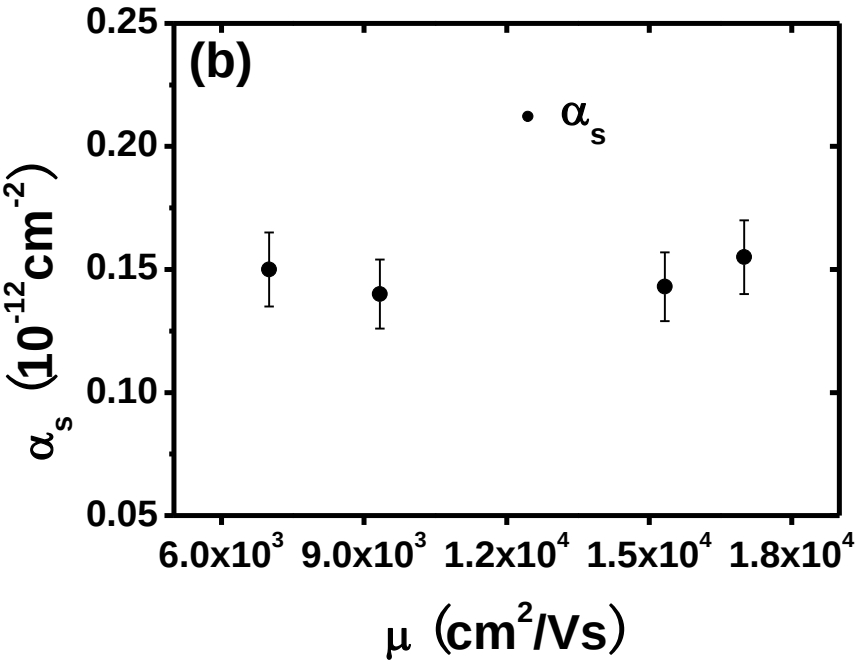

Figure VI-9 α_s, the pre-factor in Eq. 4, as a function of carrier mobility μ of a device.

In summary, we have measured four electrical and thermoelectric transport coefficients in graphene quantum transport regime and examined the empirical derivative relations among them by independently varying the magnetic field and gate voltage. We have concluded that first, these relations hold very well when the carrier density in this 2D Fermions system is varied and the empirical fitting parameter α_s does not depend on carrier mobility obviously. Second, our experimental results show this derivative relation fails at the Dirac point. The universality of the relations suggests some common physical origins shared by 2D electron systems in quantum transport regime despite their widely different properties.

Reference

A. M. Chang and D. C. Tsui, Solid State Commun. **56**, 153 (1985).

Rötger, T *et al.*, Phys. Rev. Lett. **62**, 90 (1989).

Morawicz, N. G., Phys. Rev. B **41**, 12687 (1990).

Stormer, H. L., Solid State Commun. **84**, 95 (1992).

Allerman, A. A., J. Appl. Phys. **77**, 2052 (1995).

Vagner, D. I., Phys. Rev. B **37**, 7147 (1988).

Simon, H. S., Phys. Rev. Lett. **73**, 3278 (1994).

Tieke, B., Phys. Rev. Lett. **78**, 4621 (1997).

Fletcher, R., Phys. Rev. B **33**, 7122 (1986).

Pudalov, M. V., JETP Lett. **38**, 202 (1983).

Novoselov, K. S. *et al.*, Science **306**, 666 (2004).

Geim, A. K. *et al.*, Nature Materials **6**, 183 (2007).

Wang, D. Q. *et al.*, Nano Lett. **10 (12)**, 4989 (2010).

Zuev, Y. M. *et al.*, Phys. Rev. Lett. **102**, 096807 (2009).

Wei, P. *et al.*, Phys. Rev. Lett. **102**, 166808 (2009).

Checkelsky, J. G. *et al.*, Phys. Rev. B **80**, 081413 (2009).

Checkelsky, J. G. *et al.*, Phys. Rev. Lett. **100**, 206801 (2008).

Hwang, E. H. *et al.*, Phys. Rev. Lett. **98**, 186806 (2007).

Hwang, E. H. *et al.*, Proc. Nat. Acad. Sci. USA. **104**, 18392 (2007).